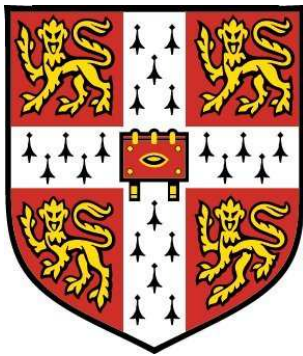# Post-main Sequence

Evolution of Planetary Systems

Amy Bonsor

Institute of Astronomy

St. John's College

University of Cambridge

A thesis submitted for the degree of

Doctor of Philosophy

October 2011

Declaration

I hereby declare that my thesis entitled **The post-main sequence evolution of planetary systems** is not substantially the same as any that I have submitted for a degree or diploma or other qualification at any other University. I further state that no part of my thesis has already been or is being concurrently submitted for any such degree, diploma or other qualification.

Furthermore, the work presented in this dissertation is my own and contains nothing which is the outcome of work done in collaboration with others, except as specifically indicated clearly in the text and acknowledgments. Whilst all writing was generated by myself, I have asked others (credited in the acknowledgments) for their aid in editing and revision.

I note that Chapters 1 and 2 are intended as reviews, and as such contain little, if any, original work. They contain a number of images and plots extracted from other published works, all of which are clearly cited in the appropriate caption.

Those parts of this thesis which have been published or accepted for publication are as follows:

- Much of the work contained in Chapter 3 formed the basis of the work published as Bonsor, A. & Wyatt, M., Post-main-sequence evolution of A star debris discs, MNRAS, 2010, 409, 1631-1646 and was completed in collaboration with the named authors.

- Much of the work contained in Chapter 4 forms the basis of the paper Bonsor, A.; Mustill, A. J. & Wyatt, M. C. Dynamical effects of stellar mass-loss on a Kuiper-like belt mnras, 2011, 414, 930-939 and was completed in collaboration with the named authors. A. J. Mustill was responsible for the encounter map analysis and producing Fig.4.4

- Much of the work contained in Chapter 5 forms the basis of the work to be published as Bonsor, A. & Wyatt, M., The scattering of small bodies in planetary systems, 2011, that is currently in preparation with collaboration with the named authors.

This thesis contains fewer than 60,000 words.

Amy Bonsor

Cambridge, 7th October, 2011

Acknowledgements

Summary
Post-main Sequence Evolution of Planetary Systems

Planetary systems are common around main sequence stars. There are hundreds of detections of planets and analogues to the Solar System's Kuiper belt, known as debris discs, around stars on the main sequence. However, there are very few observations of such systems around evolved stars. An important link has been made between observations of metal pollution and circumstellar discs around white dwarfs and evolved planetary systems. The hypothesis is that asteroids or comets from an outer belt are scattered in close to the star, where they are tidally disrupted and accrete on to the star. The focus of this thesis is on the evolution of planetary systems beyond the main sequence, with relevance to the observations.

Starting from the main sequence, the effects of stellar evolution on debris discs are outlined and it is determined that although such belts of rocks and dust survive the star's evolution, their detectability decreases as the star evolves. A cold, undetected population of outer discs around white dwarfs may supply the observed accretion. Investigations into the effects of stellar mass loss on such a disc find that for Solar System analogues sufficient material is scattered inwards in order to produce the observations. This is, however, highly dependent on the planets' orbits. The conservation of the Tisserand parameter is used to confirm that many planetary systems, with sufficient planets, can scatter particles from an outer belt onto star-grazing orbits. The conservation of the Tisserand parameter in this manner can also be used to describe the scattering of small bodies by planets in any system. I consider both our Solar System and main sequence stars with two belts of rocks and dust, an inner warm belt and an outer cold belt.

All the work presented in this thesis develops our understanding of planetary systems as they evolve beyond the main sequence. Vital evidence is provided in support of a link between main sequence planetary systems and the observations of evolved stars linked with planetary systems, in particular metal polluted white dwarfs and white dwarfs with circumstellar discs.

Amy Bonsor, 7th October 2011

Contents

List of Figures

List of symbols

Symbol	Description / Definition
A	Composition dependent parameter, used in Mestel theory
δa_{chaos}	Width of chaotic zone
a	Semi-major axis
$a_{galatic}$	The semi-major axis at which the galactic tide becomes important
a_{in}	The definition of the semi-major axis at which particles enter the inner planetary system, used in Chapter 4
a_{max}	The maximum semi-major axis in the belt used in Chapter 4
a_{pl}	Planet's semi-major axis
B_ν	Planck function
β_{RAD}	Ratio of force due to the radiation to the gravitational force
β_{SW}	Ratio of force due to the stellar wind to the gravitational force
C_J	Jacobi integral
c	Speed of light
d	Distance from the Earth to the star
D	Diameter of planetessimal or dust grain
D_{bl}	Blow-out diameter
D_c	Diameter of the largest object in the size distribution in the models of Wyatt et al. (2007b)
$D_{cc}(D)$	Diameter of the smallest object that can catastrophically destroy an object of size D
D_{min}	Diameter of the smallest object in the size distribution
D_{max}	Diameter of the largest object in the size distribution
D_{PR}	Diameter of the largest object removed by Poynting-Robertson drag
D_{SW}	Diameter of the largest object removed by stellar wind pressure
D_{SWPR}	Diameter of the largest object removed by stellar wind drag
dr	Disc width
e	Eccentricity

e_{int}	Maximum eccentricity for scattered particles that interact with the inner planet
e_{lim}	Eccentricity for particle's scattered with q_{min}, $I = 0°$
e_{max}	Maximum eccentricity in the initial conditions for the N-body simulations in Chapter 4
	Also maximum eccentricity of scattered particles, determined by the Tisserand parameter
e_{SD}	Maximum eccentricity before particle enters the scattered disc
f	Fractional luminosity
f_{acc}	Fraction of material that is tidally disrupted that accretes onto the star
f_{max}	Maximum fractional luminosity
f_{SI}	Fraction of material "scattered in"
f_{TD}	Fraction of material scattered into the inner planetary system that is further scattered to end up on star-grazing orbits
$F_{disc,\nu}$	Flux density from a disc, at a specific wavelength
F_{grav}	Force due to gravity
F_{rad}	Force due to radiation pressure
F_{SW}	Force due to stellar wind
$F_{\nu\star}$	Flux density from a stellar object at a specific wavelength
F_{ν}	Flux density from a disc at a specific wavelength
G	Gravitational constant
γ	Co-efficient in radial distribution of discs used in Chapter 3
h	Angular momentum
i, I	Orbital inclination
i_{max}	Maximum inclination, in the initial conditions for the N-body simulations in Chapter 4
I_{int}	Maximum inclination for scattered particles that interact with the inner planet
I_{max}	Maximum inclination for particles scattered with a given value of the Tisserand parameter
L	Mean longitude
λ	Wavelength

$L_\star$	Stellar luminosity
L_{WD}	White dwarf luminosity
M	Mean anomaly
m	mass of a small body
$M_\star$	Mass of a star
M_{acc}, $\dot{M}_{acc}$	Mass, and rate at which mass accretes onto star
$M_{analytic}$	Mass of disc that analytic calculations suggest will be scattered in the simulations in Chapter 4
M_{belt}	Mass in belt
M_{EJ}	Mass ejected
M_J	Mass of Jupiter
M_{max}	Maximum mass of a collisionally evolving disc at a given age
M_{mid}	Center of the mass distribution used in Wyatt et al. (2007b) and Chapter 3
M_{Nep}	Mass of Neptune
M_{scatt}	Mass scattered
M_{SD}	Mass in scattered disc
M_{SI}	Mass scattered in
$\dot{M}_*$	Mass loss of a star
$\dot{M}_R$	Rate of Kudritzki and Reimers (1978) mass loss
$\dot{M}_{VW}$	Rate of Vassiliadis and Wood (1993) mass loss
$M(D)$	Mass of objects as a function of diameter
M_{tot}	Total mass in a disc
M_{WD}	Mass of white dwarf
n	Mean motion
$n(D)$	Number of objects as a function of diameter
$n(r)$	Number of discs with radii between r and $r + dr$
N_{RH}	Separation of planets in units of Hill's radii
ω	Argument of pericentre
Ω	Longitude of ascending node
ϖ	Longitude of pericentre
ϕ	Resonant angle
P	Pulsation period

q	Size distribution power law index for a single slope distribution
q	Pericentre
q_{min}	Minimum pericentre to which particles can be scattered
Q	Apocentre
Q_{abs}	Absorption efficiency
Q_D^*	Dispersal threshold
Q_{pr}	Efficiency of radiation pressure transfer
Q_{SW}	Efficiency of stellar wind pressure transfer
ρ	Density of a particle
$\mathbf{r}$	Position vector of an object
r	Radial distance to star or disc radius
r_{2470}	Disc radius calculated using a black-body approximation
r_H	Hill's radius
r_{real}	Disc radius calculated using realistic grains
r_{min}, r_{max}	Maximum and minimum radii in the distribution of disc radii, used in Chapter 3
r_{real}	Radius of disc calculating using realistic grains
R_{col}	Collision rate
R_{cc}	Catastrophic collision rate
R_ν	Ratio of the disc to stellar flux, at a given wavelength
$R_{\nu,lim}$	Calibration limit of instrument, at given wavelength
$\sigma(D)$	Cross-sectional area as a function of diameter
$\bar{\sigma}(D)$	Cross-sectional area as a function of diameter normalised to the total cross-sectional area
σ_{tot}	Total cross-sectional area in a disc
σ	Cross-sectional area of a particle
t	Time
t_{MS}	Main-sequence lifetime
θ	True longitude
dt	Time interval
t_c	Collision timescale
t_{cool}	Cooling age of a white dwarf
t_{pr}	PR drag timescale

t_{SW}	SW drag timescale
T	Temperature
T_{BB}	Black-body temperature
T_p	Tisserand parameter with respect to the planet labelled by p
$T_{2,min}$	Minimum value of the Tisserand parameter for particles scattered by planets 1, 2
$T_{1,new,min}$	Minimum value of the Tisserand parameter for particles scattered by planets 1 and 2 and then passed back to the outer planet 1
$T_\star$	Temperature of a star
μ	G m
v_{col}	Relative velocity of a collision
v_{SW}	Velocity of the stellar wind
(x, y, z)	Co-ordinates in a frame rotating with angular velocity n, centred on the centre of mass
X_{2470}	Ratio of radius calculated using realistic grains r_{real} to radius calculated using a black-body approximation
Z	Stellar metallicity

Chapter 1

Introduction

The discovery of planets around stars other than our Sun has sparked our imaginations, in particular with the prospect of discovering a system that resembles our own Solar System or planet Earth. As we learn more about exoplanetary systems, we develop our understanding of our own planetary system. We can compare it with the newly discovered systems in order to better place our Solar System in context and help to answer some of the bigger questions such as whether or not our Solar System is unique and whether life on Earth is a special, rare or common occurrence.

In my thesis I focus on one aspect of this huge field; the ultimate fate of planetary systems. Main-sequence stars, such as our Sun, evolve off the main sequence to become giants, asymptotic giants and white dwarfs. The effects of such evolution on a planetary system can be dramatic. A theoretical understanding of how a planetary system reacts to such changes, in a way that matches the observational constraints, will not only greatly improve our knowledge of how planetary systems evolve, but will help us to determine the fate of our own Solar System and the planet Earth.

In the next section, I firstly briefly outline the current state of observations and theory regarding main-sequence planetary systems, both planets and asteroid or comet belts, known as debris discs. A more detailed discussion of debris disc theory can be found in Chapter 2. I then discuss the evolution of the star, its effects on the planetary system and our current knowledge of planets around

evolved stars. I finish this chapter by presenting details of observational signatures that have been linked with planetary systems.

1.1 Main Sequence planetary systems

1.1.1 Planets

With over 486^1 detections of exoplanets over the last ~ 20 years, our characterisation of exo-planetary systems is growing rapidly. However, huge gaps in our knowledge and understanding still remain.

There are a variety of ways to detect planets, each with its own advantages and disadvantages. The most commonly used technique, known as the **radial velocity (RV)** method, involves searching for a Doppler shift in the stellar emission, caused by movement of the star about the common star-planet centre of mass. This is most sensitive to high mass planets on short period orbits, although only a lower limit on the planet mass can be determined. A wealth of hot Jupiters have been discovered using RV measurements. RV is often used to confirm detections by the next most commonly used technique, **transits**. As the planet passes in front of the star there is a dip in the stellar luminosity. Transit detections are particularly suited to determining the planet radius, density and potentially the inclination. The main problem with transit detections is that they can easily be confused with other signatures and therefore follow-up observations are required. *Kepler* [2], a space satellite designed to detect a transit of an Earth mass planet, will vastly increase the number of transit detections during its lifetime. A handful of other techniques exist to detect planets, including directly imaging the planet, microlensing, astrometry and timing methods, although the number of detections is low.

Fig. 1.1 shows the current planet detections. As can be seen, high mass planets on close-in orbits are readily detected, whilst the current observational capacities make it hard to detect low-mass or wide orbit planets. Both RV and transit observations are more sensitive to massive planets on short period orbits. We are

---

[1] 7th October 2011 http://exoplanets.org (Wright et al., 2011)
[2] see http://kepler.nasa.gov for details
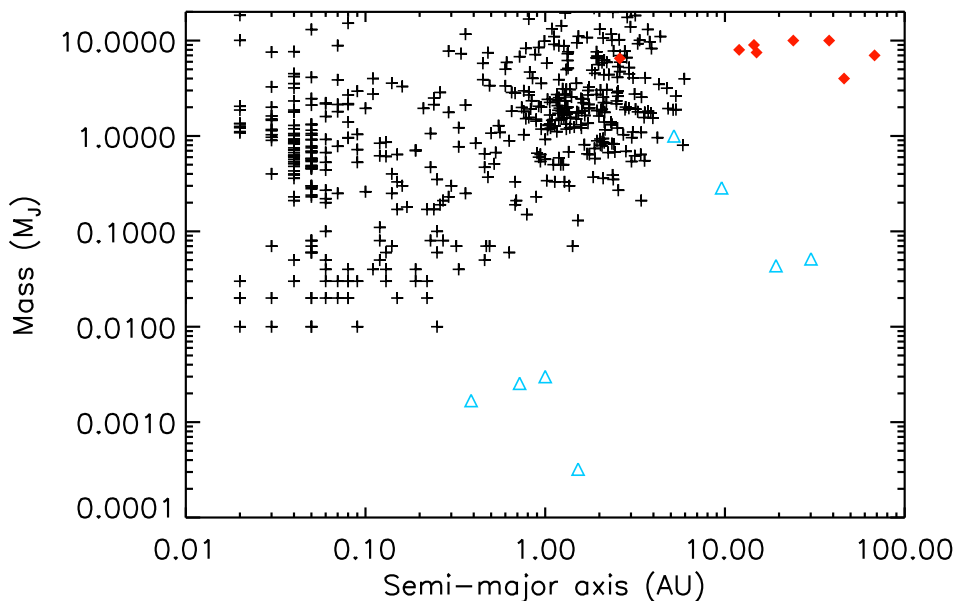
Figure 1.1 – The current planet detections are shown as black crosses, from http://www.exoplanet.org as of 7th October 2011, in terms of their masses and semi-major axis. The Solar System planets are included in blue, whilst the red diamonds label those planets detected by direct imaging.

starting to probe outer planetary systems using direct imaging (shown in red on Fig. 1.1). From Fig. 1.1 it is very clear that there are huge regions of parameter space that have not yet been probed by observations, including the region in which the Solar System's planets reside. Although a large proportion of the observed planets reside in multi-planet systems[1], taking the example of our Solar System as a precedent, it seems likely that there remain further undetected planets in the majority of systems. Many stars with planet detections are also found to have dust discs, potentially signatures of comet or asteroid belts. According to Krivov et al. (2011), 2-4% of transiting planets have warm infrared excess, a signature of a dust disc, observed with WISE.

---

[1]Currently 115 of 486 planets **http://exoplanets.org** as of 7th October 2011
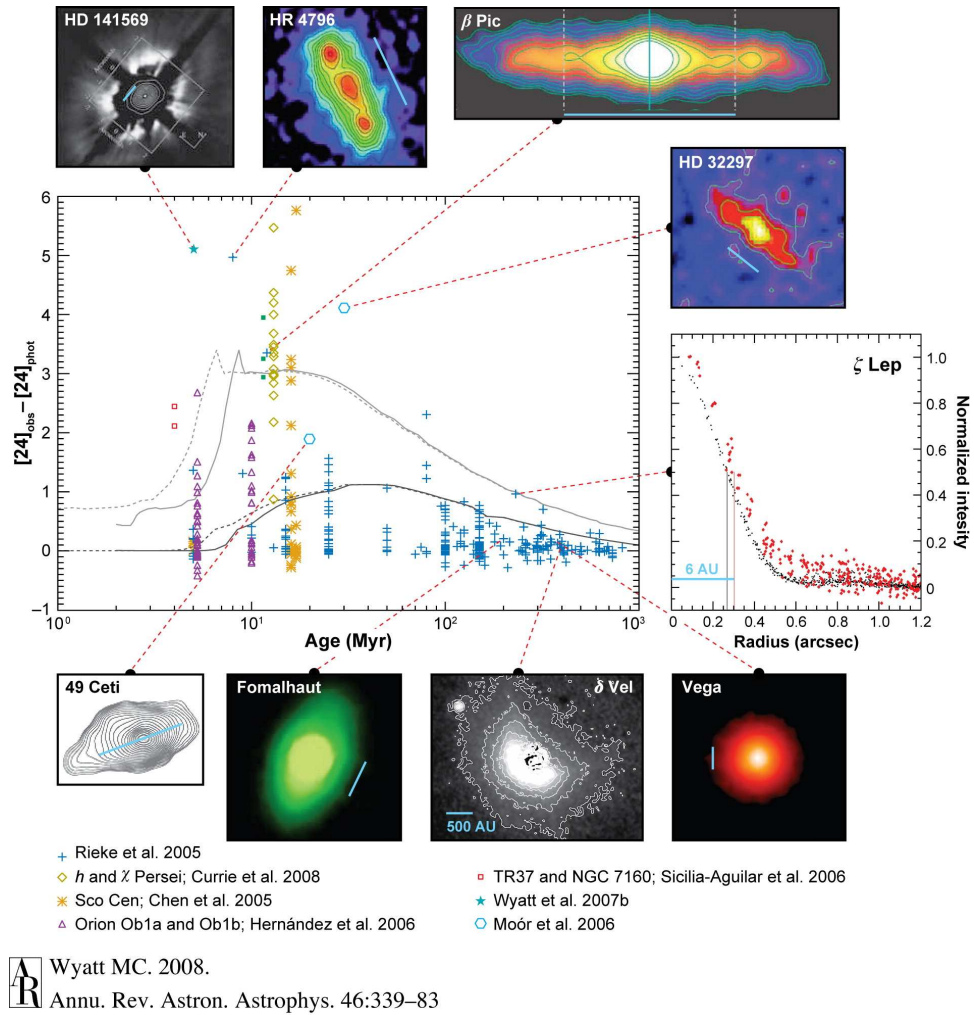
Figure 1.2 – Main-sequence A stars with infra-red excess detected with Spitzer at 24μm. The fractional excess is shown as a function of the system age. The insets show a handful of these systems where the dusty debris disc has been resolved.

1.1.2 Planetesimal belts around main-sequence stars

The first detection of an exo-planetary system was actually the detection of a dust disc around Vega in 1984 (Aumann et al., 1984). Similar dusty discs have now been observed around hundreds of main-sequence stars. They are analogues to the Solar System's asteroid or Kuiper belt and known as debris discs.

Such systems were originally detected by their emission in the infrared, over and above that expected from the stellar photosphere. This is thermal emission from dust particles in a belt orbiting the star. The disc-like nature of such systems has been confirmed by resolved imaging (Smith and Terrile, 1984). Fig. 1.2 shows hundreds of detections of such discs around main-sequence A stars with Spitzer at 24μm, a handful of which have been resolved, shown on the insets. Debris discs are characterised by the level of their emission compared to the star's, or their fractional excess, which is shown in Fig. 1.2 as a function of the stellar age.

Resolved imaging of debris discs find a variety of features including brightness asymmetries, clumps and warps. More detailed modelling of these observations can tell us a lot about an individual planetary system. Many of the features are thought to be a product of interactions between planetesimals in the belt and planets. Observations suggest that systems with both planets and debris discs are common (HR 8799 Su et al. (2009); Marois et al. (2008), Fomalhaut (Kalas et al., 2005, 2008), HD 69830 (Lovis et al., 2006; Beichman et al., 2005), amongst many others). Planets can shape a debris disc; potentially sculpting its inner edge, (*e.g.* Su et al. (2009); Chiang et al. (2009); Quillen (2007)), trapping bodies in resonance to produce clumps (*e.g.* Wyatt (2003)), inducing an eccentricity (*e.g.* Fomalhaut Chiang et al. (2009)), causing brightness asymmetries (*e.g.* Wyatt et al. (1999)) or warps (*e.g.* Augereau et al. (2001)). These interactions give us vital clues about the planets orbiting a given star potentially before they are detected by other means. Chapter 2 provides a more detailed description of debris disc evolution and modelling.

1.2 The star evolves

The main-sequence stars described in the preceding section will evolve off the main sequence. This evolution can have dramatic consequences for the planetary system. In this section I discuss the evolution of the star and the potential consequences for the planetary system, whilst summarising our current knowledge of planetary systems around such stars, focusing on planet detections. I reserve the important discussion of asteroid or comet belts and further signatures of planetary systems to §1.3.

The main stages of stellar evolution are outlined on the Hertzsprung-Russell diagram shown in Fig. 1.3. The full evolution of a star is a complicated process that is by no means fully understood. It is very dependent on the star's initial mass and chemical composition. However, for the purposes of the work presented in this thesis, the fine details of stellar evolution are not important. I am concerned with the well-understood broad changes to the star as it evolves, with a focus on their consequences for the planetary system. For this reason in this thesis I make use of simple theory and a stellar evolution code (Hurley et al., 2000) that uses analytic formulae to approximate the evolution of stars. This code produces very good models for stars on the main sequence, whilst its ability to model the stages of evolution where there are rapid changes, for example the giant and asymptotic giant branch, is more limited. It does not fully model the details of the star's evolution towards the tip of the asymptotic giant branch where thermal pulses and super-wind phases may be important. However the fine details of these rapid changes do not significantly affect the general evolution of the planetary system.

The typical luminosities and timescales for stars at various points in their evolution, calculated using this code, are summarised in Table 1.1.

1.2.1 Giants

Giant stars are characterised by hydrogen shell burning. During the giant branch the stellar luminosity increases by approximately an order of magnitude. The stellar envelope expands and the star cools. The star moves up and to the right on the HR diagram (Fig. 1.3). The increase in stellar luminosity heats close-in
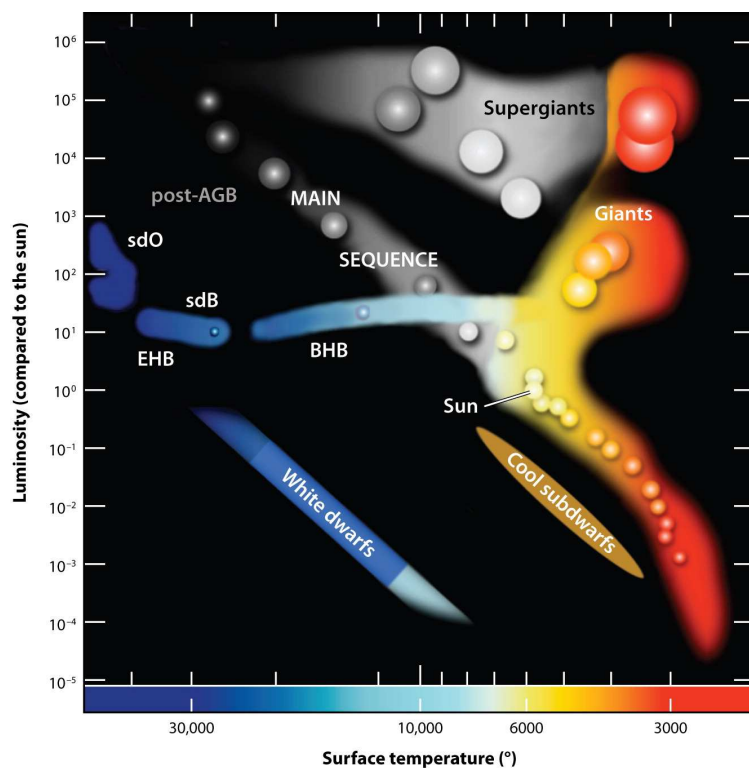
Heber U. 2009.
Annu. Rev. Astron. Astrophys. 47:211–51

Figure 1.3 – A HR diagram to show the evolutionary phases of a star. EHB: Extreme horizontal branch, sdO: sub-dwarf O, sdB: sub-dwarf B, BHB: blue horizontal branch.

Phase	Mass $M_\odot$	Luminosity $L_\odot$	Radius AU	Lifetime Myr
Main sequence	1	1	0.0046	10,000
	5	10^3	0.002	100
First ascent giant branch	1	10^3	0.7	800
	5	2×10^3	0.5	0.5
Asymptotic giant branch	1	4×10^3	0.9	5
	5	4×10^4	5	1
White dwarf	0.5		5×10^{-5}	
	1		5×10^{-5}	

Table 1.1 – Stellar evolutionary models (Hurley et al., 2000).

planets, potentially causing their atmospheres to heat and planets to become bloated (Assef et al., 2009).

The increase in the stellar radius also has important consequences for the planetary system. As the star swells, up to $\sim$ 1AU, any planets orbiting close to the star may be engulfed by the expanding stellar envelope. Tidal forces on close-in planets increase. Villaver and Livio (2009) find that all planets within 3 and 0.45 AU, for a 1 or $5 M_\odot$ star, respectively, will spiral in and be engulfed. This difference dependent on the stellar mass results from the decrease in stellar radius with increasing stellar mass (see Table 1.1) and the strong dependence of the tidal force on the stellar radius. The destruction of an engulfed planet, however, is not certain and it may be that some planets survive inside the stellar envelope, potentially accreting mass (Soker et al., 1984; Siess and Livio, 1999). It has even been suggested that low-mass companions to evolved stars may be planets that have accreted mass (Livio and Soker, 1984). There are observations of planets on small enough orbits around evolved stars that they must have survived inside of the stellar envelope; for example, the planet HD 149382b, on a 2.391 day orbit around an extreme horizontal branch star, would have been inside the stellar envelope on the giant branch (Geier et al., 2009).

The techniques for detecting planets around giant stars do not differ significantly from those for main-sequence stars. Transit signals are longer in duration and smaller in amplitude. There are, however, as yet no detections (Assef et al., 2009). Radial velocity techniques, on the other hand, have been relatively successful. There are a fair number of detections and programs currently searching for planets around giant stars *e.g.* Sato (2005); Döllinger et al. (2007); Johnson et al. (2007, 2008); Jones et al. (2011). These observations make it possible to assess the planet population around A stars, where observations on the main sequence are difficult because of rotationally broadened absorption features and high jitter levels (Galland et al., 2005; Lagrange et al., 2009). The results so far suggest that planets are more common around giants than main-sequence stars. This is probably a result of differences in formation environments, rather than an effect of stellar evolution. The sample of giant stars searched for planets, in general, have higher stellar masses than their main-sequence counterparts (Lovis and Mayor, 2007). There is also a paucity of close-in planets (Sato et al.,

2010). This is a predicted consequence of stellar evolution, although models for the destruction of close-in planets around evolved stars find that the absence of planets extends to larger radii than anticipated (Kunitomo et al., 2011; Villaver and Livio, 2009).

1.2.2 Core-helium burning or horizontal branch stars

Once the core reaches high enough temperatures to ignite helium burning, the stars move off the giant branch. Stars less than around $2M_\odot$ start helium burning degnerately in a helium flash. The luminosity of core-helium burning stars is higher than on the main sequence, but of the same order of magnitude and remains fairly constant during this phase. Core-helium burning lasts for a slightly shorter, but similar timescale to the main-sequence evolution. Instabilities may develop, leading to periodic pulsations that may be observed by changes in the stellar luminosity, temperature or radius. These provide a useful clock for determining more information about companions to the star.

Planets around such stars must have survived the full giant branch evolution and are therefore expected to have large orbital radii. The only detection of a planet on the red horizontal branch is HIP 13044 (Setiawan et al., 2010), identified as being at the blue edge of the red horizontal branch on a colour magnitude diagram. This detection is particularly significant because of the star's probable extragalactic origin and low metallicity. If the planet has evolved from the main sequence, then its orbital radius of 0.116AU (Setiawan et al., 2010) suggests that it may have survived inside the stellar envelope. Alternatively, its orbit may have decayed significantly due to tidal interactions.

1.2.2.1 Extreme horizontal branch stars

A very interesting class of objects are B type subdwarfs (sdB), stars that are on the extreme horizontal branch (see Heber (2009) for a review). These stars have undergone extreme mass loss on the giant branch. The exact mechanism that led to the premature ejection of the stellar envelope is not clear. One possibility is a common envelope phase with a binary companion. $60 \pm 8\%$ of such stars have a known binary companion (Maxted et al., 2001). A similar evolutionary path has

been suggested for the remaining stars, except that the perturbation leading to the premature ejection of the stellar envelope comes from a planetary companion (Soker, 1998). Alternative suggestions, including the merger of two helium white dwarfs, have been made (Heber, 2008).

There are a handful of detections of planetary mass companions to extreme horizontal branch stars, including Silvotti et al. (2007); Lee et al. (2009); Geier et al. (2009). These were found by searching for changes in the timing of the periodic stellar pulsation as a result of the movement of the source around the common planet-star centre of mass. This technique is very difficult as it requires a stable phase of pulsation to be identified (Silvotti et al., 2011b). A degree of scepticism remains for some of these detections; for example the 18-23 M_J planet found around HD 149382 (Geier et al., 2009) was not found by Jacobs et al. (2011). However, the future prospects for further detection of such systems are high and will help our understanding of the formation scenario for sdB stars (Silvotti et al., 2011b; Geier et al., 2011; O'Toole et al., 2011).

1.2.3   Asymptotic giant branch (AGB)

Asymptotic giant branch stars resemble in many respects stars on the first ascent giant branch and observationally they are hard to distinguish. The effects on the planetary systems are also very similar; heating and engulfment of close in planets. These effects can, however, be more severe as the star's luminosity can increase by up to an order of magnitude more than on the first ascent giant branch and the stellar radius may reach several AU. AGB stars are characterised by alternate phases of hydrogen and helium shell burning and during the late AGB the star may pulsate thermally.

Of dramatic consequence for planetary systems around AGB stars is the stellar mass loss. Although giant stars also lose mass, mass loss rates are low and their effects on planets are not dramatic. During the AGB the star may lose over 50% of its mass. Generally mass loss rates are slow compared to the orbital timescales for planets. Such adiabatic mass loss causes planetary orbits to expand gently and, depending on the system architecture, may cause dynamical instabilities (Debes and Sigurdsson, 2002). The majority of the stellar mass is lost in a super-wind

phase towards the end of the AGB. This can lead to planetary orbits expanded by a factor of 2 or 3. For some stars, or long period planetary orbits, the mass loss is no longer adiabatic and may have drastic consequences including the ejection of material (Veras et al., 2011). This is discussed in more detail in §2.1.3. The exact mechanism and rates for mass loss are poorly understood (see Willson (2000) for a review). A variety of empirical formulae fitted to observational data exist in the literature *e.g.* Kudritzki and Reimers (1978); Vassiliadis and Wood (1993).

1.2.4 White dwarfs

The end fate of the star depends on its initial mass. Since the majority of planets are discovered around low-mass main-sequence stars, I focus on such stars, which end their lives as white dwarfs. Temperatures in the cores are never high enough to ignite carbon and therefore the removal of the stellar envelope at the end of the AGB reveals a carbon-oxygen degenerate core. The UV radiation from this hot core is sufficient to ionize the expanding stellar envelope, which is seen as a planetary nebula. The exposed core is initially hot and luminous, but cools rapidly to become a white dwarf.

White dwarfs are classified observationally from their spectra; those with only hydrogen absorption lines are known as DA white dwarfs, whilst those with only helium absorption lines are known as DB white dwarfs and those with no detectable lines, DC. This classification scheme has become more complicated as more unusual white dwarfs have been detected, for example DBA stars with mainly helium lines, but also some hydrogen features, DQ white dwarfs with carbon lines and DAZ, DBZ or DZ white dwarfs with metal lines. These absorption lines come from the white dwarf's thin atmosphere, containing, for a DB white dwarf only $\sim 0.001 M_{WD}$, where M_{WD} is the white dwarf mass. DA white dwarfs have a helium atmosphere covered by a thin layer of hydrogen ($\sim 0.0001 M_{WD}$).

There are currently no planet detections around white dwarfs, although a few candidates exist, *e.g.* GD66 (Mullally et al., 2008, 2009) and GD356 (Wickramasinghe et al., 2010). A few planets exist in main-sequence - white dwarf binaries, including HD 13445, HD27442, HD147513 (Desidera and Barbieri, 2007) and the pulsar-white dwarf system PSR 1620-26 (Thorsett et al., 1999).

If planets around white dwarfs have evolved from the main-sequence then large orbital radii are anticipated as a consequence of stellar mass loss. Such far out planets are hard to detect by either radial velocity measurements or transits. Super-WASP failed to detect any transits in their small survey of 194 white dwarfs, despite being sensitive to Mercury sized bodies, although only within 0.1AU (Faedi et al., 2011). Direct imaging and astrometry are better suited to detecting white dwarf planets. There are no detections at present; however, the prospects are good, with programs such as DODO (Burleigh et al., 2008) and GAIA. GAIA should be able to astrometrically detect planets as small as $0.7M_J$ around the 50 brightest white dwarfs, and masses larger than $2M_J$ for all white dwarfs within 100pc (Silvotti et al., 2011a).

1.2.5 Neutron stars and pulsars

Stars more massive than $\sim 8M_\odot$ end their lives in a more dramatic manner. Their cores reach sufficient temperatures that nuclear burning occurs for all elements up to iron and the star explodes as a supernova. The compact iron core becomes a neutron star. Pulsars are an interesting class of magnetic neutron stars that pulsate regularly. The pulse period varies between milliseconds and seconds, with a distinct class of millisecond pulsars, thought to have been spun up by accretion of material from a binary companion. The first planets to be detected are actually in orbit around a millisecond pulsar (Wolszczan and Frail, 1992; Wolszczan, 1994). Since then, there has been one further detection of a pulsar planet (Backer et al., 1993). Many suggestions have been made in the literature regarding the origin of these planets, including their formation in a disc produced after the supernova explosion from fallback material or a disrupted companion, as well as their survival from the main sequence (Podsiadlowski, 1993).

1.2.6 Binary stars

So far all of the discussion has focused on single stars. Less than 30% of solar type stars in the solar neighbourhood are truly single (Duquennoy and Mayor, 1991) and depending on the separation, this can have consequences for the planetary system or the star's evolution.

Binaries exist at a wide range of separations. Generally the consequences for a planetary system are minimal if the binary is very widely or very closely separated, with circumbinary planetary orbits in the latter case. A binary companion can inhibit planet formation and alter the dynamics of orbiting planets (see Haghighipour (2009) for a review). 57 out of 486 planets detected are in systems with more than one star (Wright et al., 2011)[1], although few of these planets are significantly affected by the stellar companions. Of the observations considered in Chapter 3, all of the white dwarfs with circumstellar discs and the majority of metal polluted white dwarfs are single stars, although a handful of close red dwarf- white dwarf binaries show evidence of accretion of heavy elements from the companion (Zuckerman and Reid, 1998; Zuckerman et al., 2003). For simplicity and clarity, because the majority of planetary systems are minimally affected by their binary companions, the discussion in this thesis focuses on single stars.

A close binary companion can alter the evolutionary path of a star. Mass transfer via Roche lobe overflow is a common feature of many binary systems, as one star swells to become a giant (see Boyle (1984) for a review). As material accretes on to a companion, this can alter its evolution, for example setting off a Type Ia supernova. According to Perets (2010) the accretion disc on to the companion may be the site of second generation planet formation. Given the altered dynamics of the evolved system, planets may form in regions that were *forbidden* on the main sequence. This potentially allows second generation planets to be distinguished from first generation planets. One example is the $4\mathrm{M}_J$ planetary companion to Gliese 86 (Queloz et al., 2000), a main-sequence star with a white dwarf (or potentially brown dwarf) (Lagrange et al., 2006). This planet is in a region that would have been unstable for planet formation before the binary system evolved (Perets, 2010). Some of the handful of tentative circumbinary planet detections around post-main sequence binaries (*e.g.* (Beuermann et al., 2010, 2011; Qian et al., 2011) *etc*) may also be second generation planets.

A binary companion may also be the explanation behind observations of post-AGB stars, with circumbinary discs or shells (see van Winckel (2003) for a review). Post-AGB stars are in the short phase between the end of mass loss on the AGB and the ionization of the ejected stellar envelope, seen as a planetary nebula. The

---

[1]http://exoplanets.org as of 7th October 2011

circumstellar dust disc or shell emits strongly in the infra-red and a handful of such objects have been confirmed to have stable Keplerian discs (Bujarrabal et al., 2005, 2007; de Ruyter et al., 2006). There is also observational evidence for the growth of sub-mm grains (Gielen et al., 2008), which led to the suggestion that these discs could be another site for second generation planet formation (Perets, 2010).

1.3   Observations of evolved stars associated with planetary systems

Given the difficulties in detecting planets, other signatures that tell us about the presence and nature of the planetary system are incredibly important. For main-sequence stars, modelling of observations of debris discs gives us clues as to the structure of the planetary system. Around evolved stars, where there is a dearth of planet detections, such signatures are critical for our knowledge and understanding of evolved planetary systems. For white dwarfs there are two key signatures that suggest the presence of a planetary system: excess emission in the infra-red from a dust disc and the presence of unexpected metal lines in their spectra.

1.3.1   Cold dust discs

Debris discs on the main-sequence are detected in the first instance by excess emission in the infrared, over and above that expected from the stellar photosphere. The observations are well modelled by an optically and geometrically thin dust disc. The dust is second generation, produced in collisions between larger planetesimals. These discs are often considered analogues of the Solar System's Kuiper belt. The inner region of debris discs has generally been cleared and thess discs lie between ~ 3 and 200AU. The disc-like nature of such sources has been confirmed by resolved imaging. If such systems survive the star's evolution, then similar infra-red emission would be seen around evolved stars.

Giant stars with excess emission in the infra-red have been detected. Plets and Vynckier (1999) found that $14 \pm 5\%$ of their sample of G and K giants have
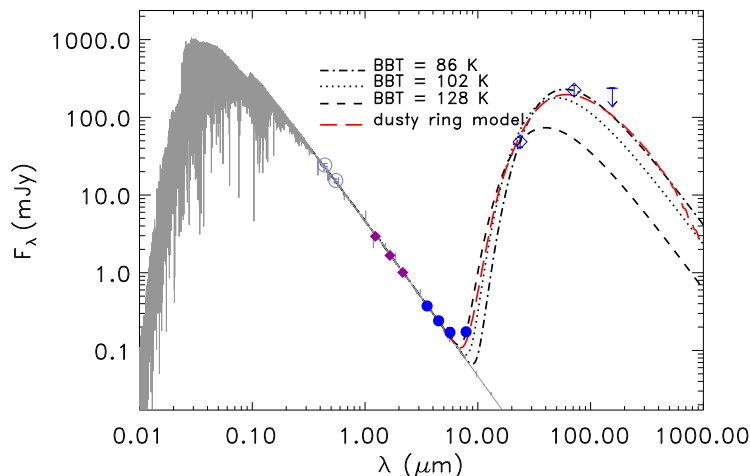
Figure 1.4 – A spectral energy distribution (SED) for the Helix nebula (Su et al., 2007) showing the excess emission in the infra-red, consistent with a dusty disc, similar to debris discs seen on the main sequence. The emission from the disc is shown as a blackbody with temperatures of 86K, 102K and 128K, as well as a more sophisticated dusty ring model, details of which can be found in (Su et al., 2007).

excess emission, whereas Zuckerman et al. (1995) find excess emission around only 300 of 40,000 ($\sim 0.08\%$) class II luminosity stars. It is plausible that this emission is from a debris disc; however more detailed modelling of 12 sources (Kim et al., 2001a) find the emission to be spatially resolved with radii of several thousand AU. This is very different from main-sequence debris discs and more likely to be emission from interstellar cirrus hotspots or dust shells ejected when the giant star sporadically loses mass.

Excess emission, very similar in nature to that seen for main-sequence debris discs, has been detected with Spitzer at 24μm around a handful of white dwarfs (Su et al., 2007; Chu et al., 2011). These are all very young white dwarfs; about half of the Chu et al. (2011) sample are still the central stars of planetary nebulae. The first such system to be detected was the Helix nebula (Su et al., 2007), a young white dwarf at the centre of a planetary nebula, where excess emission was observed at both at 24 and 70μm, with an upper limit at 160μm. The spectral energy distribution, shown in Fig. 1.4, can be fitted in a similar manner to main-sequence debris discs, giving a radial extent of 35 to 150AU. The sources

in Chu et al. (2011) are only detected with Spitzer at 24μm and require follow-up observations, scheduled with *Herschel*, before their disc-like nature can be confirmed.

Such excess emission around white dwarfs could be a signature of an evolved main-sequence debris disc, a hypothesis that is discussed further in Chapter 3. One suggestion to explain the unexpectedly high emission from these sources is that they are main-sequence like debris discs where the density of material is enhanced by the trapping of small bodies in resonances with inner gas giant planets (Dong et al., 2010). Alternatively, a potential link between these observations and stellar duplicity has been suggested (Chu et al., 2011), in a similar manner to the explanation for post-AGB discs, as discussed in §1.2.6.

1.3.2 Metal polluted white dwarfs

Elements heavier than helium sink rapidly in white dwarf atmospheres on timescales significantly shorter than the evolutionary timescales for the star. For hot, hydrogen-rich DA white dwarfs, this can be as little as days or weeks, whereas for helium rich, DB, white dwarfs, typical timescales are generally longer, hundreds of years for young stars and up to $\sim 10^6$yr for older white dwarfs (Koester and Wilken, 2006). It is therefore surprising that such a large fraction of white dwarfs have detectable calcium, magnesium, iron, *etc*, lines. Zuckerman et al. (2003) find 25% of the DA white dwarfs in their sample have CaII lines, whilst Zuckerman et al. (2010) classify $\sim \frac{1}{3}$ of the DB white dwarfs in their sample with $13,500$ K $< T_{eff} < 19,500$K, as DBZ; *i.e.*, with metals in their atmospheres. Even including the potential effects of radiative levitation (Chayer et al., 1995; Chayer and Dupuis, 2010), the observed elements sink too rapidly under gravity for the observed abundances to be accounted for without the recent accretion of material.

The presence of small quantities of heavy elements in some white dwarfs has been known for years and was originally associated with the accretion of material from the interstellar medium (ISM); *e.g.*, Dupuis et al. (1992, 1993); Aannestad et al. (1993). However, there is growing evidence against this theory. First, Farihi et al. (2010a) found a lack of correlation between positions and/or velocities
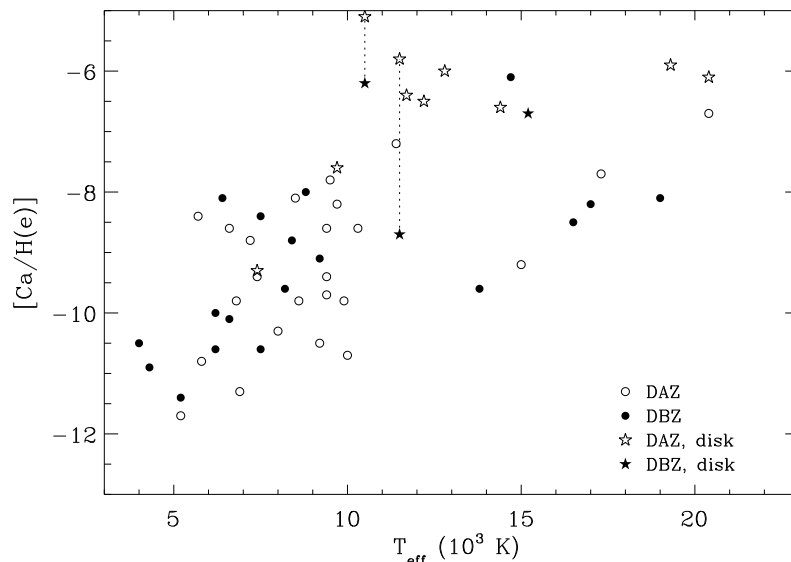
Figure 1.5 – The calcium abundances of polluted white dwarfs, relative to hydrogen (DAZ- open circles) and helium (DBZ- filled circles), as a function of their stellar temperature. Those white dwarfs that also have an infrared excess are shown as stars. Farihi et al. (2009)

of polluted white dwarfs in comparison with a non-polluted sample. Secondly, the composition of the accreted material, determined from spectral fitting of the emission lines, resembles more closely asteroidal or planetary material than interstellar grains; for example, GD40 (Klein et al., 2010). If this material is planetary, then these compositions are the best compositions determined so far for any planetary material outside of our Solar System.

The best explanation to account for this anomalous presence of metals is that planetary material has been (or is currently being) accreted on to the star. The effects of stellar evolution on a planetary system are numerous and include potential dynamical instabilities after stellar mass loss on the giant branches (Debes and Sigurdsson, 2002). Such instabilities could scatter asteroidal or cometary bodies on to star-grazing orbits, a phenomenon which is discussed further in Chapter 4. Comets, asteroids or planets that end up on orbits that approach within the tidal radius of the star are torn apart by tidal forces. Material rich in heavy elements from such tidally disrupted comets accretes on to the star.

This model has been outlined in, amongst others, (Alcock et al., 1986; Debes and Sigurdsson, 2002; Jura, 2003; Gänsicke et al., 2006; Kilic et al., 2006; von Hippel et al., 2007b; Farihi et al., 2009, 2010b; Melis et al., 2010) and is supported by observations of circumstellar material within the tidal radius of ~ 20 white dwarfs, discussed further in §1.3.3. Such discs are thought to be formed from the disrupted material and feed the accretion.

If this hypothesis is correct then the flux of asteroids or comets scattered on to star-grazing orbits would decrease with time, as the planetary system stabilises. This would reduce the metal accretion rates of older white dwarfs, a trend seen in the observations of Farihi et al. (2009) (see Fig. 1.5), although new larger samples of metal polluted white dwarfs question the validity of this correlation (Koester et al., 2011). Such a correlation provides good evidence in support of the dynamical settling of the planetary system after stellar mass loss, particularly because the observational bias makes it easier to detect metals in cooler white dwarfs. Further confirmation of this hypothesis will be discussed in Chapter 4.

1.3.3   White dwarfs with close-in, circumstellar discs

Spitzer observations of white dwarfs in the near-infrared have found excess emission over and above that expected from the stellar photosphere (Reach et al., 2005; von Hippel et al., 2007b; Kilic et al., 2006; Farihi et al., 2009; Melis et al., 2010) *etc.* In a similar manner to excess emission found around main-sequence stars, this emission is associated with a dust disc orbiting the star. Unlike main-sequence debris discs, which have typical radii of $3-100$AU, these discs are very hot ($\sim 1,000$K) and close to the star ($r \sim R_\odot$), as shown in the example spectrum of GD16 in Fig. 1.6. Another explanation that has been suggested for the observed emission is that we are observing a dust disc around a companion, potentially material from the stellar wind accreting on to the companion star. The lack of even brown dwarf companion detections around these white dwarfs (*e.g.* Kilic et al. (2006)) suggests that this is unlikely.

These observations can be modelled in the same way as main-sequence debris discs using an optically thin model, as in Reach et al. (2005). However, it seems more likely that they resemble Saturn's rings and a flat, passive, opaque circum-
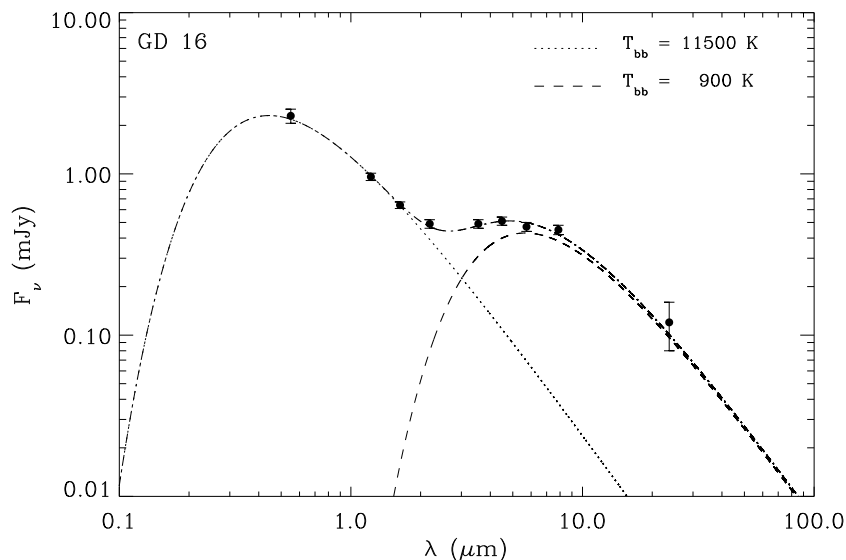
Figure 1.6 – A spectral energy distribution for the polluted white dwarf GD16 (Farihi et al., 2009). The stellar spectrum can be approximated by a single temperature black body at 11,500K, whilst the emission from the disc is approximately a single temperature blackbody at 900K.

stellar disc, such as that used in the models of Jura (2003); Becklin et al. (2005); Jura et al. (2007), amongst others, is more suitable. A tentative estimate for the minimum disc mass can be made from these models. A typical (large) estimate is the 2×10^{23}g of G29-38 (Jura, 2003), equivalent to a ~ 200km asteroid. Discs masses are very uncertain; in particular if the discs are optically thick, then the mass could be significantly higher.

Such dust discs cannot have survived the star's evolution, nor can they survive on long timescales against collisions, PR-drag or viscous coupling between the dust and gas, in the case of a gaseous disc, in their current position. This implies a recent origin. As discussed in the preceding section (§1.3.2), the best model suggests that the discs are formed when asteroids or comets are scattered close enough to the star that they are tidally disrupted. The disrupted bodies form and replenish the observed discs, from where planetary material accretes on to the star. This is supported by the fact that all the white dwarfs with circumstellar discs are also metal polluted. There are, however, many more polluted than dusty

white dwarfs. One possibility is that these stars also possess discs that are too faint to be detected. This could be because the disc mass is too low, in which case it would be reasonable to anticipate a lower accretion rate, which fits with the fact that the majority of white dwarfs with dust discs have the highest accretion rates or levels of pollution (Fig. 1.5). There are, however, a handful of heavily polluted systems without dust discs. Another possibility to explain these systems is that they have discs that are inclined to our line of sight and thus faint and not detectable. For example, one of the faintest detected discs PG 1457-086, a narrow ring of width $0.01R_{\odot}$, would not be detected if its inclination were more than $i = 50°$ (Farihi et al., 2010b). Such a disc could hide over 10^{22}g of material, and supply metals at 10^9g s^{-1}, one of the highest calculated accretion rates for metal-rich white dwarfs, for 10^6yrs (Farihi private communication).

It is not clear whether the observations of metal pollution and circumstellar material are a steady state or transient phenomenon. It is possible that stellar mass loss destabilises a planetary system such that there is a steady stream of asteroidal or cometary bodies scattered on to star-grazing orbits. In order to maintain the observed high accretion rates, the amount of material required during the white dwarf's lifetime is large, for example $2M_{\oplus}$ by the age of GD362 (Becklin et al., 2005). Another possibility is that we are observing these systems at a special time, after a recent scattering and disruption of an asteroidal or planetary body. In which case a disc will be formed with a finite, relatively short, lifetime after which all of the material will be accreted on to the star. Hence, some of the polluted stars without dust discs may have already accreted their discs.

1.3.4   White dwarfs with gaseous discs

This picture has been further complicated by the discovery of gaseous discs around a handful of white dwarfs. Gänsicke et al. (2006) found the first detection of unusual calcium emission lines from the metal polluted white dwarf SDSS J1228+1040, which was later found to also have a dust disc (Brinkworth et al., 2009). The double peaked shape of the calcium triplet is distinctive of gas in a stable, rotating, Keplerian disc. Such a signature is common in accreting bi-

naries, although none of these stars show evidence for a stellar-mass companion. There are five more white dwarfs with gaseous discs (Gänsicke, 2011; Gänsicke et al., 2007, 2008), although further searches suggest this is a rare phenomenon (Gänsicke et al., 2007).

It seems plausible that such gaseous discs are related to the tidal disruption of planetary bodies, the circumstellar dust discs and the pollution of the white dwarfs. One possibility is that the gas disc results when dusty material sublimates. The problem with this is that the observations find that the gas disc is outside the sublimation radius for calcium. Melis et al. (2010) model emission from SDSS1228, Ton 345 and SDSS1043 to find that the observations are consistent with the same spatial position for the gas and dust discs (Melis et al., 2010). Rafikov (2011) present a potential model that leads to a build up of sublimated gas at and just outside of the sublimation radius. If the initial mass of the dust disc is such that the timescales on which material is transported to the sublimation radius and sublimates exceed those on which it is transported viscously on to the star, then material builds up and spreads outwards from the sublimation radius. Many questions still remain concerning the formation of discs and their relation to the accretion on to the star.

1.4   Summary

In this chapter I have summarised the growing number of observations of planetary systems around evolved stars, along with the reasonably well understood population of planetary systems around main-sequence stars. There are important links to be made between main-sequence planetary systems and planetary systems around evolved stars. Given the dearth of planet detections around evolved stars, one of our biggest clues as to the evolution of planetary systems are the observations of metal polluted white dwarfs and white dwarfs with circumstellar discs. Our understanding of the link between these observations and planetary systems requires further development. The aim of this thesis is to improve our understanding of how planetary systems evolve after the main sequence and to investigate whether this evolution is consistent with the observations.

In this thesis I focus on the planetary system as a whole and consider typical

planetary systems that contain both planets and planetesimal belts, equivalent to the Solar System's asteroid or Kuiper belt. I start by summarising our knowledge of planetesimal belts or debris discs around main-sequence stars and describing models for their evolution in Chapter 2. I then make use of these models in Chapter 3, combined with stellar evolution, to determine the evolution of debris discs beyond the main sequence. This determines the population of evolved main-sequence debris discs around white dwarfs, which are very different to the observed close-in, dusty discs. In order to produce the observed close-in discs and metal pollution, material must be scattered inwards from an outer planetary system. In Chapter 4 I investigate whether the dynamical effects of stellar mass loss on a planet and debris disc, such as those observed on the main sequence, are sufficient to produce the observations. In order to form the observed discs, asteroids or comets must not merely be scattered inwards, they must be scattered on to star-grazing orbits, such that they approach close enough to the star to be tidally disrupted. In Chapter 5 I use analytical dynamics to investigate the planetary system architecture required to scatter particles on to star-grazing orbits. All of this work adds to our understanding of planetary systems beyond the main sequence and helps to show that there is a plausible link between main-sequence planetary systems and observations of metal polluted white dwarfs or white dwarfs with hot dust discs. This is summarised in Chapter 6.

Chapter 2

Debris disc theory

In this thesis I focus on planetary systems that contain not only planets, but belts of planetesimals, known as debris discs. There are many observations of debris discs around main-sequence stars and our understanding of them and their evolution on the main sequence is relatively good. This is a necessary precursor to understanding their evolution as the star evolves. This chapter summarises the important aspects of debris disc evolution. The first half discusses some aspects of planetary dynamics that are applicable to debris discs and specifically the work in the rest of this thesis, whilst the second half discusses models for debris disc emission.

2.1 Dynamics

The motion of planets and smaller bodies in a planetesimal belt or debris disc is controlled by gravity. To a first approximation, the motion of any planetary body is determined purely by the gravitational pull of the central star (unless the central star has a binary companion, see Haghighipour (2009) for a review of planetary dynamics in binary star systems which for simplicity are ignored here). In reality this only applies to very massive planets. The majority of planetary bodies will be perturbed by the gravitational forces of other planetary bodies in the system. Most planetary systems are hierarchical. Thus, the gravitational forces from smaller bodies, such as asteroids or comets, can be ignored in favour
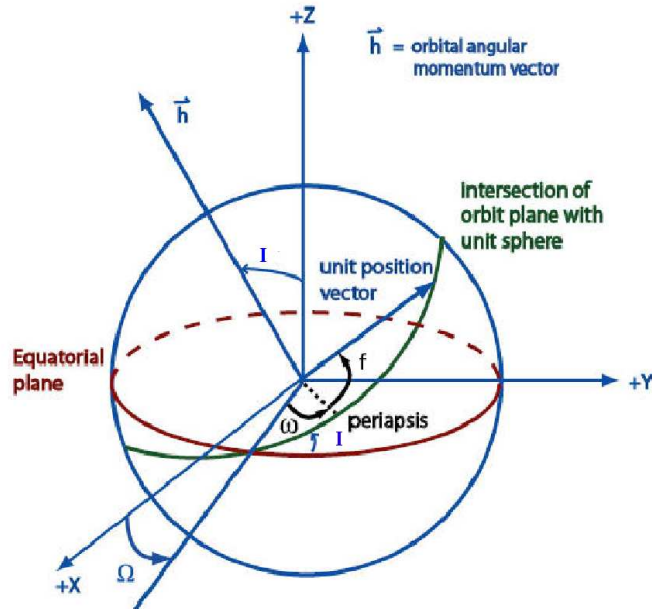
Figure 2.1 – The orbital elements of an ellipse, with respect to a reference plane is (x, y,z). ω is the argument of pericentre, θ is true longitude, Ω is the longitude of ascending nodes and i is the inclination. $\mathbf{h}$ is the angular momentum vector.

of the larger perturbations from planets. Planets can play an important role in determining the dynamics of small bodies and thus shape a debris disc.

First, considering the motion of any planetary body solely around the central star, the equations of motion for a particle, with position vector, $\mathbf{r}$, orbiting a central star of mass, M_*, are given by:

$$\frac{d^2\mathbf{r}}{dt^2} = \frac{-GM_*}{r^3}\mathbf{r} \tag{2.1}$$

If the particle is on a bound orbit, this forms an ellipse, described by:

$$r = \frac{a(1 - e^2)}{1 + e\ cos(\theta - \Omega - \omega)} \tag{2.2}$$

where a is the particle's semi-major axis, e its eccentricity, θ is true longitude, Ω is the longitude of ascending nodes and ω is the argument of pericentre. Fig. 2.1 shows the definition of these angles, and the orbit's inclination, I, in terms of the particle's orbit and a reference plane.

Although these equations are a good first approximation to the orbits of most

planetary bodies, most are perturbed by the gravitational influence of other massive planets in the system. Analytically the gravitational pull of other bodies can be considered as a small perturbation on the orbits in order to determine the dynamical behaviour. Many features can be described using an expansion of the *disturbing* function; see Murray and Dermott (1999) for further details. It is not possible in general to solve for the equations of motion for more than 2 massive bodies. The full equations for the N-body problem are given by:

$$m_i \ddot{\mathbf{r}}_\mathbf{i} = G \sum_{k \neq i} \frac{m_i m_k (\mathbf{r_k} - \mathbf{r_i})}{|\mathbf{r_k} - \mathbf{r_i}|^3} \qquad i = 1, N \qquad (2.3)$$

where m and $\mathbf{r}$ are the masses and position vectors for the N bodies, labelled by index i. $i = 1$ labels the central star of mass $m_1 = M_*$.

The only way to fully solve these equations is to integrate them numerically. There are a variety of standard techniques including Runge-Kutta, Burlisch-Stoer or sympletic integrator, see Morbidelli (2002) for a review of these techniques. In this work I make use of the code *Mercury* (Chambers, 1999) and the integrator RADAU (Everhart, 1985), that uses a 15th order Runge-Kutta with Gauss-Radau spacing, to integrate the equations of motion for any planetary system. *Mercury* also contains a sympletic integrator that is marginally faster, but not as accurate for close encounters. It is therefore generally used along with the Burlish-Stoer integrator for close approaches. All the different integrators produce results that are substantially the same.

Analytically there is a wealth of techniques and approximations that can be used to describe the motion of particle in the N-body problem. There is not space here to discuss them all fully, therefore I limit my discussion to that which is directly relevant to the rest of this thesis and refer the reader to Murray and Dermott (1999) for full descriptions and derivations.

2.1.1 Circular restricted three-body problem

One such analytical technique applies to debris discs, where it is a reasonable approximation to ignore any interactions between planetesimals, treating them as test particles, thus only considering the mass of the central star and any

perturbing planet(s). For a simple system with only one planet and a disc, the motion of particles in the disc can be described entirely by considering the form of the potential from a central body and the planet. In order to get a further handle on the problem analytically, it is useful to consider the case where the planet is on a circular orbit. This is known as the circular restricted three-body problem and is integrated numerically in Chapter 4.

Consider the case of two massive bodies of masses m_1 and m_2, and a mass-less test particle situated at a distance r_1 and r_2 from each body, respectively. If the planet and central star's orbits are restricted to be circular, then the two massive bodies orbit their common centre of mass at constant angular velocity n, and in the centre of mass frame the distance between the two bodies remains constant. Thus, in a frame rotating at constant angular velocity, n, the two bodies remain stationary. Consider this rotating frame, centred on the centre of mass, with the unit length defined as the separation of the two bodies and $G(m_1 + m_2) = 1$. Co-ordinates in this frame are given by (x, y, z). Therefore, the bodies are positioned at $(-\mu_2, 0, 0)$ and $(\mu_1, 0, 0)$, where $\mu_1 = Gm_1$ and $\mu_2 = Gm_2$ and the equations of motion of the circular restricted three-body problem can be written as:

$$\ddot{x} - 2n\dot{y} = \frac{\partial U}{\partial x} \tag{2.4}$$

$$\ddot{y} + 2n\dot{x} = \frac{\partial U}{\partial y} \tag{2.5}$$

$$\ddot{z} = \frac{\partial U}{\partial z} \tag{2.6}$$

where U is the pseudo-potential, given by:

$$U = \frac{n^2}{2}(x^2 + y^2) + \frac{\mu_1}{r_1} + \frac{\mu_2}{r_2}. \tag{2.7}$$

See Murray and Dermott (1999) pg.64 for a full derivation.

These equations can be used to determine a constant of motion of the circular restricted three body problem, the *Jacobi integral*, C_J. This is obtained by multiplying the three above equations by $\dot{x}$, $\dot{y}$, and $\dot{z}$ respectively, adding them

together and integrating to obtain:

$$C_J = n^2(x^2 + y^2) + 2\left(\frac{\mu_1}{r_1} + \frac{\mu_2}{r_2}\right) - \dot{x}^2 - \dot{y}^2 - \dot{z}^2. \tag{2.8}$$

This restricts the motion of a test particle to a region of parameter space, depending on its initial value of the Jacobi integral. For cometary bodies it is useful to consider the Tisserand parameter, which is derived from the Jacobi integral. This assumes that the mass of the planet is much less than the mass of the central star, *i.e.* $m_1 >> m_2$, and assumes $r_1 >> r_2$, so that it is not strictly valid when the test particle approaches very close to the planet, although it should be valid before and after the close encounter. The Tisserand parameter is conserved in the circular restricted three-body problem and is given by:

$$T_p = \frac{a_p}{a} + 2\sqrt{\frac{a(1 - e^2)}{a_p}} \cos I, \tag{2.9}$$

where a is the particle's semi-major axis, e its eccentricity, I its inclination and a_p the planet's semi-major axis. The Tisserand parameter is approximately conserved in the three-body problem. The conservation of this parameter will be used extensively in Chapter 5 in order to learn more about the dynamics in evolved planetary systems.

2.1.2   Resonance

An important feature of many planetary systems with multiple planetary bodies, is resonance. This occurs anytime there is a simple relationship between frequencies or periods associated with the planetary bodies. This could be orbital periods in the case of mean-motion resonances, spin-orbit periods, or precession periods in the case of secular resonances. Mean motion resonances are seen in many planetary systems, including our own Solar System, for example Neptune, who orbits the Sun three times for every two orbits of Pluto, shown in Fig. 2.2. This mean motion resonance protects the planets against close encounters and thus their mutual gravitational perturbations.

Mean motion resonances are often characterised in terms of the objects' mean

motions, n. If p and q are integers, two bodies in a mean motion resonance will satisfy

$$\frac{n'}{n} = \frac{p}{p+q}.$$ (2.10)

The resonance angle for such a particle is defined by:

$$\phi = (p+q)L' - pL - q\varpi',$$ (2.11)

where L' and L are the mean longitudes of both bodies and ϖ' the satellite's longitude of pericentre.

A particle is trapped in resonance if the resonant angle oscillates about some fixed value. The main mechanism for trapping particles into resonance is migration. The probabilities for particles to be trapped into resonance were calculated semi-analytically in Mustill and Wyatt (2011b). Many planetary bodies are trapped into resonance during the planet formation phase, when planets migrate (Chambers, 2009). Migration of small particles because of radiative forces can also trap them into resonance, for example the resonant clump trailing Earth in the zodiacal dust (Dermott et al., 1994). Stellar wind drag during the mass loss process can also trap small particles into resonances (Dong et al., 2010).

Resonant interactions can be self-correcting and lead to stable orbits, but they can also lead to chaotic behaviour, particularly where multiple resonances overlap. The gaps in the asteroid belt, such as the Kirkwood gap, are cleared by chaotic behaviour in resonances (Nesvorný et al., 2002). Kuiper belt objects may leave resonances with Neptune, once their eccentricity is excited sufficiently that they enter a chaotic region, where secular and mean motion resonances overlap (Morbidelli, 1997).

The overlap of many high order mean motion resonances close to a planet leads to a chaotic region close to the planet. The size of this region can be calculated by considering the width of mean motion resonances. This was done in Wisdom (1980) and defines a region close to the planet where orbits will be chaotic. This is given, in terms of the planet's semi-major axis, a_{pl}, by:

$$\frac{\delta a_{chaos}}{a_{pl}} = C \left(\frac{M_{pl}}{M_*} \right)^{2/7},$$ (2.12)
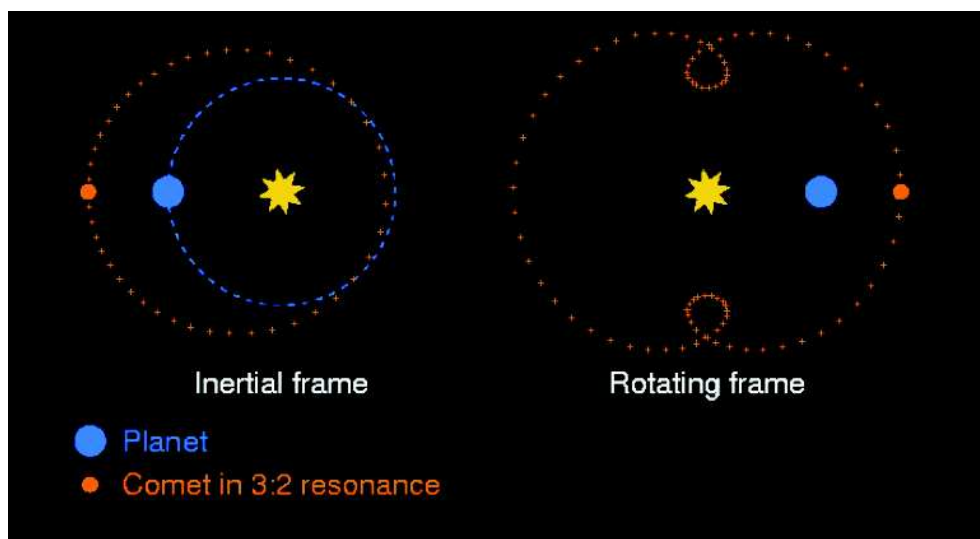
Figure 2.2 – The kinematics of the 3:2 resonance; for example that of Neptune and Pluto. In the rotating frame it is easy to see that the comet does not have close encounters with the planet. Figure made by Mark Wyatt.

where $C = 1.3$, and M_{pl}, M_* are the masses of the planet and star, respectively. This will be used in Chapter 4 to determine the region surrounding a planet that will be devoid of planetesimals, since any bodies orbiting within this region would be unstable on short timescales.

2.1.3   Mass Loss

The mass of the central star on the main sequence is constant, but on the first ascent or asymptotic giant branch the star loses mass. This has important consequences for the dynamics of orbiting planetary bodies. Even considering the simple 2-body problem, outlined in Eq. 2.1, a solution, Eq. 2.2, is only achieved if the central stellar mass M_* is a constant. The N-body problem is significantly more complicated. The equations of motion for a single planet around a star losing mass are determined analytically in Veras et al. (2011).

Fortunately stellar mass loss generally proceeds at a slow enough rate, compared to planetary orbits, that it is adiabatic. For isotropic mass loss it has been

shown that the specific angular momentum (h) is a constant of the motion:

$$h = \sqrt{G\mu a(1 - e^2)}, \qquad (2.13)$$

where $\mu = M_* + m$ is the total mass of the star and planetary body, a its semi-major axis, and e its eccentricity. Hadjidemetriou (1963) showed that this is true for binary star systems, by modelling the mass loss as an additional perturbing force that is a function of a time and mass dependent velocity. For a body on an initially circular orbit, its eccentricity remains constant (Veras et al., 2011), such that if angular momentum is conserved, then the evolution of the semi-major axis is given by:

$$a(t) = \frac{a(0)\mu(0)}{\mu(t)}. \qquad (2.14)$$

If the particle is on an initially eccentric orbit, the variation in the semi-major axis differs from this simple form, see Veras et al. (2011) for a full derivation of this and the variation of all orbital parameters.

It is possible to assess how good the adiabatic approximation is by considering the eccentricity induced on an orbiting body, initially on a circular orbit, if the mass lost by the star during a single orbit of that body, were to be lost instantaneously. The maximum super wind mass loss rates on the AGB are of order $\sim 10^{-4} M_\odot$ yr^{-1}, such that even orbits in the outer Kuiper belt, at ~ 50AU, with periods of ~ 350yr, only have their eccentricities increased by $e \sim \frac{\delta M}{M_*} \sim 0.03$, per orbit. This was calculated by assuming that the mass released in an orbital period was instead released instantaneously.

Only very large radii orbits, such as those of Oort cloud comets, may experience non-adiabatic mass loss (Veras et al., 2011). Even so, the majority of Oort cloud comets will not be significantly affected, since such high mass loss rates only act rarely and for short time periods. A small fraction of comets may be ejected during these episodes of high mass loss, but the majority only suffer small increases in eccentricity. For most planetary systems, including those considered in this work, the adiabatic approximation is a good approximation to the orbital evolution after stellar mass loss. I therefore assume that mass loss is adiabatic throughout the rest of this work.

Planetary systems may be destabilised by stellar mass loss. As the mass of the star decreases, since the planet masses remain unchanged, the gravitational influence of the planets on one another increases. This means that if planets were close to the stability limit they may become unstable (Debes and Sigurdsson, 2002). This can be seen analytically from the increase in the size of the planet's Hill's sphere. Chambers et al. (1996) determined that planetary orbits should be separated by at least $10R_H$ to guarantee stability, where R_H is the Hill's radius, given by:

$$R_H = a \left(\frac{m_{pl}}{3M_*} \right)^{1/3}, \tag{2.15}$$

m_{pl} is the mass of the planet and M_* is the stellar mass. The separation of two planets, in units of Hill's radii, with semi-major axes, a_2 and a_1 is given by:

$$N_{RH} = \frac{(a_2 - a_1)}{R_H(a_1)} = \frac{(a_2 - a_1)(3M_*)^{1/3}}{a_1 \, m_{pl}^{1/3}} \tag{2.16}$$

As the star loses mass, M_* decreases and a increases, such that the planet's separation in Hill's radii decreases, using Eq. 2.14:

$$N_{RH}(t) = \frac{(a_2(0) - a_1(0))(3M_*(t))^{1/3}}{a_1(0)m_{pl}^{1/3}} = N_{RH}(0) \left(\frac{M_*(t)}{M_*(0)} \right)^{1/3}, \tag{2.17}$$

where $a(0)$ and $M_*(0)$ are the original values and $M_*(t)$ those after stellar mass loss.

Thus, the separation of the planets in units of Hill's radii decreases, as their mutual perturbations increase and they can become unstable.

2.2 Debris disc modelling

In this section I discuss models for debris discs. Dynamics can be important for many debris discs, in particular in systems with planets, where resolved imaging shows evidence of interactions. Many models for the emission from debris discs ignore any dynamical perturbations, in favour of more detailed modelling of the

emission proprieties, collisions, radiative forces and stellar wind drag. This is appropriate for modelling the general population of debris discs, or individual systems that are not resolved. In this section I discuss the processes which are important for a debris disc and finish by briefly summarising some of the debris discs models that exist in the literature.

2.2.1 Thermal emission

Debris discs can be detected from the thermal emission of dust particles heated by the star. The dust particles are cooler than the star and hence this emission peaks at longer wavelengths, where the stellar flux is low. To a first approximation the emission can be modelled by a single temperature black body, although in many more sophisticated models this assumption is relaxed in favour of more realistic emission properties, such as those used in the models in Chapter 3.

Fig. 2.3 shows the emission from a single temperature black body, detected above the stellar photosphere in the infrared. The black body temperature can be related to the stellar luminosity, L_* and the disc radius, r, by (Wyatt, 2008):

$$T_{BB} = 278.3 \frac{(L_*/L_\odot)^{1/4}}{(r/AU)^{1/2}} \quad \text{K}. \tag{2.18}$$

The assumption of a single temperature black body is equivalent to assuming that the disc is at a single radius.

Debris discs contain a variety of grain sizes. As a first approximation it can be assumed that all grains act like black-bodies and have the same temperature. The flux from such a disc, at a given wavelength, is given by:

$$F_{disc} = \frac{B_\nu(\lambda, T)\sigma_{tot}}{4\pi d^2} \tag{2.19}$$

where $B_\nu(\lambda, T)$ is the Planck function or power per unit area per unit solid angle per unit frequency of a black-body at a temperature, T and wavelength, λ, σ_{tot} is the total cross-sectional area in dust and d is the distance to the source.

It is common to characterise debris discs in terms of their fractional luminosity,
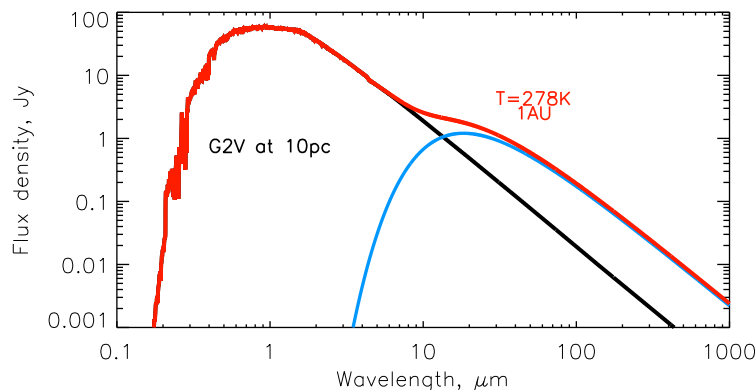
Figure 2.3 – The spectrum (red) from a G2 star (black), surrounded by a debris disc of radius 1AU. The emission from the debris disc, shown in blue, is modelled by a single temperature black-body.

or the ratio of their luminosity to the stellar luminosity:

$$f = \frac{L_{disc}}{L_*} = \frac{\sigma_{tot}}{4\pi r^2}, \tag{2.20}$$

where σ_{tot} is the total cross-sectional area of the disc and r is the disc radius.

Simple models for debris discs, in particular for those systems where there is only excess emission at two wavelengths, use a blackbody approximation to estimate properties of the disc, including importantly its radius. The black body approximation is only appropriate for particles that are significantly larger in size than the wavelengths of the emitted or absorbed radiation. The emission from most realistic debris discs therefore differs substantially from that calculated using a blackbody approximation. Many debris disc models include more realistic optical emission properties of grains that are size dependent. The emission properties of grains will also depend on their composition, porosity and shape. One of the most commonly used models for the emission properties of such grains is Li and Greenberg (1997), which is used in Chapter 3 to model the optical properties of small grains in a debris disc.

2.2.2 Collisions

Collisions between particles in a disc can have many outcomes. These are summarised nicely by the experiments of Blum (2010) and include sticking, bouncing and fragmentation, depending on the particles' collision velocity, masses, porosity and so forth. During the epoch of planet formation the presence of a gas disc damps the collisional velocities and collisions are generally sticking, accretional or bouncing. By the debris disc phase, the gas disc has been removed, the disc has potentially been gravitationally stirred by planets or large planetesimals (Kenyon and Bromley, 2004a; Mustill and Wyatt, 2009) and collisions are mainly destructive. If a debris disc has not been stirred, there will not be a collisional cascade and the disc will not be detected due to an absence of small dust.

The full impact of collisions on a disc is very complicated to model. This would require a way to determine the outcome of collisions and the distribution of collisional fragments, based on the impact velocities, particle sizes, compositions and strengths of the colliding bodies. It would need to include cratering and glancing as well as head-on collisions. The best models are always the simplest ones that are sufficient to explain the observations. For debris discs the most simple models only consider destructive collisions and assume that the overall outcome of many individual collisions maintains a constant size distribution of particles in the disc. This has been done in Wyatt and Dent (2002); Sheret et al. (2004); Wyatt et al. (2007b); Kains et al. (2011), amongst others.

The size distribution normally used is that of an infinite collisional cascade, in steady state, given by (Dohnanyi, 1969):

$$n(D)dD \propto D^{2-3q}dD, \tag{2.21}$$

where $n(D)dD$ is the number density of bodies with diameters between D and $D + dD$, and the index $q = 11/6$ (Tanaka et al., 1996). This assumes that collisions are self-similar, or that bodies of all sizes have the same strength per unit mass. More realistic models find different size distributions, based on more sophisticated prescriptions for collisions and the inclusion of a cut-off in the size distribution at small sizes, due to radiation pressure, see later discussion in §3.5.

This size distribution (or any other) can be used to determine both the mass

and cross-sectional area of a debris disc, if the range of particle sizes present is known. Assuming that there is a cut-off in the size distribution at D_{min} for small particles and D_{max} for large particles and $q = 11/6$, the total disc mass, M_{tot}, and the cross-sectional area, σ_{tot}, are given by

$$
\begin{align}
M(D)dD &\propto \rho D^{-1/2}dD \tag{2.22}\\
M_{tot} &\propto \rho(D_{max}^{1/2} - D_{min}^{1/2}), \tag{2.23}\\
\sigma(D)dD &\propto D^{-3/2}dD \tag{2.24}\\
\sigma_{tot} &\propto D_{max}^{-1/2} - D_{min}^{-1/2}. \tag{2.25}
\end{align}
$$

Hence if $D_{max} \gg D_{min}$,

$$
\sigma_{tot} = \frac{3M_{tot}}{2\rho\sqrt{D_{max}D_{min}}}, \tag{2.26}
$$

where ρ is the bulk density of the material. From these equations it can be seen that the majority of the disc's total cross-sectional area is found in the smallest particles of size D_{min}, whilst the majority of the disc's mass is found in the largest particles of size D_{max}.

In order to model the collisional evolution of particles in a debris disc a catastrophic collision is defined as one in which the largest remnant has a mass less than half that of the progenitor. This defines a dispersal threshold, Q_D^*, or the specific energy required by an impactor in order to catastrophically destroy a body of diameter D. Generally this is a function of particle diameter. Bodies fall into two regimes, large bodies where the outcome of collisions is dominated by gravitational forces and small bodies, where it is the internal strength of bodies that determines their collisional properties. SPH and analytical calculations can be used to determine the variation of Q_D^* as a function of particle diameter (*e.g.* Benz and Asphaug (1999); Kenyon and Bromley (2004c); Stewart and Leinhardt (2009)), however these produce a variety of values and are highly composition dependent. One example is shown in Fig. 2.4.

Whatever the prescription for the dispersal threshold, if only destructive collisions are considered, it is useful to consider the minimum size particles that can catastrophically break up an object of diameter, D, given by $D_{CC}(D)$. Since the
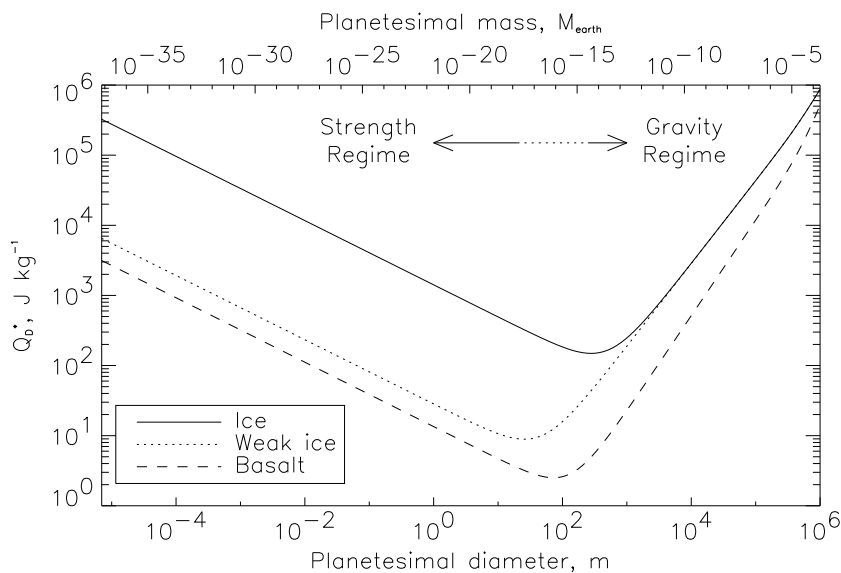
Figure 2.4 – The dispersal threshold, Q_D^*, as a function of particle diameter, based on SPH modelling of Benz and Asphaug (1999) for ice, weak ice and basalt.

cross-sectional area of the disc is dominated by small bodies, a given diameter particle will mainly be destroyed by objects of this minimum size, $D_{CC}(D)$. The rate at which a body of diameter D is catastrophically destroyed is given by:

$$R_{CC}(D) = \frac{f_{CC}(D)\sigma_{tot}v_{rel}}{V},$$ (2.27)

where v_{rel} is the relative velocity of the collision, V is the total volume of the disc and f_{CC} is the fraction of the total cross-sectional area density of planetesimals encountered by a body of diameter D that could catastrophically destroy that body.

One way of deriving a lifetime for particles against collisions is presented in Wyatt et al. (1999, 2007b). This assumes a simplistic disc geometry of radius r, width dr and constant opening angle, I, such that the disc volume is given by $4\pi r^2 dr I$. The relative velocity of particles is taken from a Rayleigh distribution and it is assumed that the particle eccentricity is the same order of magnitude as the inclination, $e \sim I$. In order to simplify the expressions it is useful and realistic to assume that objects can be destroyed by bodies significantly smaller than them, i.e. $D_{cc} \ll D$, although full expressions can be found in Wyatt et al.

(2007a). This gives a collisional lifetime for bodies of diameter, D, of:

$$t_c(D) = 1.31 \times 10^{-14} \frac{(\rho/kg\,m^{-3})\,(r/AU)^{13/3}\,(\frac{dr}{r})\,(Q_D^*/J\,kg^{-1})^{5/6}\,\sqrt{(D/m)\,(D_{max}/km)}}{(M_{tot}/M_\oplus)\,(M_*/M_\odot)^{4/3}\,e^{5/3}} \quad Myr,$$

(2.28)

where M_* is the mass of the star in solar units and ρ the density of each particle in the disc.

It can then be assumed that the total mass of the disc decreases collisionally on this timescale, such that:

$$\frac{dM_{tot}}{dt} = -\frac{M_{tot}}{t_c},$$

(2.29)

solving which to give the total mass in the disc at any time, t:

$$M_{tot}(t) = \frac{M_{tot}(0)}{1 + \frac{t}{t_c}},$$

(2.30)

where t_c is the initial collisional lifetime of the largest objects in the disc, of size D_{max}. One implication of this is that at late times $(t \gg t_c)$ there is a maximum mass for the disc that is independent of its initial mass, given by:

$$M_{max}(t) = 5.2 \times 10^{-13} \frac{(\rho/kgm^{-3})\,(r/AU)^{13/3}\,(\frac{dr}{r})(Q_D^*/Jkg^{-1})^{5/6}\,(D_{max}/km)}{(M_*/M_\odot)^{4/3})\,e^{5/3}\,(t/Myr)} \quad M_\oplus.$$

(2.31)

Since the disc mass is related to its cross-sectional area or fractional luminosity, this means that within the context of this model, for a given disc radius, stellar properties and age, t, a disc that is evolving collisionally in steady state cannot be brighter than f_{max}, where

$$f_{max} = 5.8 \times 10^{-10} \frac{(r/AU)^{7/3}\,\frac{dr}{r}(D_{max}/km)^{1/2}\,(Q_D^*/Jkg^{-1})^{5/6}}{(M_*/M_\odot)^{5/6}\,(L_*/L_\odot)^{1/2}\,(t/Myr)}.$$

(2.32)

There are multiple observations of debris discs that are brighter than this limiting brightness (Wyatt et al., 2007a). These are generally close-in, warm discs. The question arises as to how such discs formed, since they cannot be the leftovers of the planet formation process evolving collisionally in steady state.

They must either be the result of a recent collision between two large bodies (*i.e.* a transient event) or the material must originate from further out in the planetary system. Such systems will be discussed further in Chapter 5.

2.2.3 Removal of small grains

As noted in §2.2.2 the truncation of the collisional cascade at small sizes is important for the evolution and observable properties of debris discs. There are several forces that dominantly affect small grains and can cause them to be removed from a disc. These include radiative forces and stellar wind drag.

2.2.3.1 Radiative forces

The orbits of particles around a star are dominated by gravity, however the effect of the stellar radiation on small dust grains cannot be ignored. The radiative forces are given by (Mann et al., 2009):

$$\mathbf{F_{rad}} = F_{rad} \left[\left(1 - \frac{\mathbf{v.r}}{cr} \right) \frac{\mathbf{r}}{r} - \frac{\mathbf{v}}{c} \right],$$ (2.33)

where $\mathbf{v}$ and $\mathbf{r}$ are the particle velocity and position vectors and

$$F_{rad} = \frac{L_* \sigma Q_{pr}}{4\pi r^2 c}$$ (2.34)

where, Q_{pr} is the efficiency for radiation pressure transfer, σ is the cross-sectional area of the particle, $\sigma = \frac{3m}{2\rho D}$ for spherical particles of diameter D, mass m, and uniform density ρ. From this it can be seen that radiative forces are only important compared to gravitational forces if $\sigma = \frac{3m}{2\rho D}$ is large, *i.e.* for small diameter particles. Radiative forces result in two outcomes; the first, radial term, essentially reduces the gravitational force by a factor:

$$\beta_{rad} = \frac{F_{rad}}{F_{grav}} = \frac{L_* Q_{pr} \sigma}{4\pi G M_* mc}.$$ (2.35)

This generally affects small bodies formed in collisions. Assuming that the small bodies initially retain the position and velocity of their parents, who were on circular orbits, then all particles with $\beta_{rad} > 0.5$ are ejected, whilst particles with

lower values of β_{rad} end up on eccentric orbits. This is commonly used to define the smallest diameter particle that is found in a standard debris disc around a main-sequence star, the blow-out size, given by (Burns et al., 1979):

$$D_{\mathrm{bl}} = \frac{3 Q_{pr} L_*}{4\pi G M_* \rho},\tag{2.36}$$

where L_* and M_* are the stellar luminosity and mass and G the gravitational constant.

All particles smaller than D_{bl} will be on unbound orbits. Hence, D_{bl} is often used as the cut-off in the size distribution at small sizes, D_{min}. In a self-consistent calculation of the size distribution, this cut-off leads to a wavy size distribution (Campo Bagatin et al., 1994; Thébault et al., 2003; Krivov et al., 2006; Wyatt et al., 2011). The value of β_{rad} for a particle determines the eccentricity of its orbit. Particles on bound eccentric orbits, for example with $0.1 < \beta_{rad} < 0.5$, can produce an important contribution to the debris disc emission, often in a halo around the disc *e.g.* Vega (Müller et al., 2010).

The one unknown in these equations is the efficiency of the transfer of radiation to the particles. Generally $Q_{pr} = 1$ is a reasonable approximation, however, Q_{pr} depends on the particle diameter and composition. In the large diameter limit $(D \gg \lambda)$, $Q_{pr} \to 1$ and the radiation pressure efficiency merely depends on the geometrical cross-section of the particles, whereas for particles where $D \ll \lambda$, the radiation is in the Rayleigh limit and $Q_{pr} \propto D$. For $D \sim \lambda$, Q_{pr} is dependent on the shape and material of the particle. This behaviour can be seen in Fig. 2.5 which shows the variation of β_{rad} with particle diameter. This functional form for β_{rad} means that for some stars β_{rad} is never greater than 0.5 and no particles are ejected by radiative forces. The value of Q_{pr} is important, because the exact value of D_{bl} can significantly change the overall emission from the disc, since the emission is dominated by small particles.

2.2.3.2 Poynting-Robertson drag

The second term in Eq. 2.33 acts to reduce the angular momentum of an orbiting body, causing it to spiral inwards towards the star an effect known as Poynting-Robertson drag (PR-drag). By considering the radiative force as a small per-
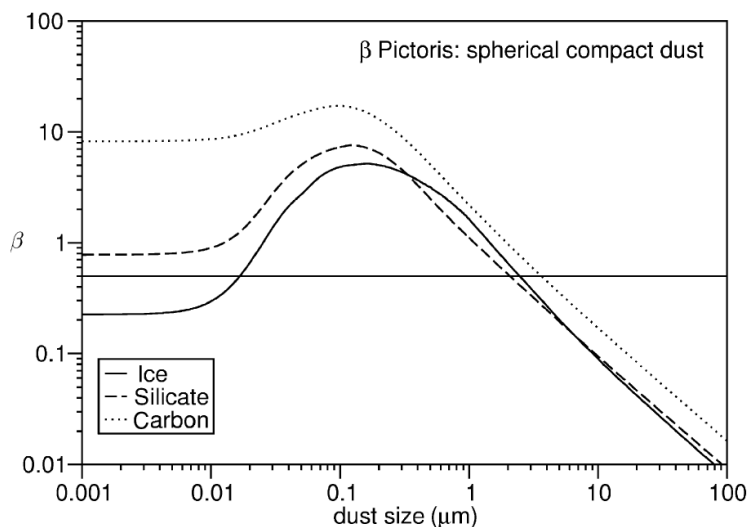
Figure 2.5 – The change in the radiation pressure efficiency as a function of particle diameter, for compact spherical dust grains, plotted in terms of β_{rad} (Mann et al., 2009).

turbation, it is possible to derive the rate of change of the orbital parameters it causes (see Burns et al. (1979) for a full derivation). Assuming circular orbits and averaging over the orbital period, this gives:

$$\langle \frac{da}{dt} \rangle = -\frac{3L^*}{8\pi\rho c^2 Da}$$ (2.37)

such that the semi-major axis of a particle changes by order itself, in time:

$$t_{\mathrm{pr}} = \frac{8\pi a^2 \rho c^2 D}{3L_* Q_{\mathrm{pr}}}.$$ (2.38)

Poynting-Robertson (PR) drag is mainly important for small bodies in close-in discs and can largely be ignored for the majority of detectable main-sequence debris discs. Particles in most detectable discs are destroyed by collisions on shorter timescales than PR-drag can act (Wyatt, 2005), which can be seen by comparing the PR-drag timescale (Eq. 3.17) to the collision lifetime (Eq. 2.28). There are, however, examples of debris discs where PR-drag is very important, our Solar system's zodiacal cloud being one example.

2.2.3.3 Stellar wind

main-sequence stars generally have weak stellar winds; the solar wind is on the order of $10^{-14}\,\mathrm{M_\odot\,yr^{-1}}$. Compared to the gravitational and radiative forces acting on particles in debris discs, the forces due to the stellar wind are weak and it is generally a valid approximation to ignore them. M stars, however, can have strong stellar winds, up to $10^{-12}\,\mathrm{M_\odot\,yr^{-1}}$ (Plavchan et al., 2005) and since radiative forces are weak in these stars, the forces due to the stellar wind are relatively important. There are models of such stars, such as AU Mic (Augereau and Beust, 2006), where the inclusion of stellar wind pressure is critical to truncate the collisional cascade. The stellar wind is also important for discs around stars on the giant branch, as will be discussed in Chapter 3.

The stellar wind behaves in a similar way to radiation pressure: it has a transverse and a radial component, that can cause bodies to become unbound or spiral inwards under stellar wind drag :

$$\mathbf{F_{sw}} = F_{SW}\left[\left(1 - \frac{\mathbf{v.r}}{v_{SW}r}\right)\frac{\mathbf{r}}{r} - \frac{\mathbf{v}}{v_{SW}}\right], \tag{2.39}$$

where v_{SW} is the velocity of the wind and

$$F_{SW} = \frac{\dot{M}_* v_{SW}\sigma Q_{SW}}{4\pi r^2}, \tag{2.40}$$

where Q_{SW} is the efficiency factor for momentum transfer from the stellar wind, and $\dot{M}_*$ is the rate of mass loss.

In a similar manner as for the above example of radiation pressure, particles become unbound if $\beta_{SW} > 0.5$, where, for spherical particles of uniform density, initially on circular orbits:

$$\beta_{SW} = \frac{\dot{M}_* v_{SW} Q_{SW}\sigma}{4\pi GM_* m}. \tag{2.41}$$

Conversely to radiative forces, where radiation pressure generally dominates over PR drag, stellar wind drag is generally more important than stellar wind pressure (β_{SW}). This is because β_{SW} is reduced by a factor $\frac{v_{SW}}{c}$ compared to β_{rad}. Stellar wind drag causes particles to spiral inwards towards the star on timescales

of:

$$t_{SW} = \frac{8\pi D\rho a^2}{3Q_{SW}\dot{M}_*}.$$ (2.42)

2.2.4 Planets

If there are planets in the system these can influence the debris disc. In fact signatures in the debris disc may provide vital clues to the presence of undetected planets (Quillen and Thorndike, 2002; Krivov, 2010; Churcher et al., 2010), *etc.* The main planetary perturbations considered in this thesis were discussed in §2.1. These include the truncation of the inner edge of a disc by a planet. The overlap of mean motion resonances clears a chaotic zone around the planet. This is seen in many observed systems, for example Neptune in the Solar System and Fomalhaut (Chiang et al., 2009). Resonant interactions between particles and planets can also be important. Many planetesimals may be trapped in resonance, for example during the planet migration phase. This leads to over-densities at specific locations and clumps in the resolved images of discs (Wyatt, 2003; Stark and Kuchner, 2008). Planets can secularly perturb planetesimals in the disc. This could lead to eccentric or inclined orbits. An eccentric disc has distinctive observational features, including brightness asymmetries and a pericenter glow (Wyatt et al., 1999; Moerchen et al., 2011). Discs with warps have also been detected *e.g.* Augereau et al. (2001). The potential effects of planets on debris discs are vast, however detailed modelling of individual systems is nearly always restricted by poorly constrained planetary orbits.

2.2.5 Models

All of these properties of a debris disc can be amalgamated to produce a full model for the emission from the disc. A review of such models can be found in Krivov (2010). Such models vary in sophistication from simple black body models of a single temperature, thin disc, to complicated models that are able to explain the behaviour of multiple grain populations seen in multi-wavelength resolved imaging. The emission from a disc can be calculated from a radial density distribution, size distribution and total disc mass. Although many models use the size distribution of an infinite collisional cascade (Eq. 2.21) as discussed

earlier, the size distribution may vary from this. Statistical code, such as ACE (Krivov et al., 2000, 2005) or Thébault et al. (2003); Thébault and Augereau (2007) calculate more realistic size distributions. These can include radiative forces, drag forces, disruptive and erosive collisions. Statistical calculations of the size distribution that include radiative forces can be well matched by analytical calculations (Wyatt et al., 2011). In order to model the dynamics of a disc or the effects of planets N-body simulations are required, such as Stark and Kuchner (2009). Some aspects of the dynamics, can however, be considered analytically, for example the formation of resonant clumps (Wyatt, 2003) and the secular perturbations of an eccentric planet on a disc (Wyatt et al., 1999).

2.3   Summary

Debris discs are belts of dust and rocks, containing bodies from micrometre sized dust particles up to kilometre sized boulders. In this chapter I have summarised the main factors that affect their evolution and emission properties, including collisions, dynamics, emission properties, radiative and drag forces. It is very difficult to produce a model that fully incorporates all of the relevant processes, therefore most debris disc models make a range of approximations in order to be able to provide usefully model the observations. In this thesis I make use of existing models for the evolution of debris discs, extending these to include the evolution of the star in Chapter 3 and focusing on the dynamical evolution of planetesimal belts and planets in Chapter 4 and Chapter 5.

Chapter 3

Post-main sequence evolution of A star debris discs

3.1   Summary

While the population of main-sequence debris discs is well constrained, little is known about debris discs around evolved stars. This chapter provides a theoretical framework that considers the effects of stellar evolution on debris discs, in particular the production and loss of dust within them. In this Chapter I repeat a steady state model fit to disc evolution statistics for main-sequence A stars, this time using realistic grain optical properties. I then evolve this population and consider its detectability at later epochs. My model predicts that debris discs around giant stars are harder to detect than on the main sequence because radiation pressure is more effective at removing small dust around higher luminosity stars. Just 12% of first ascent giants within 100pc are predicted to have discs detectable with Herschel at 160μm. However, this is subject to the uncertain effect of sublimation on the disc, which I, therefore, propose such observations can constrain. My model also finds that the rapid decline in stellar luminosity means that only very young white dwarfs have luminous discs. As such systems are on average at larger distances, they are hard to detect, but I predict that the stellar parameters most likely to yield a disc detection are a white dwarf at 200pc with a cooling age of 0.1Myr, in line with observations of the Helix Nebula.

My model does not predict close-in (<0.01AU) dust, as observed for some white dwarfs, however I find that stellar wind drag leaves significant mass ($\sim 10^{-2}$M$_\oplus$), in bodies up to $\sim$10m in diameter, inside the disc at the end of the AGB phase which may replenish these discs.

3.2 Introduction

Excess emission, over and above that expected from the stellar photosphere in the infra-red, is observed around hundreds of main-sequence stars, including 32% of main-sequence A stars (Su et al., 2006). This is inferred to be thermal emission from dust particles in orbit around the star in a debris disc. Debris discs are collisionally dominated in that the smallest bodies in the system are continuously replenished by collisions between larger objects and are subsequently removed by radiation pressure. The long term evolution of such systems can be modelled by steady state collisional models (Kenyon and Bromley, 2004b; Wyatt et al., 2007b; Krivov et al., 2008; Kennedy and Wyatt, 2010). Discs are depleted due to collisional erosion and are expected to show a slow decline in brightness. A decrease in brightness with age is indeed observed *i.e.* (Su et al., 2006) and can be well fitted with the models of Wyatt et al. (2007b), allowing such models to characterise the population of main-sequence A stars' debris discs reasonably accurately. These models assume that velocities in the disc are high enough that collisions are destructive. This requires that the disc is stirred, for example by self-stirring (*e.g.* Kenyon and Bromley (2004b)) or planet stirring (*e.g.* Mustill and Wyatt (2009).

As discussed in Chapter 1, dust is also seen around some post-main-sequence stars. In some cases this dust can be a result of the evolution of the star, for example material emitted in the stellar wind form spherical shells of dust that are observed around AGB stars (*e.g.* Olofsson et al. (2010)) or even stable discs observed around post-AGB stars, possibly linked to binarity (*e.g.* van Winckel et al. (2009)). Infrared excess observed around giant stars, *e.g.* Jura (1999), and the Helix Nebula (Su et al., 2007), on the other hand, has been interpreted as a disc similar to debris discs on the main sequence (although alternative interpretations do exist see *e.g.* Kim et al. (2001b)). Hot dust is also observed in

small radii (<0.01AU) discs around white dwarfs, *e.g.* Farihi et al. (2009) or von Hippel et al. (2007a), again inferred to originate from a debris disc. However, in contrast to main-sequence debris discs, these discs cannot be in steady state since material at such small radii has a short lifetime. Rather models suggest that these discs are formed when an asteroid approaches close to the star where it is tidally disrupted (Jura, 2008).

There are not yet enough observations of discs around post-main sequence stars to fully understand the population and it is not clear how the few discs that have been discovered around post-main sequence stars relate to the progenitor population of debris discs on the main sequence. In this chapter I take advantage of the fact that the main-sequence debris disc population around A stars is well characterised and extend the steady state collisional evolution models to consider the changes to this known population during the star's evolution. In particular I consider its detectability on the post-main sequence and therefore whether the observed post-main sequence discs derive from this population and what future observations would be best suited to detect them.

Previous work has looked at specific aspects of the effects of stellar evolution on asteroids or comets, such as stellar wind drag (Dong et al., 2010) and sublimation (Jura, 2004, 2008). Dong et al. (2010) model the evolution of a planetesimal belt due to stellar mass loss and suggest that the capture of km-sized planetesimals into mean motion resonance could explain systems such as the Helix Nebula. In this chapter a theoretical framework is built that incorporates the effect of collisions, radiation forces, the stellar wind, sublimation and realistic optical properties of dust, during the star's evolution from the main sequence to the white dwarf phase, focusing on the observable properties of the belt. The dynamical effects of stellar evolution, in particular stellar mass loss, on planetary systems will be considered in future work.

This chapter begins by discussing the evolution of the star in §3.3. This chapter uses the steady state collisional model for the evolution of debris discs on the main sequence, including the optical emission properties of realistic grains, fitted to the population of A stars observed with Spitzer at 24 and 70μm. Some of the details of this model were outlined in Chapter 2. Here, in §3.4, I take observations of debris discs around main-sequence A stars (Rieke et al., 2005; Su

et al., 2006) and reproduce the model fit calculated in Wyatt et al. (2007b), but this time using a model that incorporates the optical properties of realistic grains rather than a black body approximation. The steady state collisional models of Wyatt et al. (2007b) are then extended to include post-main sequence stellar evolution. In §3.5 the changes to the properties of an individual disc, as the star evolves, are described, whilst §3.6 discusses the implications for observations of the population of debris discs around evolved stars, focusing in particular on giant stars and white dwarfs and §3.7 summarises the models discussed.

3.3   Stellar Evolution

In this chapter stellar evolution models from Hurley et al. (2000) are used. Further details on the evolution of the star can be found in §1.2. The models in Hurley et al. (2000) use analytic formulae and are designed for population synthesis. They are accurate to within 5% of more detailed models. Although they provide a very accurate model for the evolution of the star during the slower phases of its evolution, for example the main sequence, they are less accurate for the very rapid phases of evolution, for example thermal pulses or super-wind phases on the asymptotic giant branch. This means that caution should be taken when applying the exact details of these models to observational properties of debris discs during the more rapid stages of stellar evolution, for example on the AGB. A good example being the diameter body removed by stellar wind drag, as will be discussed further in §3.5.4.4, which depends on the exact rate and time period for which mass loss acts. Fortunately it is not possible to observe debris discs on the AGB due to the presence of material ejected in the stellar wind and once the star becomes a white dwarf the disc quickly restablishes collisional equilibrium (at least for the smaller particles, see discussion in §3.5.4.6), such that the disc's future evolution is not significantly affected. These models are therefore sufficient to provide a good general description of the evolution of debris discs from the main sequence to white dwarf phase.

Here I consider stellar evolution models for stars of mass 1.67 to 3.8 $M_\odot$, these correspond to stars of spectral type A9-B8, according to the models of Kurucz (1979), although the stellar temperature varies along the main sequence and a
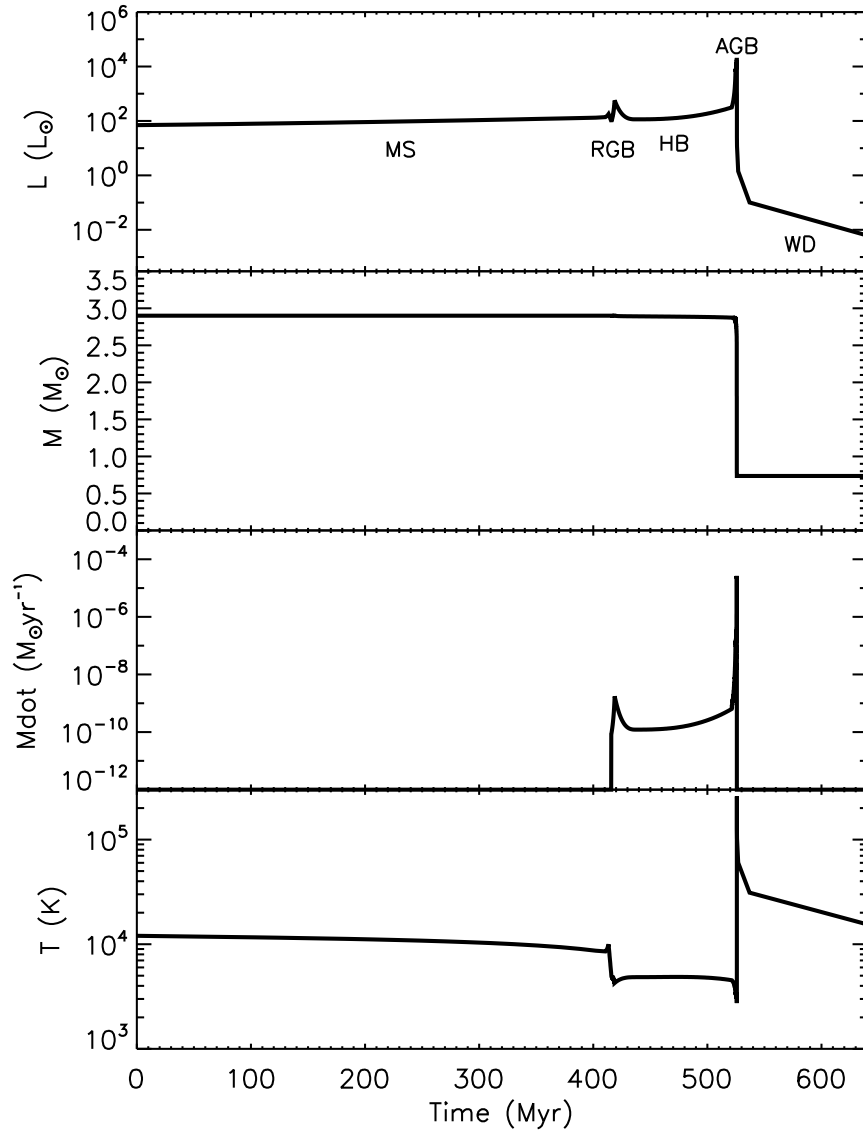
Figure 3.1 – The luminosity (L), mass (M), mass loss rate and temperature (T) evolution of a $2.9M_\odot$ star, Z=0.02, in solar values. MS: main sequence (0-413Myr), RGB: red giant (415.9-418.7 Myr), HB: core-helium Burning (418.7-521.4)Myr, AGB: asymptotic giant branch (521.4-525.9)Myr, WD: white dwarf (525.9 Myr onwards).

star of a given mass will be classified differently depending on the point in its evolution at which it is observed. This range of spectral types corresponds to that of the Su et al. (2006) sample.

There are two properties of the star that directly affect the disc's evolution and detectability; the stellar luminosity and mass. The variation in these is shown in Fig. 3.1, for the example of a 2.9M$_\odot$ star, equivalent to spectral type A0. The luminosity increases by approximately an order of magnitude on the giant branch and several orders of magnitude on the asymptotic giant branch. Typical values were summarised in Table 1.1. As the star exposes its core as a white dwarf, its luminosity drops swiftly by several orders of magnitude. The white dwarf then cools radiatively. This is modelled in Hurley et al. (2000) by Mestel theory (Mestel, 1952), with the white dwarf luminosity given by

$$L_{WD} = 635\ L_\odot\ \frac{(M_{WD}/M_\odot)\ Z^{0.4}}{[A\left((t/Myr) + 0.1\right)]^\alpha} \tag{3.1}$$

where M_{WD} is the mass of the white dwarf, Z is the metallicity, t is the cooling age or time since the WD formed, A is a parameter that is composition dependent and α is a parameter that describes the rate at which the white dwarf cools.

In the current models solar metallicity, Z=0.02 and A=15 for a CO white dwarf is used. Once the white dwarf has cooled significantly, crystallization occurs, and the cooling rate enters a different phase, and hence in these models α changes from 1.18 to 6.48 at an age of 9Gyr, for all spectral types. Although prescriptions for white dwarf crystallisation have improved significantly since the groundbreaking work of Mestel (1952), for example Metcalfe et al. (2004), crystallisation only occurs when the white dwarf cools to $\sim 6000 - 8000$ K (Metcalfe et al., 2004) and therefore Mestel (1952) should provide accurate luminosities for white dwarfs hotter than this. It is found later in this chapter that debris discs are only detectable around very young, hot white dwarfs (see §4.6) and therefore differences between the cooling theory of Mestel (1952) and more modern prescriptions are not significant for the current work.

Fig. 3.1 also shows the variation in stellar mass. Although stars lose mass on the giant branch, mass loss rates remain low until the super-wind phase towards the end of the asymptotic giant branch is reached. Therefore, as far as the

planetary system is concerned, the mass of the central star remains constant, throughout most of the star's evolution. Mass loss rates on the giant branch are, however, included. There is a fair degree of uncertainty in mass loss rates and the exact mechanism driving the mass loss in AGB stars (see review by Willson (2000)). Hurley et al. (2000) use the mass loss of Kudritzki and Reimers (1978) on the first and second ascent giant branches:

$$\dot{M}_R = 2 \times 10^{-13} \frac{(L_*/L_\odot)(R_*/R_\odot)}{(M_*/M_\odot)} \ \mathrm{M}_\odot \mathrm{yr}^{-1} \tag{3.2}$$

where M_*, R_* and L_* are the stellar mass, radius and luminosity in solar values.

On the AGB the formulation of Vassiliadis and Wood (1993) is used:

$$\log \dot{M}_{VW} = -11.4 + 0.0125 \left[(P/\mathrm{d}ays) - 100 \ \max((M_* - 2.5, 0.0)/M_\odot) \right] \ \mathrm{M}_\odot \mathrm{yr}^{-1} \tag{3.3}$$

$$P = \min \left(3.3, -2.07 - 0.9 \log(M_*/M_\odot) + 1.94 \log(R_*/R_\odot) \right) \quad \mathrm{days} \tag{3.4}$$

where P is the Mira pulsation period of the star, in days. The expansion velocity for the stellar wind is given by:

$$v_{SW} = -13.5 + 0.056(P/\mathrm{d}ays) \ \mathrm{kms}^{-1}. \tag{3.5}$$

The high mass loss rate during the super-wind phase, at the tip of the AGB (Vassiliadis and Wood, 1993), are given by

$$\dot{M} = 1.36 \times 10^{-9}(L_*/L_\odot) \ \mathrm{M}_\odot \mathrm{yr}^{-1}. \tag{3.6}$$

These are empirical mass loss rates, fitted to observations of RGB and AGB stars. Thermal pulses, with periods $\sim 10^5$yr dominate the evolution on the AGB as the star switches between helium and hydrogen shell burning. This may lead to discrete super-wind phases and the multiple shells seen in many planetary nebulae. Although the exact way in which mass is lost on the AGB may be important for the properties of the debris disc during this evolutionary phase, it is only the total mass that is lost that is important for the future evolution of the debris disc. As is discussed later in the chapter, it is very hard to observe

a debris disc around an AGB star and therefore the exact way in which mass is lost is not important for the evolution or detectability of a debris disc.

3.4 Models of debris discs around post-main sequence A stars

3.4.1 Evolution of an individual disc

The evolution of an individual disc, due to collisions, can be described by a simple steady state model such as that presented in Wyatt et al. (2007b). Many details of these models were described in §2.2.

A infinite collisional cascade is assumed for the size distribution (Eq. 2.21), but with a cut-off at small sizes determined by radiation pressure and the blow-out size ($D_{min} = D_{bl}$ Eq. 2.36) and at large sizes by $D_{max} = D_c$, the largest planetesimal formed.

For such a cascade the majority of the cross-sectional area of the disc is found in the smallest particles, but the mass of the disc is determined by the largest objects. As discussed in §2.2.2, these models assume that the evolution of the mass in the disc (M_{tot} in $M_\oplus$) is determined by the collisional lifetime (t_c) of the largest objects, with diameter, D_c, such that its evolution is described by Eq. 2.29 and Eq. 2.30.

For early times, when $t \ll t_c$, the mass in the disc remains approximately constant at its initial value, only turning over and falling off as $M_{\text{tot}} \propto \frac{1}{t}$ at times $t \gg t_c$. At late times the mass in the disc tends to a value M_{max} that is independent of its initial value (Eq. 2.31).

These models are, however, a simplification since only collisions between the largest bodies are considered to change the mass in the disc and a single value of the dispersal threshold, Q_D^*, is used. However this simple procedure allows the dust luminosity to be calculated to within an order of magnitude of more detailed prescriptions in which collisions between all diameter particles are considered, Q_D^* is a function of diameter and the size distribution is three-phase (Löhne et al., 2008).

In Wyatt et al. (2007b) the emission properties of the disc were calculated using a black body approximation. For reasons that are explained in §3.5.4.1, a black body approximation cannot be used in the current models. I updated the models of Wyatt et al. (2007b) to incorporate realistic emission properties of grains using the method of Wyatt and Dent (2002). The prescription of Li and Greenberg (1997) was used to calculate optical properties for grains with a composition of 1/3 silicates, 2/3 organic refractory materials and zero porosity, using Mie theory, Rayleigh-Gans theory or geometric optics in the appropriate limits. Although observations of debris disc suggest that grains may have a wide variety of composition, we chose this commonly used composition in order to provide a representative example and because it lacks icy material, so that the unknown effect of sublimation does not need to be accounted for (see discussion in §3.5.4.5. The temperature in the disc now depends on the particle's diameter, D, in addition to its distance from the star, r in AU:

$$T(D,r) = \left(\frac{\langle Q_{\mathrm{abs}} \rangle_{T_*}}{\langle Q_{\mathrm{abs}} \rangle_{T(D,r)}} \right)^{1/4} T_{BB} \qquad (3.7)$$

where $\langle Q_{\mathrm{abs}} \rangle_{T_*}$ and $\langle Q_{\mathrm{abs}} \rangle_{T(D,r)}$ are the particle's absorption efficiency averaged over the stellar spectrum and the spectrum of a black body radiating at temperature, T, and T_{BB} is the equilibrium temperature of the particle if it were a black body (Eq. 2.18). The flux from the disc, at a wavelength λ, is given by:

$$F_{\mathrm{disc}}(\lambda) = 2.98 \times 10^{-7} \frac{P(\lambda, r)(M_{\mathrm{tot}}/M_\oplus)}{\sqrt{(D_{\mathrm{min}}/\mu m)(D_c/km)}(\rho/kgm^{-3})\,(d/pc)^2} \quad \mathrm{Jy}, \qquad (3.8)$$

where M_{tot} is the mass in the disc in $M_\oplus$, $D_{\mathrm{min}}(\mu\mathrm{m})$ and D_c (km) are the smallest and largest particles in the disc, ρ is the density of each particle, in $\mathrm{kg\,m^{-3}}$, d is the distance from the observer to the star, in pc,

$$P(\lambda, r) = \int_{D_{\mathrm{min}}}^{D_c} Q_{\mathrm{abs}}(\lambda, D) B_\nu(\lambda, T(D,r)) \bar{\sigma}(D) dD, \qquad (3.9)$$

$B_\nu(\lambda, T(D,r))$ is the black body flux, in $\mathrm{JySr^{-1}}$ and $\bar{\sigma}(D)dD$ is the proportion

of the total cross-section of the disc found in particles with sizes between D and $D + dD$.

3.4.2 Population of discs around A stars

The population of debris discs around main-sequence A stars (spectral type B8 to A0) is relatively well constrained from observations by Spitzer at $24\mu m$ and $70\mu m$ (Rieke et al., 2005; Su et al., 2006). The models in Wyatt et al. (2007b) were fitted to these observations, using a population of 10,000 discs, with a distribution of initial masses, radii, spectral type, distance and ages. The initial masses formed a log normal distribution centered on M_{mid}, assuming the same width as for proto-planetary discs, 1.14dex (Andrews and Williams, 2005) and the initial radii a power law distribution, with the number of discs with radius between r and dr given by, $N(r)dr \propto r^{-\gamma}dr$, for discs between r_{min} and r_{max}. It was assumed that the stars are randomly distributed, evenly in spectral type and age and isotropically in distance. In the original model the dust grains were assumed to be black bodies and the $24\mu m$ and $70\mu m$ statistics were fitted by adjusting the parameters, M_{mid}, D_c, e, Q_D^*, γ, r_{min} and r_{max}. For simplicity it was assumed that the particle inclinations were of the same order as their eccentricities, $I \sim e$ and that the disc width is related to its radius by $dr = \frac{r}{2}$.

Here, I repeated the fit, using the updated formulation that incorporates the optical properties of realistic grains, to find new values for this parameter set. As discussed in Wyatt et al. (2007b) a degeneracy in the model means that these parameters are not uniquely constrained (see Eq.15 or Eq.16 of Wyatt et al. (2007b)). Thus, I chose to keep Q_D^* and e unchanged at $150\mathrm{Jkg}^{-1}$ and 0.05 respectively, without any loss of generality and performed a fit to M_{mid}, D_C, γ, r_{min} and r_{max}.

In order to fit the observations with a new population, calculated using the emission properties of realistic grains, in order to obtain the same overall behaviour, we assume that every disc should to evolve in the same way as every disc in the old population, calculated using a black body approximation. The optical properties of realistic grains mean that they are hotter and emit less efficiently at longer wavelengths. Therefore, in order for the flux ratio $\frac{F_{\mathrm{disc},24\mu m}}{F_{\mathrm{disc},70\mu m}}$

to remain the same, disc radii must increase. In fact a good fit is achieved by adjusting the disc radii from the values in the original model, r_{2470}, to a new value, $r_{\text{real}} = X_{2470}\, r_{2470}$. r_{real} is the radius of the disc calculated using realistic grains. A good fit to the data is achieved so long as the other parameters are also adjusted accordingly. Thus, I keep γ at -0.8, the value obtained from a fit to radii obtained assuming black bodies in Wyatt et al. (2007b). r_{min} and r_{max} increase by a factor X_{2470}. Then, in order to keep the flux from each disc constant, its fractional luminosity (f Eq. 2.20), the ratio of the luminosity of the disc to the luminosity of the star, should remain unaltered. Grains are larger than the peak emission wavelength of starlight on the main sequence such that they absorb starlight efficiently and $f \propto \frac{M_{tot}}{r^2 D_c^{1/2} D_{min}^{1/2}}$. Therefore M_{tot} and D_C need to be adjusted, keeping $\frac{M_{tot}}{\sqrt{D_c}r^2}$ constant. The maximum fractional luminosity that a disc of a given age can have due to its collisional evolution should also remain constant and thus using Eq. 2.31 $r^{7/3}D_c^{1/2}$ is also a constant. Together these mean that D_c and M_{mid} are altered by $(X_{2470})^{-14/3}$ and $(X_{2470})^{-1/3}$ respectively.

The conversion between r_{real} and r_{2470} was determined for realistic grains with the prescribed size distribution around main-sequence stars and is shown in Fig. 3.2. There is a functional dependence of X_{2470} on r_{2470} and spectral type that can be readily understood. For a given spectral type, X_{2470} has a minimum at intermediate radii but increases at small and large radii. The latter arises because the cooler temperatures at larger radii mean that the emission at these wavelengths is on the Wien side of the black body spectrum. This means that the small increase in the temperature of the grains causes a larger increase in the flux ratio at these wavelengths and hence the radius inferred, r_{2470}. This is compounded by the fact that the temperature of blow-out grains falls off more slowly with radius than that of black body grains (*e.g.* Su et al. (2009)). The increase at small radii arises because the emission efficiency of realistic grains falls off with wavelength, such that the emitted spectrum appears steeper (*i.e.* hotter) than the true grain temperatures. This effect is more important where the spectrum is steeper, *i.e.* where discs are hotter. All of these effects are more pronounced for later spectral type stars because the blow-out size is smaller (Eq. 2.36) and therefore there is a larger population of grains whose properties depart from black body.
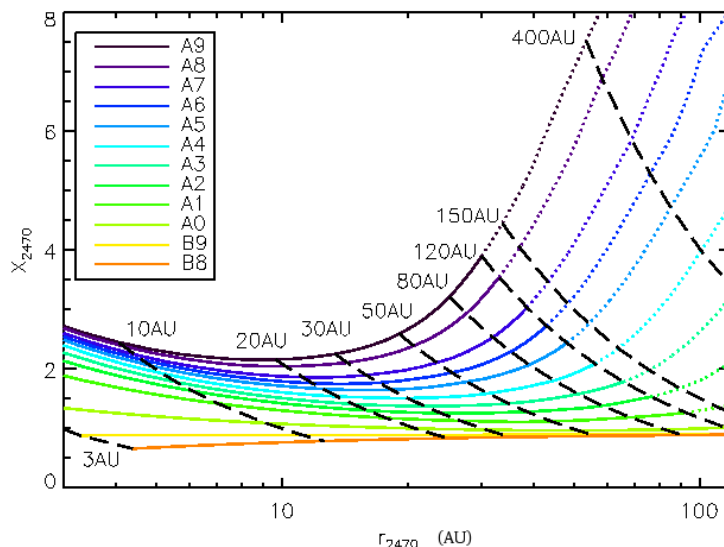
Figure 3.2 – The ratio (X_{2470}) of the radius of a disc calculated using realistic grains (r_{real}) to the radius inferred from the flux at 24μm and 70μm, assuming black body emission (r_{2470}), as a function of r_{2470}.

X_{2470} was found self-consistently using Fig. 3.2 to give an average value of 2.1. The above discussion suggests that an equally good fit to the statistics could be obtained with $M_{\text{mid}} = 8.1 M_{\oplus}$ and $D_c = 1.9$km. Indeed, as is shown in Fig. 3.3 this is found to be the case, with a total $\chi^2_{24,70,r}$ of 16.0 compared to 9.8 of Wyatt et al. (2007b).

3.5 Models of debris discs around post-main sequence A stars

The steady state models for the evolution of the disc due to collisions described in §3.4 are extended to include the effects of the evolution of the star, described in §3.3. The evolution of individual discs and changes to their properties, are discussed. Individual discs follow different evolutionary paths depending on their properties. The plots presented in this section are representative, and look at the evolution of a disc around a $2.9 M_{\odot}$ (equivalent to A0) star, with solar metallicity ($Z = 0.02$), initial masses in the disc of 1.0, 10.0 and 100.0 $M_{\oplus}$ and initial radii
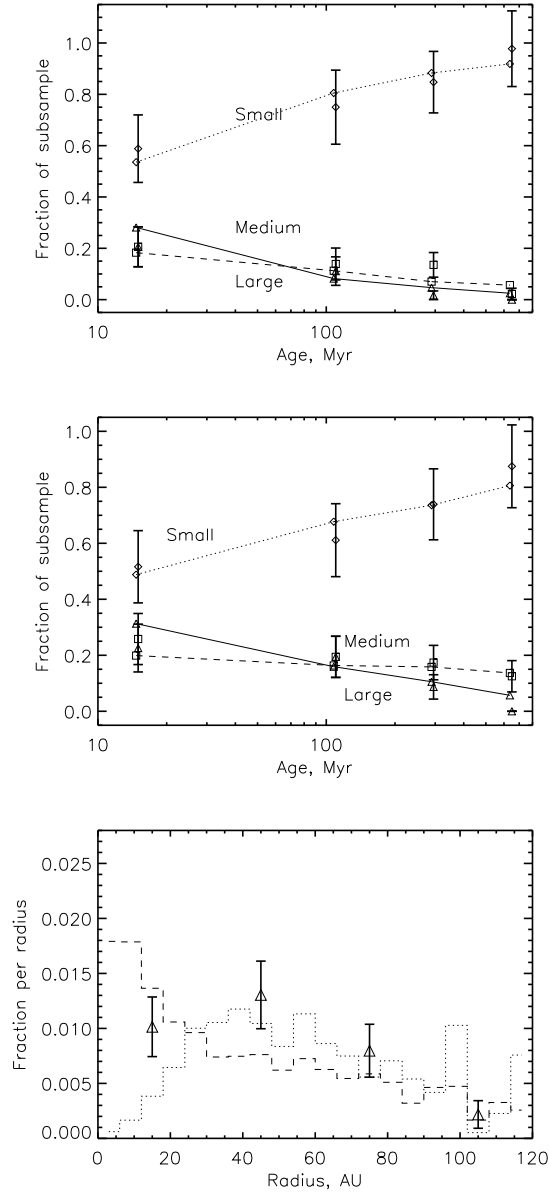
Figure 3.3 – Upper panels: The fit to the observations of Su et al. (2006) at 24 (top) and 70μm (middle), comparable to Fig.3 of Wyatt et al. (2007b). The plots show the fraction of stars with flux ratios in different age bins (<30Myr, 30-190Myr, 190-400Myr), at 24μm $\frac{F_{disc}}{F_*}$ = 1-1.25 (diamond: small excess), 1.25-2 (square: medium excess), >2 (triangle: large excess) and similarly at 70μm $\frac{F_{disc}}{F_*}$= 1-5 (diamond:small excess), 5-20 (square: medium excess), >20 (triangle: large excess). Observed values are shown with $\sqrt{N}$ error bars, whilst model values are joined with dotted, dash and solid lines, for small, medium and large excess.
Lower: The distribution of planetesimal belt radii. The model population is shown with a dashed line, whilst the sub-sample of the model population that is detectable at both 24 and 70μm is shown with a dotted line. The observed distribution of radii are shown with triangles and $\sqrt{N}$ error bars.

57

of 10, 50 and 100 AU, although the population models discussed in § 3.6.2 use the evolution for the appropriate disc and stellar parameters.

3.5.1 Radius evolution

As discussed in §2.1.3, as the star loses mass, the semi-major axes of orbiting bodies will increase. The star loses the majority of its mass in 10^5yr at the tip of the AGB. Mass loss is adiabatic and therefore disc radii increase by:

$$r(t) = \frac{r(0)M_*(0)}{M_*(t)} \tag{3.10}$$

Essentially the radius of the disc switches from an initial to a final value at the tip of the AGB, as shown in the upper panel of Fig. 3.4.

3.5.2 Mass in the disc and the collisional lifetime

As discussed in §3.4, the mass in the disc is dominated by the largest particles, and hence the timescale on which the mass is depleted is dependent on the collisional lifetime of the most massive particles, t_c (Eq. 2.28). The evolution of t_c is shown in the middle panel of Fig. 3.4. Collisions occur most frequently (t_c is shorter) in the most massive discs, closest to the star. The collisional lifetime increases significantly when the star loses mass, and is given by:

$$t_c = \frac{t_c(0)M_{tot}(0)M_*^{17/3}(0)}{M_*(t)^{17/3}M_{tot}(t)}. \tag{3.11}$$

Once the mass in the star changes as a function of time, the evolution of the mass in the disc is no longer given simply by Eq. 2.29, instead:

$$\frac{dM_{\text{tot}}}{dt} = \frac{-M_{\text{tot}}}{t_c} \propto \frac{M_{\text{tot}}^2(t)M_*^{4/3}(t)}{r^{13/3}(t)} \tag{3.12}$$

Using the expression for $r(t)$ (Eq. 3.10),

$$\int_{M_{tot}(t)}^{M_{tot}(0)} \frac{dM_{\text{tot}}}{M_{\text{tot}}^2} \propto \int_{M_*(t)}^{M_*(0)} M_*^{17/3}dt \tag{3.13}$$
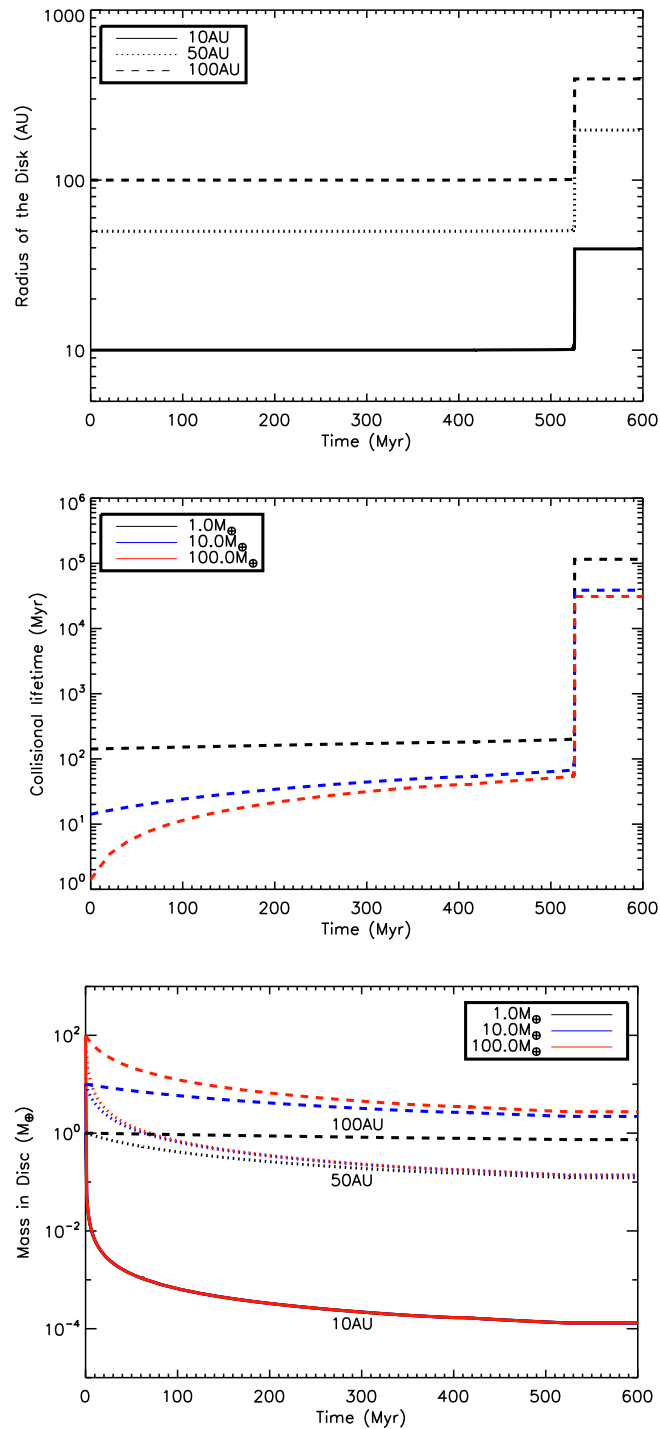
Figure 3.4 – The evolution of the disc radius (upper), collisional lifetime (middle) and total disc mass (lower), for different initial disc masses, $1.0 M_\oplus$ (black), $10.0 M_\oplus$ (blue), $100.0 M_\oplus$ (red), and radii, 100AU (dashed line), (bottom plot only 50AU (dotted line), 10AU (thick line)), around a $2.9 M_\odot$ star.

Therefore

$$M_{\text{tot}} = \frac{M_{\text{tot}}(0)}{1 + M_{\text{tot}}(0)K \int_{M_*(t)}^{M_*(0)} M_*^{17/3} dt} \tag{3.14}$$

where

$$K = [1.4 \times 10^{-9} (\frac{dr}{r}) \, e^{-5/3} \, (D_c/km) \, (Q_D/Jkg^{-1})^{*5/6} (r(0)/AU)^{13/3} (M_*(0)/M_\odot)^{13/3}]^{-1}. \tag{3.15}$$

However the mass in the star is approximately constant until the AGB, and up until this point Eq. 2.29 is valid. In fact up to the end of the AGB, the evolution of the mass in the disc is similar to that on the main sequence in that M_{tot} remains approximately constant for discs with longer collisional lifetimes (larger radii) and tends to M_{max} (Eq. 2.31) for discs with shorter collisional lifetimes (small radii), as shown in the bottom panel of Fig. 3.4. Once the star loses mass on the AGB, the collisional lifetime of larger objects increases so much that it approaches the Hubble time, even for close-in discs (see the middle panel of Fig. 3.4). Collisional evolution is no longer significant for the total disc mass, which remains constant throughout the white dwarf phase.

3.5.3   Temperature of the disc

Particles in the disc are heated by stellar radiation. Their temperature is a balance between absorption and emission and is a function of particle diameter, as shown in the upper panel of Fig. 3.5. Large grains emit efficiently and act like black bodies, whilst medium sized grains ($\sim \mu$m) emit inefficiently and are therefore hotter than black body. The smallest ($< \mu$m) grains emit and absorb inefficiently and reach a temperature that is independent of grain size.

To illustrate the evolution of the temperature of particles in the disc, the lower panel of Fig. 3.5 shows the change in the temperature of black body particles (appropriate for large grains) and the smallest grains in the disc of size D_{min} (as calculated in §3.5.4) as the star evolves. This follows the luminosity of the star. Along the main sequence the temperature of the disc is relatively constant, but it increases up to several hundred Kelvin (depending on disc radius) as the
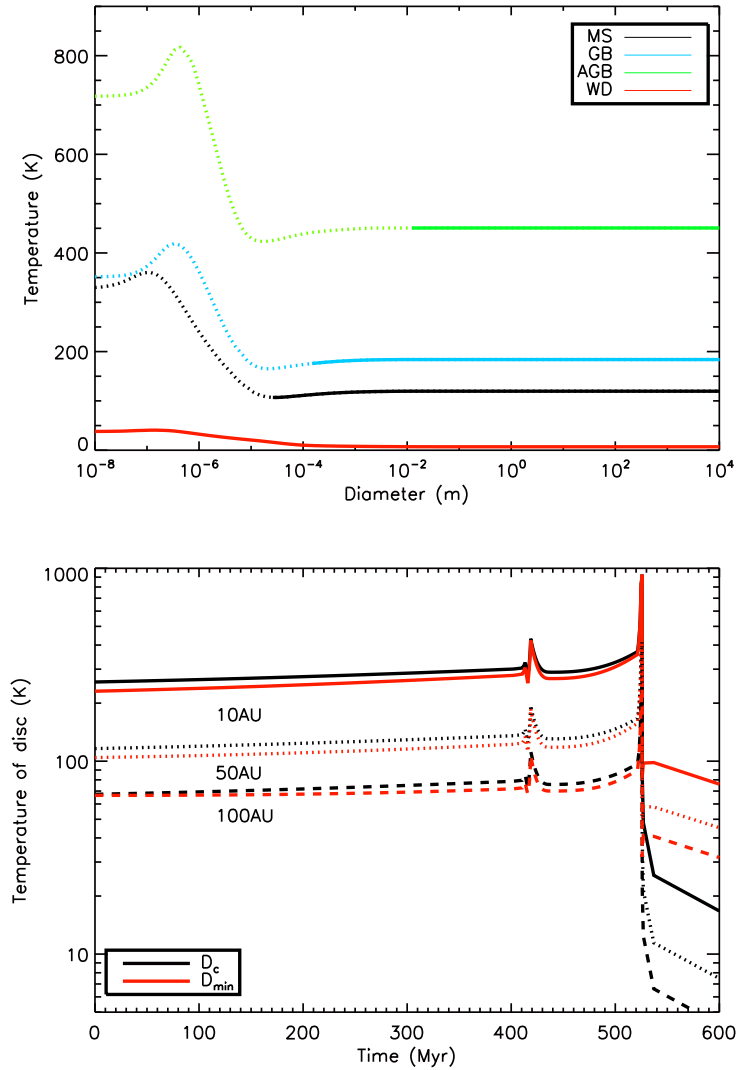
Figure 3.5 – Upper: The temperature of particles in the disc as a function of particle diameter, for a disc initially at 50AU around a $2.9M_\odot$ star, around a main-sequence star ($L_* = 190L_\odot$), giant star ($L_* = 500L_\odot$), an AGB star ($L_* = 1.5 \times 10^4 L_\odot$) or white dwarf ($L_* = 7 \times 10^{-3} L_\odot$). The solid lines show bound grains that are included in the model, whereas the dotted lines are unbound grains that are excluded from the model.
Lower: The evolution of the temperature of black body grains (D_c) and the smallest grains in the disc (D_{min}), for discs initially at 10AU (thick line), 50AU (dotted line), 100AU (dashed line) around a $2.9M_\odot$ star.

star's luminosity increases on the RGB and AGB. The temperature of the disc falls dramatically as the star becomes a white dwarf, mostly because the stellar luminosity drops by several orders of magnitude, but also because the discs are now further from the star. For this example mass star, the only epoch when the temperature of any particle in the disc greatly exceeds the black body temperature is for white dwarfs, however for later spectral type (lower mass) stars the smaller grains may be hotter than blackbody through all phases of stellar evolution.

3.5.4   Smallest particles in the disc

The size of the smallest particles (D_{min}) in the collisional cascade was determined in the Wyatt et al. (2007b) models and in §3.4 by radiation pressure (the blow-out size Eq. 2.36). This is correct for most discs around main-sequence stars, however there are several other forces that can remove small particles from the disc, including Poynting-Robertson drag, stellar wind pressure, stellar wind drag and sublimation. In the models presented here, D_{min} is determined by whichever of these processes removes the largest diameter objects at a given epoch. In the following section all five processes are discussed and compared such that D_{min} can be determined for every disc during its evolution. The outcome is summarised in Fig. 3.6.

3.5.4.1   Radiation pressure

As discussed in Section 2.2.3.1, radiation pressure is a radial force which acts in the opposite direction to the star's gravity. The ratio of radiation forces to the gravitational forces is β_{RAD} (Eq. 2.35). The dependence of β_{rad} on particle diameter is shown in the left panel of Fig. 3.7, for realistic grains, calculated in the same manner as described in §3.6.2, at different epochs in the star's evolution. The peak in β_{rad} occurs at a size comparable to the peak wavelength in the stellar spectrum. The dotted line shows the approximation to β_{rad} used in this chapter for which $\langle Q_{\mathrm{pr}} \rangle = 1$. It only deviates from the more realistic calculation at the smallest particle sizes and since these small particles are generally removed from the disc, apart from during the white dwarf phase, this is considered a reasonable approximation.
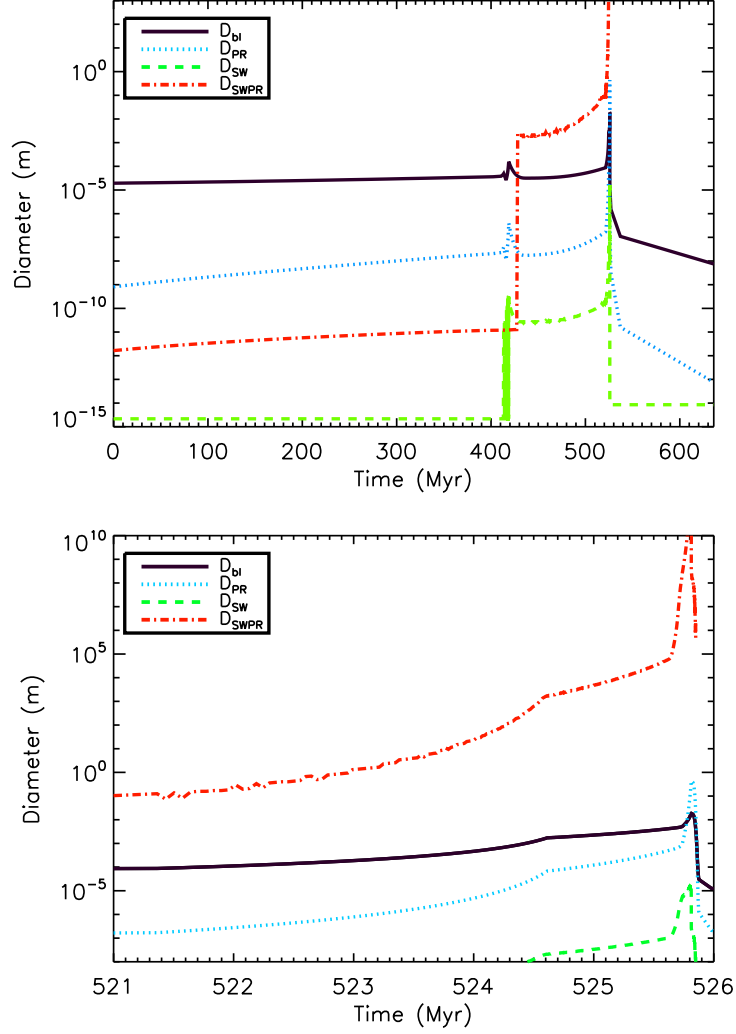
Figure 3.6 – The limiting diameter below which objects are removed by either radiation pressure (D_{bl}), PR-drag (D_{PR}), stellar wind pressure (D_{SW}) or stellar wind drag (D_{SWPR}), calculated using Eq. 2.36, Eq. 3.18, Eq. 3.21 and Eq. 3.23, in a disc initially at 100AU with a mass of $10M_{\oplus}$, around an evolving $2.9M_{\odot}$ star. The lower panel shows a zoom-in on the AGB. D_{SWPR} overestimates the diameter bodies that are removed by stellar wind drag as it does not take into account the finite AGB lifetime.

The upper left panel in Fig. 3.7 shows how the blow-out size (D_{bl}) changes as the star evolves for stars with different initial masses. The blow-out size follows the luminosity evolution of the star, increasing both on the RGB and AGB, up to ∼cm in size, before decreasing significantly as the star becomes a white dwarf. The stellar luminosity of a white dwarf is so low that once the star has cooled sufficiently ($L_{WD} \leq 0.1L_{\odot}$), β_{rad} is never above 0.5 (as seen in Fig. 3.7) and no grains are removed from the system by radiation pressure. The change in stellar luminosity or β_{rad} with time causes particles to spiral inwards, changing their semi-major axis by:

$$a(t) = \frac{a(0)(1 - \beta_{rad}(0))}{(1 - \beta_{rad}(t))}, \tag{3.16}$$

where a(0) and $\beta_{rad}(0)$ are the semi-major axis and ratio of the radiation pressure to the stellar gravity at the start of the white dwarf phase. No particles ever reach the star by this process, the maximum fractional change in semi-major axis is $(1 - \beta_{rad}(0))$.

This leaves the question of what, if anything, removes the smallest particles from collisional cascades in discs around white dwarfs, a problem which also exists for M-dwarfs (Plavchan et al., 2009). It is possible that magnetic effects or interactions with the interstellar medium remove the smallest particles in discs around white dwarfs. In this chapter, however, the fate of the smallest particles is left as an open question. The bottom panel of Fig. 3.7 shows that, should they exist, particles smaller than $D_{min} = 10^{-8}$m contribute negligibly to the total flux in the wavebands considered here. This is because, despite the size distribution of Eq. 2.21 meaning that such grains contain the majority of the cross-sectional area in the disc, such small grains also have extremely low emission efficiencies at longer wavelengths. For example even for the extreme case of a disc at 100AU, around an evolved $2.9M_{\odot}$, with a white dwarf cooling age of 1Myr and a size distribution that extends down to 10^{-10}m, the contribution of particles less than 10^{-8}m in size to the 24μm disc flux is only 20%. Thus for practical purposes I set $D_{min} = 10^{-8}$m.
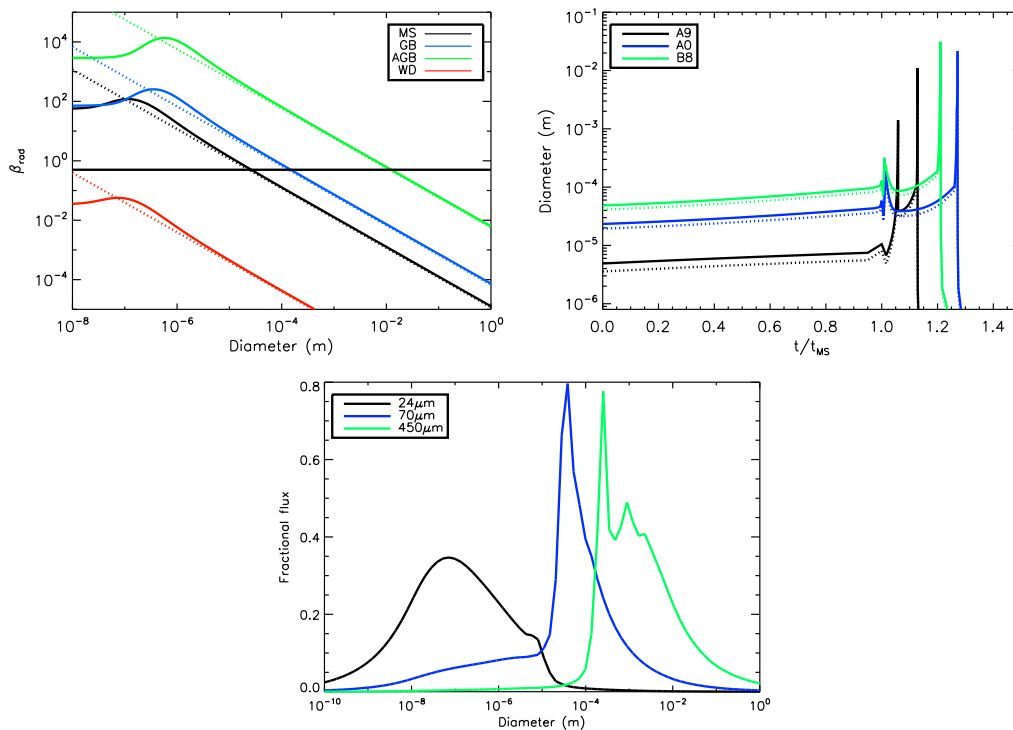
Figure 3.7 –   The effect of radiation pressure on the disc. Calculations with $\langle Q_{\rm pr} \rangle = 1$ are shown with dotted lines, whilst the solid lines show a more realistic calculation.
Upper left: The ratio of the radiational to gravitational forces (β_{rad}) for different diameter particles in a disc around a main-sequence star ($L_* = 190 L_\odot$), giant star ($L_* = 500 L_\odot$), AGB star ($L_* = 1.5 \times 10^4 L_\odot$) or white dwarf ($L_* = 7 \times 10^{-3} L_\odot$). The horizontal black line shows $\beta_{rad} = 0.5$. Particles with $\beta_{rad} > 0.5$ are removed from the system by radiation pressure. The maximum value of β_{rad} is less than 0.5 around a white dwarf, once L_{WD} falls below $\sim 0.15 L_\odot$.
Upper right: The change in the blow-out diameter of realistic grains around 1.67, 2.9 and 3.8 $M_\odot$ or A9, A0 and B8 stars. For both plots the dotted lines show calculations with $\langle Q_{\rm pr} \rangle = 1$, which do not vary significantly from the solid lines, which include a more realistic calculation of $\langle Q_{\rm pr} \rangle$, apart from for small diameter particles.
Lower: The fraction of the flux per unit log diameter, defined such that the area under the curve is 1, for a disc at 100AU, around an evolved 2.9$M_\odot$ star as a white dwarf with a cooling age of 1Myr.

3.5.4.2 Poynting-Robertson Drag

Radiation forces also oppose the velocity of an orbiting dust particle, reducing its angular momentum and causing it to spiral inwards, by Poynting-Robertson drag (PR-drag), changing its radius by order itself on timescales of

$$t_{\mathrm{pr}} = 1.4 \times 10^{-6} \frac{(r/AU)^2 (\rho/kgm^{-3})(D/m)}{L_* \langle Q_{\mathrm{pr}} \rangle} \quad \mathrm{Myr.} \tag{3.17}$$

Poynting-Robertson drag is only relevant for particle sizes for which the PR-drag timescale is significantly shorter than the collisional lifetime, since otherwise the particles are destroyed by collisions before they have had the opportunity to migrate. Assuming that the size distribution extends down in size indefinitely according to Eq. 2.21 and that PR-drag lifetime varies according to Eq. 3.17, both of which are valid in the regime where radiation pressure is negligible, it is possible to derive a condition for the diameter, D_{PR}, at which the collisional cascade is truncated by PR-drag, by comparing the collisional lifetime of the smallest grains to their PR-drag lifetime:

$$D_{PR} = 8.63 \times 10^{-23} \frac{(L_*/L_\odot)^2 \left(\frac{dr}{r}\right)^2 (r/AU)^{7/3} Q_D^{*5/3} (D_c/km)}{(M_*/M_\odot)^{8/3}(M_{tot}/M_\oplus)^2 e^{10/3}} \quad \mu m. \tag{3.18}$$

In Fig. 3.6 D_{PR} is compared to D_{bl} (Eq. 2.36). D_{PR} is always smaller than D_{bl} for the disc initially at 100AU with $10 M_\oplus$ shown, such that collisions and radiation pressure dominate over PR-drag which can therefore be ignored, as was previously shown in Wyatt (2005). A similar analysis for discs of different mass and radii around different mass stars shows that PR-drag can always be ignored except for close-in discs or those low in mass.

PR-drag in discs around white dwarfs is of particular interest as a possible mechanism to remove the smallest grains. Of potential importance is the fact that objects larger than $D > \frac{22.4 \, mm}{(r(0)/AU)^2}$ can never reach the star due to PR-drag. This is because the luminosity of the white dwarf decreases, and thus the rate at which objects spiral in decreases with time. The critical size is calculated by solving for the rate of change of semi-major axis, a, due to PR-drag, for a zero

eccentricity particle, given by (Burns et al., 1979):

$$\langle\frac{da}{dt}\rangle = -\frac{3L_{WD}}{8\pi\rho c^2 Da}$$

(3.19)

where L_{WD} is given by Eq. 3.1. However since collisions still occur on faster timescales than PR-drag can act, even for the smallest particles present (10^{-8}m, as is seen in the upper panel of Fig. 3.6), it is not expected that PR-drag has a significant effect on debris discs around white dwarfs.

3.5.4.3 Stellar wind pressure

Mass loss is an important feature of stellar evolution along the giant, horizontal and asymptotic giant branches. However mass loss rates are low and do not affect the disc significantly except towards the end of the AGB. It should be noted that there is a relatively large degree of uncertainty in the exact mass loss rates of an evolving star, as discussed in §3.3. As discussed in §2.2.3.3, the effect of the stellar wind on particles in the disc is very similar to that of stellar radiation in that its pressure component causes the smallest particles created in collisions to have eccentric or unbound orbits and its drag component causes them to spiral inwards. Assuming a stationary wind model, with a constant wind velocity v_{SW}, the ratio of the pressure force due to the stellar wind to the gravitational forces is given by:

$$\beta_{SW} = 5.67 \times 10^{10}\frac{(\dot{M}_*/M_\odot yr^{-1})(v_{SW}/kms^{-1})Q_{SW}}{(M_*/M_\odot)\ (\rho/kgm^{-3})(D/m)},$$

(3.20)

where $\langle Q_{SW}\rangle$ is the efficiency for momentum transfer from the stellar wind, assumed to be 1, $\dot{M}_*$ the mass loss rate, in $M_\odot$ yr^{-1} and v_{SW} the wind velocity, in kms^{-1}, calculated in Eq. 3.5.

Just like with radiation pressure grains smaller than D_{SW} or with $\beta_{SW} > 0.5$ would be removed from the system, where

$$D_{SW} = 1.13 \times 10^{-4}\frac{(\dot{M}_*/M_\odot yr^{-1})(v_{SW}/kms^{-1})}{(\rho/kgm^{-3})(M_*/M_\odot)}\quad \text{m.}$$

(3.21)
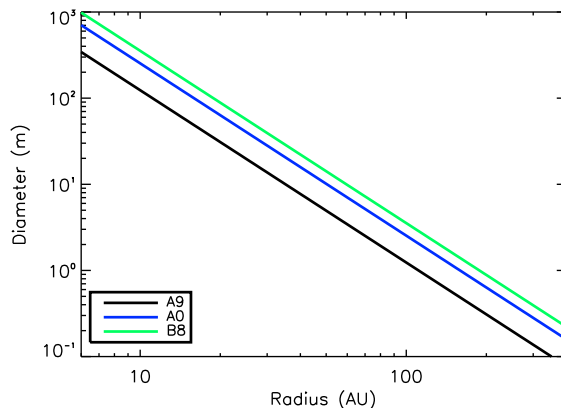
Figure 3.8 – The maximum diameter object that can be removed by stellar wind drag, throughout the disc's evolution, ignoring collisions, as a function of disc radius, for a disc around a $1.67 M_\odot$ (A9), $2.9 M_\odot$ (A0) or $3.8 M_\odot$ (B8) star.

However, as shown in Fig. 3.6 D_{SW} is smaller than D_{bl} throughout the star's evolution, such that removal of grains by stellar wind pressure can be ignored.

3.5.4.4 Stellar wind drag

The stellar wind causes particles of diameter, D, in μm, to spiral in towards the star on timescales of:

$$t_{SW} = 9.4 \times 10^{-17} \frac{(D/m)(\rho/kgm^{-3})(r/\text{AU})^2}{Q_{SW}(\dot{M}_*/M_\odot yr^{-1})} \quad \text{Myr.} \quad (3.22)$$

Similarly to for PR-drag these timescales can be compared to those for collisions (Eq. 2.28) to derive a condition for the diameter below which particles are removed by stellar wind drag:

$$D_{SWPR} = 194 \frac{(\dot{M}_*/M_\odot yr^{-1})^2 (r/AU)^{14/3} \frac{dr}{r}^2 (Q_D^*/J\,kg^{-1})^{5/3}(D_c/km)}{(M_{tot}/M_\oplus)^2 (M_*/M_\odot)^{8/3} e^{10/3}} \quad \text{m.} \quad (3.23)$$

In Fig. 3.6 D_{SWPR} is compared to D_{bl}, D_{SW} and D_{PR} throughout the star's evolution. It shows that stellar wind drag is only important for the higher mass loss rates on the horizontal and asymptotic giant branches, seen in Fig. 3.1. This is generally true for all disc and star parameters considered in this study.

The high mass loss rates, however, only act for a relatively short timescale, shorter than collisional timescales, such that D_{SWPR} actually overestimates the size objects that are removed by stellar wind drag. Fig. 3.8 shows the maximum diameter particle that can be removed by stellar wind drag for a disc around a $2.9M_\odot$ star, given the finite AGB lifetime. For the smallest radii discs, since planetesimals up to D_C (1.9km) are present in my model, almost all the mass in the disc is removed by stellar wind drag during the AGB phase. However the maximum diameter particle that can be removed for large radii discs is not much larger than the blow-out size. It should also be noted, as discussed earlier, that the exact values calculated in these models depend on the exact rates and time period for stellar mass loss. Therefore, their accuracy is limited by the accuracy of the stellar evolution code.

Although the majority of the disc mass at the end of the AGB still lies within the main belt, my treatment of the effects of stellar mass loss do not include the fate of smaller bodies migrating inwards under stellar wind drag. This is the main difference between my work and numerical simulations such as Dong et al. (2010). Dong et al. (2010) also include the effect of planets on a planetesimal belt, including the trapping of planetesimals into mean motion resonances. Although my models do not include the flux from small bodies spiralling in under stellar wind drag in the calculation of the disc luminosities, the amount of material distributed between the inner edge of the belt and the star has been monitored. This will be discussed further in §4.6, in terms of the hot white dwarf discs observed around some stars, for example Farihi et al. (2009).

3.5.4.5   Sublimation

As the star evolves to higher luminosities particles heat up and may sublimate. For some ideal assumptions, the resulting rate of change of diameter, D (in m), is independent of the size (Jura, 2008):

$$\frac{dD}{dt} = \frac{2\dot{\sigma}_0}{\rho}\sqrt{\frac{T_0}{T(t)}}e^{\frac{-T_0}{T(t)}} \qquad (3.24)$$
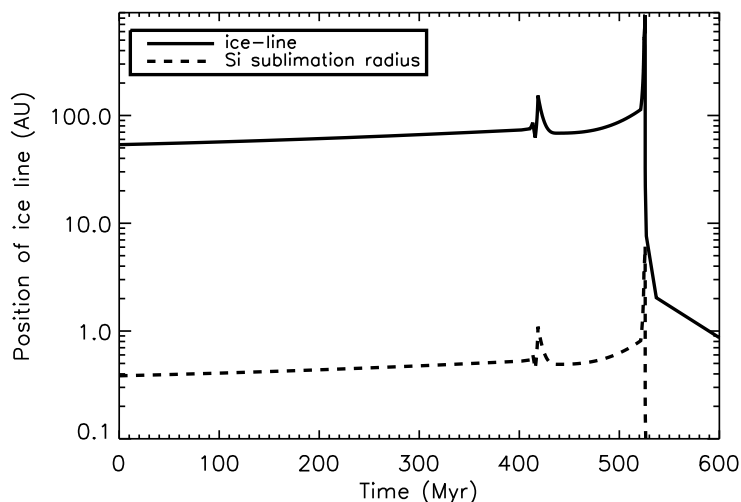
Figure 3.9 – The change in position of the ice-line and silicate sublimation radius due to the change in luminosity of a $2.9M_\odot$ star, Z=0.02, as it evolves. Objects initially outside the ice-line on the main sequence, *e.g.* at 100AU, could end up inside of the ice-line around a giant or AGB star, such that any particles composed purely of water ice would sublimate.

where T the temperature, in K, $\dot{\sigma}_0 = 1.5 \times 10^{10} \mathrm{kgm^{-2}s^{-1}}$ and T_0 the composition dependent sublimation temperature. For pure water ice $T_0 = 5,530$ K and for olivine $T_0 = 65,300$K, meaning that water ices sublimate at ~ 110K, whereas silicates only sublimate at $\sim 1,300$K. Here I define the ice-line and silicate sublimation radius as the radius inside of which black bodies have temperatures hotter than these sublimation temperatures.

The change in the position of the ice-line and silicate sublimation radius as the star's luminosity changes is shown in Fig. 3.9. It can be seen that the silicate sublimation radius is always smaller than the discs considered in the current models, hence the sublimation of silicates can be ignored for the population of discs considered.

Temperatures hot enough for the sublimation of water ices, on the other hand, are found in debris discs around main-sequence stars, for example sublimation of water ice is important for comets in our Solar System on orbits that approach the Sun within the ice line of 6 AU. A disc initially outside of the ice-line on the main sequence, may be inside of it by either the giant or asymptotic giant branches.

The sublimation of objects composed entirely of water ice would therefore be expected, resulting in significant mass loss from objects of all sizes in the disc. Since sublimation loss timescales are proportional to diameter, this means that smaller objects are removed most rapidly. This could truncate the collisional cascade size distribution at a size larger than the blow-out limit.

The behaviour of more realistic objects of mixed composition, however, is more complex. Sublimation may not proceed at the rate given by Eq. 3.24 indefinitely as water ice below the surface may be protected from sublimation by the surrounding layers of other non-volatile material (Jura and Xu, 2010). As observed for Solar System comets, sublimation may also lead to the release of small dust grains that were originally embedded in the ice, thus increasing the number of small grains. Such a process was invoked in the models of Jura (2004). Thus, although sublimation may truncate the size distribution, and so reduce the number of small grains, it may also lead to the production of an extra population of small grains. Due to this complexity in behaviour it is not clear that sublimation cleanly truncates the size distribution and it is therefore assumed not to dominate over other processes in the current models and its effect is discussed further in §3.6.2.1.

3.5.4.6 Summary

The five processes that could potentially remove the smallest particles from the disc have been discussed. Fig. 3.6 provides a summary of which processes are relevant as the star evolves. Radiation pressure removes the largest particles from the disc throughout most of its evolution, apart from on the AGB when stellar mass loss rates are high and relatively large objects are removed from the collisional cascade by stellar wind drag. PR-drag is only relevant for small radii discs on the main sequence and giant branch. Uncertainties in the outcome of sublimation mean that the models presented in this paper assume that discs are unaffected by this process; the implications of this assumption are discussed in §3.6.2.1. The maximum of D_{bl}, D_{SWPR}, D_{PR} and D_{SW}, as shown in Fig. 3.6, was used to determine the cut-off of the collisional cascade, D_{min}, in my models. For epochs where D_{min} decreases with time, a time delay would be expected

before the small grains are replenished by collisions. However in these models I assume that this delay is shorter than the timescales considered and that the collisional cascade is instantaneously replenished. For example at the start of the white dwarf phase D_{min} decreases rapidly. I assume that although the collisional lifetime of large bodies is long, this is not the case for small bodies and these will therefore be replenished quickly by collisions.

3.6   Observations

The preceding section discussed the various processes that affect the disc as the star evolves. Combining these processes, together with a knowledge of the change in stellar properties as the star evolves (Fig. 3.1), the evolution of a debris disc and its observable properties on the post-main sequence can be modelled. The evolution of an individual disc is, of course, dependent on its initial conditions, characterised in the current models by its radius, initial mass, distance from earth and the spectral type of the star. In this section I first consider the evolution of an individual disc, with a given set of parameters, and then proceed to discuss the evolution of the population of debris discs observed on the main-sequence around A stars.

The two quantities of relevance to observations of the disc are its flux (F_{disc}) and the ratio of the flux from the disc to the flux from the star (R_ν). In order for a disc to be detected by a given instrument, at a given wavelength, its flux (F_{disc}) must be above the sensitivity limit for that instrument (F_{sens}), and the ratio of the flux from the disc to the flux from the star (R_ν) must be above the calibration limit ($R_{\nu,\mathrm{lim}}$). The calibration limit is set by the accuracy to which the stellar flux is known and the quality of the instrumental calibration. Here it is assumed that all far-IR measurements have the same calibration limit as Spitzer at 70μm ($\sim$0.55), whilst mid-IR measurements, such as Spitzer at 24μm have a calibration limit of $\sim$0.1. Although the instrument calibration for Herschel is quoted as 0.1 (Poglitsch and Waelkens, 2010), once the uncertainty in the stellar flux is included the limit will be similar to that for Spitzer at 70μm.

3.6.1 Evolution of a 100AU disc around a 2.9M$_\odot$ star at a distance of 10pc

Fig. 3.10 shows the evolution of F_{disc} and $R_{70\mu m}$ at 70μm, for a disc initially at 100AU, with a mass of 1, 10 or $100M_\oplus$, around a $2.9M_\odot$ star at 10pc. The blue lines show the sensitivity and calibration limits for Spitzer at 70μm, respectively. The disc is detectable if both F_{disc} and $R_{70\mu m}$ are above these limits. From these plots it can be seen that a disc of these initial conditions can be detected on the main sequence, early on the giant branch and early in the white dwarf phase. The exact values of F_{disc} and $R_{70\mu m}$, relative to the calibration and sensitivity limits, vary significantly for discs of different radius, initial mass, distance from earth or around different spectral type stars, however the form of these plots, in terms of when F_{disc} and $R_{70\mu m}$ increase or decrease relative to the evolutionary phase of the star, remains relatively unchanged. The discussion begins below by considering the variation of F_{disc} and $R_{70\mu m}$ during the evolution of a disc with a given set of initial parameters and then goes on to consider the changes to this evolution when these initial parameters of the disc are varied in §3.6.1.1, §3.6.1.2 and §3.6.1.3.

Along the main sequence the stellar properties change only by a small amount and the evolution of the disc is unchanged from that in Wyatt et al. (2007b). The flux from the disc falls off with time as collisional evolution depletes the mass in the disc. Observations of discs around nearby stars with Spitzer at 70μm are in general calibration limited, and the example shown at 100AU is detectable throughout the main sequence.

On the giant branch, the stellar luminosity increases by several orders of magnitude (see Fig. 3.1). The increase in stellar luminosity heats the disc, however the increase in disc flux is small since all the small grains that would dominate the emission are removed by radiation pressure (see middle panel of Fig. 3.7). There is a substantial decrease in $R_{70\mu m}$ with time along the giant branch, since the increase in stellar flux is large, whilst the increase in F_{disc} on the giant branch is relatively small. The difficulty in observing discs around giant stars is therefore the calibration limit, as can be seen in Fig. 3.10 for the example disc for which
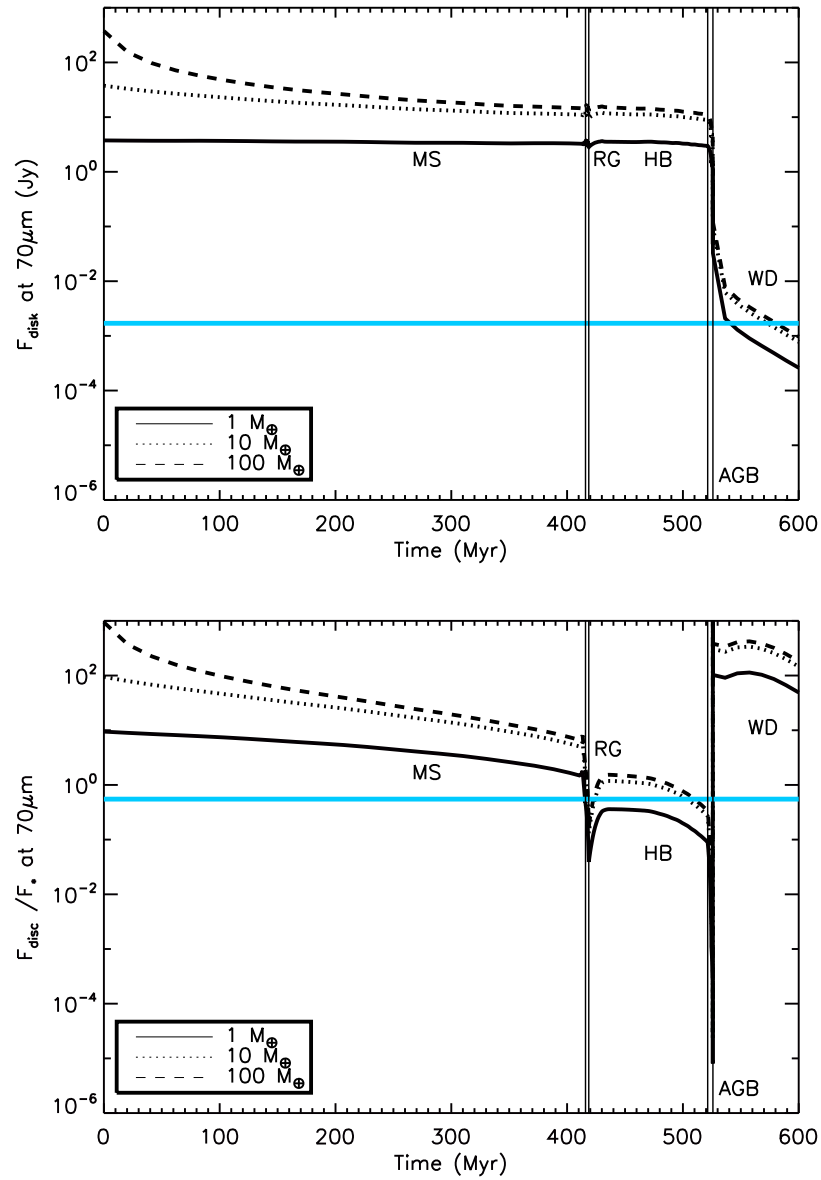
Figure 3.10 – The evolution of the total flux from the disc (top panel) and the ratio of the flux from the disc to the flux from the star (bottom panel) at 70μm, as the star evolves. The thick blue line in the upper plot is the sensitivity limit of 110μJy, whilst in the bottom plot it shows the calibration limit of $R_{\text{lim}} = 0.1$, for Spitzer at 70μm. The star is a $2.9M_{\odot}$ star, with solar metallicity ($Z = 0.02$), at 10pc and the disc has an initial radius of 100AU. MS: main sequence, RG: first ascent giant branch, HB: core-helium burning phase, WD: white dwarf.

$R_{70\mu m}$ is only greater than $R_{70\mu m,\text{lim}}$ for the first half of the star's giant branch evolution.

As the star starts burning helium in its core, its luminosity decreases from the maximum value on the giant branch, but remains higher than on the main sequence, whilst the stellar temperature remains low (see Fig. 3.1). The combination of these means that the stellar flux is high and $R_{70\mu m}$ is small, less than $R_{70\mu m,\text{lim}}$, for the $10\text{M}_{\oplus}$ example disc, at 10pc, shown in Fig. 3.10. Although this example disc is detectable, many discs around core-helium burning stars in my population are not.

As helium in the core is exhausted, the star swells to become an asymptotic giant branch star. It ejects a significant proportion of its mass in a stellar wind and the smallest grains are removed by stellar wind drag ($D_{min} = D_{SWPR}$ Eq. 3.23). The stellar luminosity increases and heats the disc such that F_{disc} remains high, despite the fact that D_{min} is relatively large. This means that $R_{\nu} < R_{\nu,\text{lim}}$ and discs do not have an observable excess. However AGB stars may be surrounded by expanding circumstellar envelopes of material ejected from the star in a stellar wind and emission from these dust shells would be significantly brighter than a debris disc in the infra-red or sub-mm.

After mass loss ceases, the white dwarf core evolves swiftly to higher effective temperature at constant luminosity, before the stellar luminosity starts to fall as the star cools as a white dwarf. As the stellar luminosity decreases, R_{ν} increases and it becomes possible to detect emission from this example debris disc. For this short evolutionary epoch the star is defined as a post-AGB or pre-white dwarf, as discussed in §1.2.6. For the purposes of these models I have defined the post-AGB phase as the 0.1Myr before the start of the white dwarf phase.

There is a sharp drop in stellar luminosity as the stellar envelope is ejected and the stellar core is exposed as a white dwarf. This means that the ratio of the stellar luminosity to the disc flux increases significantly and that observations are no longer calibration limited. However the disc flux falls rapidly below the sensitivity limit as the white dwarf cools and it is this limit that determines whether a white dwarf debris disc is detectable. As discussed in §3.5.4.1 even though there is no process to remove small dust created in collisions, the flux from these small grains is small and does not make a white dwarf debris disc

detectable. As can be seen in Fig. 3.10, F_{disc} is only greater than F_{sens} for very young white dwarfs.

3.6.1.1 Dependence on disc parameters

Changes in F_{disc} and R_ν with initial disc mass and radius are interlinked. Simplistically F_{disc}, and thus R_ν, is proportional to disc mass and hence discs that are more massive are easier to observe. The collisional evolution of material in the disc, however, means that there is a dependence of disc mass at later times on disc radius, since the collisional lifetime is shorter for close-in discs than for those further out (Eq. 2.28). For discs that have reached collisional equilibrium their mass, at a given age, is independent of their initial mass but increases with disc radius (Eq. 2.31). Discs at large radii, on the other hand, will not have reached collisional equilibrium and so retain their initial mass. This leads to the behaviour of F_{disc} with radius shown in the bottom panel of Fig. 3.11. For close-in discs the disc mass and thus F_{disc} increases with radius, despite the decrease in disc temperature. For large radii discs, on the other hand, there is a significant variation in F_{disc} with initial disc mass and F_{disc} decreases with radius or disc temperature. This behaviour is of particular importance in determining which radii discs are the brightest at a given epoch. As can be seen for a given individual disc mass, the brightest discs at some later epoch are those with intermediate radii at which the largest planetesimals are just reaching collisional equilibrium at this age.

3.6.1.2 Dependence on stellar parameters

The simplest scaling relation is the distance to the star. R_ν is unchanged, whilst F_{disc} scales inversely with distance squared. At large enough distances observations are always sensitivity limited.

In the current models stars with mass between 1.67 and 3.8 $M_\odot$ or spectral type A9-B8 are considered. The difference between these models that has the greatest effect on the disc is the stellar luminosity. More luminous stars have brighter discs, although this increase is not as large as might be expected because the blow-out size also increases with stellar luminosity. Thus, the ratio of the

disc flux to the stellar flux decreases with stellar luminosity, since the increase in stellar flux is larger than the increase in disc flux. In terms of Fig. 3.10 this means that, for higher luminosity stars, the upper plot is shifted upwards relative to the sensitivity limit, whilst the lower plot shifts downwards. As was discussed in §3.3 the stellar luminosity increases the most on the giant branch for lower mass stars and therefore F_{disc} and R_ν show the greatest variation on the giant and asymptotic giant branch for these stars.

There is also a dependence in disc mass on main-sequence lifetime for collisionally evolving discs. Later spectral type stars take much longer to evolve and therefore the reduction in their disc mass at a given epoch is larger, however the difference in disc flux due to this is small compared to the difference due to the change in stellar luminosity.

In terms of detecting discs, this means that where observations are calibration limited, discs are more detectable around the least luminous stars. This applies to lower mass stars on the main sequence, or early on the giant branch. On the other hand when observation are sensitivity limited, *i.e.* around white dwarfs, discs are more detectable around the most luminous, or higher mass stars.

3.6.1.3 Dependence on wavelength of observations

The above discussion has focused on observations with Spitzer at 70μm. The form of the upper panels of Fig. 3.11 remain relatively unchanged as observations are made in different wavelengths however the exact values of F_{disc} and R_ν relative to the sensitivity and calibration limits vary significantly. The disc flux peaks at approximately the peak emission wavelength for a blackbody of the disc temperature. The ratio of the disc to stellar flux also has a similar variation with wavelength, however it peaks at longer wavelengths, since F_* falls off more rapidly with wavelength than F_{disc}. Variations in F_{disc} and R_ν are larger for shorter wavelengths, where the emission is from the Wien region of the blackbody spectrum.

All of this behaviour, means that there will be an optimum wavelength for detecting discs that depends on disc temperature, and whether observations are sensitivity or calibration limited. When observations are sensitivity limited discs

are most detectable for the wavelength at which F_{disc} is maximum, given by Wien's displacement law for a disc of a given temperature, around 100μm for young white dwarfs. Alternatively when observations are calibration limited, the most discs are detectable for the wavelengths at which R_ν is maximum, for example on the giant branch this varies between 100 and 800μm.

3.6.2 Population models

Using my models the evolution of a disc, with a given set of initial parameters, can be determined. Here I apply these models, to the population of discs on the main sequence known from observations of A stars by Spitzer and the models of Wyatt et al. (2007b) (see §. 3.4). These discs are evolved from the main sequence through to the white dwarf phase and the population of discs around evolved stars is determined. The following discussion focuses on giant stars, post-AGB stars and white dwarfs. AGB stars are not discussed because debris discs are not detectable during this phase, and in any case observations would be complicated by the presence of material emitted in the stellar wind.

There are many surveys for debris discs with recent and current instruments, such as Spitzer and *Herschel*, as well as up-coming instruments such as ALMA. Here I calculate the percentage of the evolved population that are detectable with various instruments. Table 3.1 shows these percentages for young white dwarfs, giant and main-sequence stars.

It is important to note that these percentages only correspond to the population of evolved A stars, not the entire population of giants or white dwarfs. The number of discs that these percentages correspond to can be calculated from the space density of A stars from Phillips et al. (2010) of 0.0014 ± 0.0001 pc^{-3} and the average main-sequence lifetime for A stars, 950Myr, to give a density of 3.5×10^{-5}pc^{-3} for evolved A stars on the first ascent giant branch, 2.5×10^{-4}pc^{-3} for core-helium burning stars and 1.47×10^{-4}pc^{-3} for white dwarfs with a cooling age of less than 100Myr. It is not possible to tell from observations of giant stars whether they are evolved FGK or A stars and it is therefore hard to compare the populations, however the majority of white dwarfs currently observed are evolved A stars and these space densities make a reasonable comparison with the 80%

complete catalogue of Sion et al. (2009); the number of white dwarfs within 10pc less than 100 Myr old is predicted to be 0.6 and less than 1000Myr within 20pc is predicted to be 50, compared to 0 and 30 (Sion et al., 2009). This catalogue contains no white dwarfs with cooling ages of less than 1Myr within 20pc.

3.6.2.1 Giant stars

Early on the giant branch a small set of the evolved population of debris discs have a detectable excess. The following discussion defines which discs are detectable, in terms of the parameter space specified by initial disc radius, initial disc mass, distance to the star, wavelength for observations and mass of the star. In order to assess this the disc flux is plotted as a function of radius in the bottom panel of Fig. 3.11. As discussed in §3.6.1.1, this peaks at intermediate radii because collisions have depleted the mass in close-in discs, such that $F_{disc} \propto M_{max} \propto r^{7/3}$ (Eq. 2.31), whereas large disc radii retain their initial masses, and the disc flux falls off with the disc temperature or radius. Only discs with $R_\nu > R_{lim}$ are detectable, or those with fluxes above the solid lines in the upper panel of Fig. 3.11, excluding both small and large radii discs.

This dependence leads to the form of the upper left panel of Fig. 3.11, the solid area of which shows the discs that can be detected with various instruments. The upper curve is the sensitivity limit, whilst the cut-off at low and high radii are from the calibration limit. This plot varies with mass and age of the star, as well as the mass of the disc and wavelength for observations. As can be seen for the example disc shown, around an evolved $1.67M_\odot$ star, of initially $10M_\oplus$ at the start of the giant branch, only discs with radii of around 100AU, within ~ 200pc of the Sun, are detectable with Spitzer, *Herschel* or ALMA at the wavelengths considered. As the luminosity of the star increases along the giant branch, the distance out to which discs can be detected increases, however the range of radii of discs with detectable excess decreases. This means that the solid (detectable) area of an equivalent to the middle panel of Fig. 3.11 is largest for the least luminous giants. The dependence of disc flux on wavelength discussed in §3.6.1.3 means that the solid (detectable) area is largest for *Herschel* PACS at 160μm.

A smaller fraction of the population has detectable excess on the giant branch
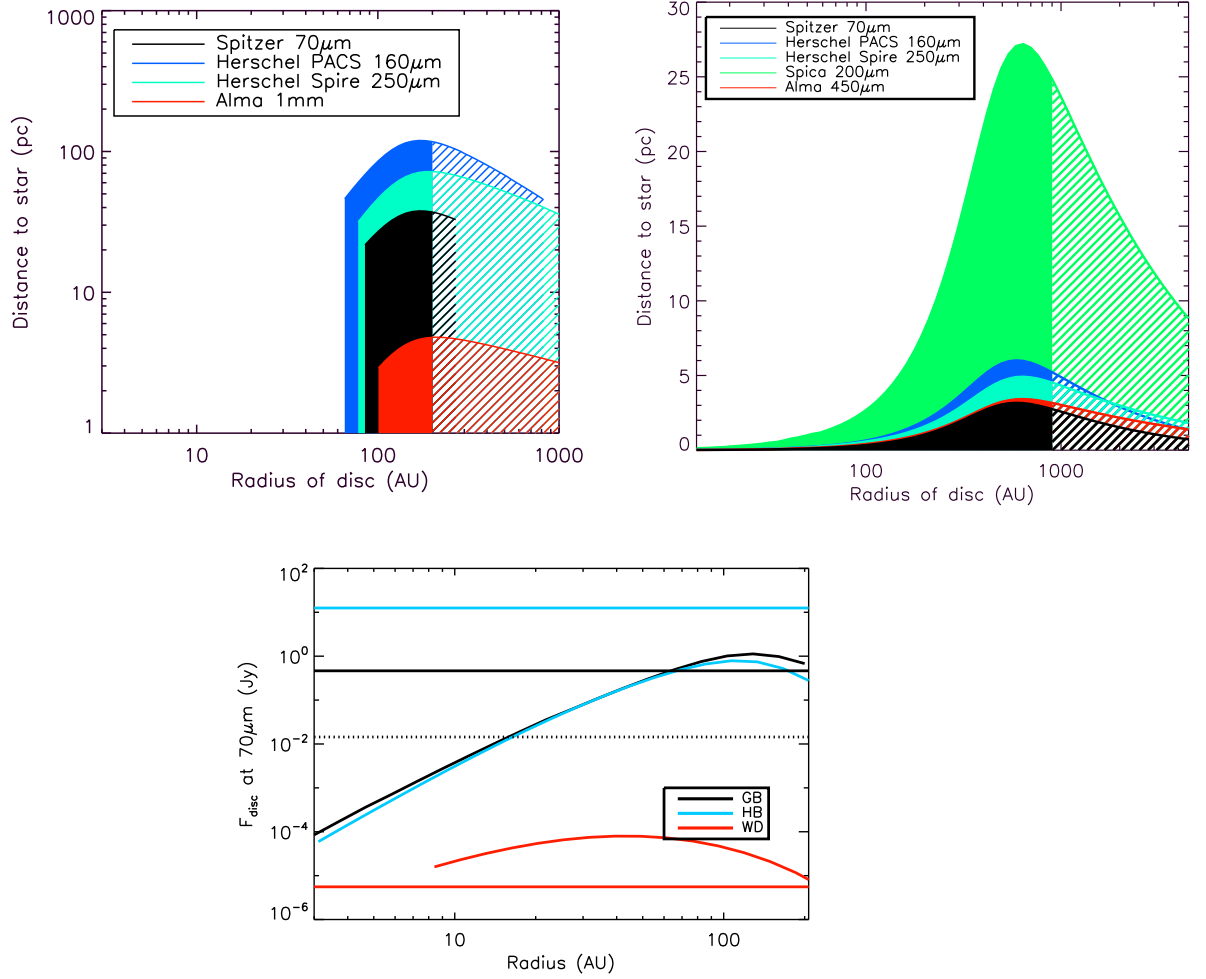
Figure 3.11 – Observations of the disc. Top right: Detection limits for discs of initially $10M_{\oplus}$, around a star of $1.67M_{\odot}$, at the base of the giant branch ($L_* = 10.2L_{\odot}$). Excesses can be observed for the discs that fall within the solid filled regions for *Herschel* PACS at 160μm, *Herschel* SPIRE at 250μm, ALMA at 1mm and Spitzer at 70μm. The dashed filled regions are for discs with radii larger than 200AU, not included in the current models, that can be detected. A calibration limit of $R_{\nu,lim} = 0.55$ is assumed for all instruments.

Top left: same as top right but for a $3.8M_{\odot}$ (equivalent to B8) star that has evolved to become a 1Myr old white dwarf. Note that the disc radii are 4 times larger than on the main sequence.

Bottom: The variation in disc flux with radius for a $1.67M_{\odot}$ star on the giant branch (2000Myr) (black line), core-helium burning star (2200Myr) (blue line) and around a white dwarf (cooling age of 1Gyr) (red line), for discs with an initial mass of $10M_{\oplus}$. The horizontal lines show the calibration limits for Spitzer at 70μm on the giant branch (black), horizontal branch (blue) and white dwarf phase (red), respectively, whilst the dotted horizontal line shows the sensitivity limit.

Instruments	Sensitivity (mJy)	Main Sequence d< 100pc	Giant Branch d< 100pc	Core-helium burning stars d< 50pc L< $100L_\odot$	Post-AGB d< 200pc $t > t_{WD}$-0.1Myr $t < t_{WD}$	White Dwarf $d < 10$pc $t_{WD} < 1000$Myr
		%	%	%	%	
IRAS at 60μm[b]	100^c	4.6	1.7	0.6	1.8	<0.1
Spitzer at 24μm	0.11 [d]	51.0	14.0	20.5	<1.0	<0.1
Spitzer at 70μm	14.4^d	39.0	9.3	<1.0	6.3	<0.1
Spitzer at 160μm	40 [d]	13.0	4.2	1.0	5.7	<0.1
Herschel PACS at 70μm	4^e	44.0	9.6	<1.0	9.1	<0.1
Herschel PACS at 160μm	4^e	35.0	12.2	1.0	9.1	1.6
Herschel SPIRE at 250μm	1.8^e	33.0	12.8	2.5	22.6	1.9
Herschel SPIRE at 350μm	2.2^e	23.0	10.8	3.0	11.4	1.0
ALMA at 450μm	80^f	19.0	7.0	3.0	12.6	1.1
ALMA at 1.2mm	0.25	10.7	2.2	<0.1	22.6	2.5
Spica at 200μm	0.1^g	45.0	12.0	1.5	22.6	23.70
No. of stars[h]		5860^b	1050^b	130^b	5.0	6.6^b

All results for $\lambda > 70\mu$m use the calibration limit of Spitzer at 70μm.
[b] Only stars with magnitudes brighter than 4.0 are considered such that the sample can be compared with Jura (1990)
[c] http://irsa.ipac.caltech.edu/IRASdocs/iras_mission.html
[d] Wyatt (2008)
[e] http://herschel.esac.esa.int/science_instruments.shtml
[f] http://www.eso.org/sci/facilities/alma/observing/specifications/
[g] Swinyard and Nakagawa (2009)
[h] The number of evolved A stars, calculated from the space density of A stars (Phillips et al., 2010)

Table 3.1 – Detection of discs around evolved stars

than the main sequence, as can be seen in Table 3.1. The significant increase in stellar luminosity, compared to the small increase in disc flux means that fewer discs are detectable over the stellar emission ($R_\nu > R_{lim}$). Spitzer at $24\mu m$ can detect the largest fraction of the population, because observations are calibration limited and the calibration limit in the mid-IR is lower than in the far-IR. *Herschel* SPIRE detects the next highest fraction of the population due to the wavelength dependence of R_ν, peaking in the sub-mm, as discussed in §3.6.1.3. A sample of stars within 100pc are considered in Table 3.1. However, if observations with, for example, ALMA were made with the intention of detecting such discs, a sample that only extended out to smaller distances would maximise the rate of detection.

My models suggest that around 10% of evolved A stars on the giant branch have detectable excess with Spitzer or *Herschel*. This is, however, subject to the unclear effect of sublimation on debris discs. Sublimation could have two possible effects. Either it removes all small grains, truncating the collisional cascade, and thus decreasing the number of discs with detectable excess, or it releases a population of small silicate grains, increasing the number of giants with detectable excess. This makes future observations of giant stars with *Herschel*, in comparison with my models, very interesting, as they have the potential to constrain the effects of sublimation on discs.

My models, however, compare favourably with the sample of 44 giants brighter than $m_v = 4.0$ mag (Jura, 1990) (see Table 3.1), none of which display excess at $60\mu m$ ($< 3\%$) with IRAS. Infrared excess is, however, found around 300 of the 40,000 G and K giants in the Bright Star Catalogue and Mitchigan Spectral Catalogue (Zuckerman et al., 1995), although the origin of this emission is not clear. 12 of these sources are modelled in further detail in Kim et al. (2001b), who suggest that they are more likely to result from sporadic dust ejection or emission from nearby interstellar cirrus rather than black-body grains in a Kuiper-belt disc. In order to compare observations of giant stars with my models it would be necessary to distinguish between these scenarios, potentially with high resolution imaging.

Another factor that could significantly change the detectability of discs around giant stars is the radius distribution of discs in my population. My models only included discs detected with Spitzer at $24\mu m$ and $70\mu m$ and therefore there is a

bias towards small radii discs. This is particularly relevant, as large radii discs are detectable, particularly at longer wavelengths (see middle panel of Fig. 3.11). This could be accounted for by extending my models to include sub-mm observations of debris discs on the main sequence or incorporating this radius bias into my modelling of the main-sequence population. Including observations of discs around main-sequence FGK stars would also make my models more directly comparable with a sample of giant stars. Given these extensions and a technique to distinguish emission from a debris disc to that from stars undergoing sporadic dust ejection or emission from nearby interstellar cirrus, it should be possible for future observations with *Herschel* or ALMA to determine the effect of sublimation on debris discs.

3.6.2.2 Core-helium burning stars

The majority of the discussion in §3.6.2.1 also applies to core-helium burning stars. Observations are also calibration limited, however significantly fewer discs are detectable around core-helium burning stars than giant stars, since the stellar flux is on average higher, whilst the disc flux remains approximately constant. In order to maximise the percentage of discs with detectable excess observations should focus on low luminosity core-helium burning stars. In Table 3.1 the percentage of the population of core-helium burning stars within 50pc and with luminosities lower than $100L_{\odot}$ were calculated. Observationally it may be that core-helium burning stars in a sample are indistinguishable from giants and therefore it may be necessary to add the detection probabilities for discs around core-helium burning stars to those for discs around giant stars.

3.6.2.3 White dwarfs

As can be seen in Fig. 3.10 the disc flux falls off rapidly as the star cools during the white dwarf phase and it is therefore very hard to detect debris discs around white dwarfs. Observations of debris discs around white dwarfs in my baseline model are sensitivity limited and only the most massive discs around the closest, youngest white dwarfs are detectable. By the same analysis as in §3.6.2.1 the bottom panel of Fig. 3.11 shows the distance out to which discs of initially $10M_{\oplus}$
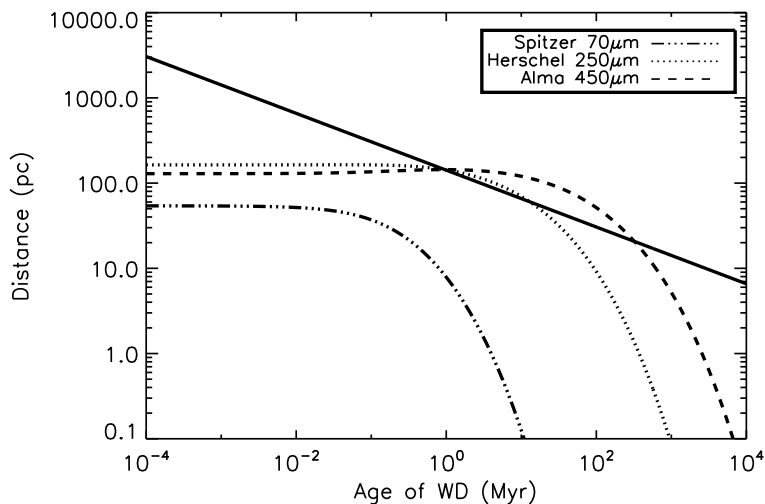
Figure 3.12 – The solid line shows the maximum distance out to which a disc initially at 100AU, with a mass of $10M_\oplus$, around an evolved $3.8M_\odot$ white dwarf, of a given age can be detected with Spitzer at 70μm, *Herschel* SPIRE at 250μm and ALMA at 450μm, whilst the dotted line shows the distance within which there is one white dwarf younger than the given age, calculated using the space density of A stars from Phillips et al. (2010).

can be detected around an evolved $3.8M_\odot$ (equivalent to B8) star, with a white dwarf cooling age of 1Myr. Thus for discs in my baseline model (initial radii less than 200AU) around white dwarfs that are younger than 1 Myr, the disc flux is so low that it is only those that are within a couple of parsecs of the Sun that are detectable with Spitzer, *Herschel* or ALMA. Even the increased sensitivity of Spica only means that discs out to tens of parsec are detectable.

Similarly to discs around giant stars, it is the large radii discs that retain the highest mass at late times, that are therefore the most detectable. As can be seen in the bottom panel of Fig. 3.11, F_{disc} peaks at $\sim$200AU for a disc of initially $1M_\oplus$ around the 1Myr old white dwarf considered. This radius increases with initial disc mass or white dwarf cooling age.

There is, however, a balance between young white dwarfs being the most luminous and therefore having the brightest discs and the low volume density of young white dwarfs such that they are more likely to be found at greater distances from the Sun. Fig. 3.12 shows the maximum distance out to which discs around
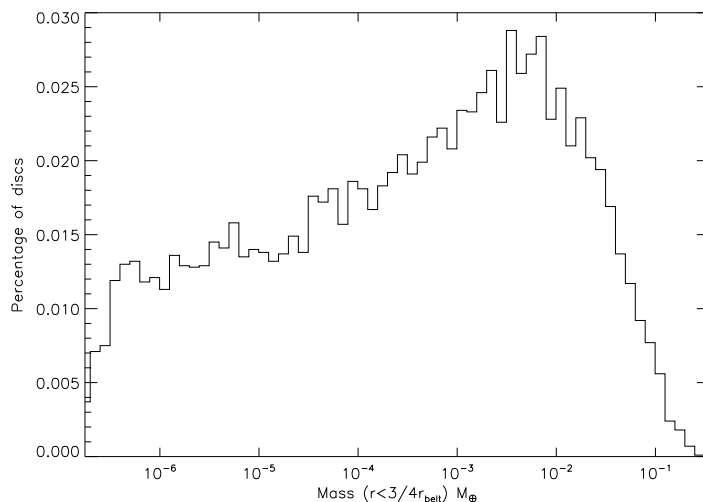
Figure 3.13 – A histogram showing the amount of mass left inside of the main belt (between $r = 0$ and $r = \frac{3}{4}r_{belt}$) at the end of the AGB for the population of discs in my models.

white dwarfs can be detected as a function of cooling age, for discs at 100AU with Spitzer at 70μm, *Herschel* SPIRE at 250μm and ALMA at 450μm. This is compared to the distance within which one white dwarf of a given cooling age is found, according to the space densities of Phillips et al. (2010). The maximum distance out to which discs can be detected is never significantly greater than the distance within which there is one white dwarf and it is therefore unlikely that such a system can be observed. There is an optimum cooling age for detecting white dwarf discs, which varies with wavelength, for Spitzer at 70μm it is ∼1Myr, whilst for *Herschel* SPIRE at 250μm it is ∼10Myr and ALMA at 450μm ∼100Myr. As the disc temperature drops, the disc flux decreases, more rapidly at the shorter wavelengths. This means that for a young population of white dwarfs, the best chances of detecting debris discs are at the shorter wavelengths of Spitzer or *Herschel*, whilst for a sample that includes older stars ALMA would be better. However, overall, the best chances of detecting such a system are with the longer wavelengths of *Herschel* or ALMA.

Focusing on Spitzer at 70μm, if for some reason my models under-predicted the flux from (or mass in) such discs by approximately an order of magnitude a disc would be most likely to be detected around a white dwarf of less than 5Myr

old at a distance of around 200pc. At the time of this work, the only detection of excess around a white dwarf that resembles a main-sequence debris disc was the helix nebula (Su et al., 2007), a young white dwarf with a cooling age significantly less than 5Myr, surrounded by a planetary nebula at 219pc. This fits nicely with my models, especially given that alternative explanations that increase the disc flux exist, for example the trapping of bodies in resonances (Dong et al., 2010). There are now 6 further young white dwarfs with infra-red emission (Chu et al., 2011), awaiting *Herschel* observations that confirm their disc-like nature.

There are very few young white dwarfs close to the Sun, therefore assuming that my models are correct, the best chances of detecting a white dwarf debris disc are to observe nearby white dwarfs with ALMA. Table 3.1 shows the percentage of the population of white dwarfs within 10pc with a cooling age of less than 1000Myr. According to the space densities of (Phillips et al., 2010) there are only 6 white dwarfs in this distance, and even less from Sion et al. (2009), and therefore the chances of one of these white dwarfs having a debris disc within the narrow initial radius and initial mass range such that it is detectable is slim. Increasing the distance limit of the sample does not improve matters as at greater distances the disc flux falls below the sensitivity limit. Even with the increased sensitivity of Spica the chances of observing such a disc around a white dwarf are slim.

These low probabilities for detecting debris discs around white dwarfs fits with the fact that Spitzer observations of white dwarfs that have found very few white dwarfs with infrared excess fitted by a disc with a radius of the same order of magnitude of main-sequence debris discs. There are, however, as discussed in §1.3.3 ∼20 observations of hot, dusty discs around white dwarfs that are best fitted by discs of radii on the order the solar radius *e.g.* Farihi et al. (2009), Reach et al. (2005). Farihi et al. (2009) estimate that 1-3% of white dwarfs with cooling ages less than 0.5 Gyr possess excess emission in the near-infrared. The minimum radius of a disc in my population is ∼6AU and therefore these observations cannot be explained by the discs in my population. Material in discs with such a small radius will have a very short lifetime and must, therefore, be replenished. Within the context of the current model I have identified a potential source of material for such discs. Stellar wind drag was included in the current models in as far

as it truncates the collisional cascade on the AGB. Material that leaves the disc will spiral in towards the star, most of it being accreted on to the star during the AGB, however some mass will be left between the inner edge of the belt and the star, at the end of the AGB. Fig. 3.13 shows this mass for all the discs in my population. The masses in Fig. 3.13 are significantly higher than the typical dust masses for these hot discs *e.g.* $3.3 \times 10^{-10} M_{\oplus}$ of GD166-58 (Farihi et al., 2008), and there are even a significant proportion of the population with more mass than the largest such disc, GD362, with a mass of $0.017 M_{\oplus}$ (Jura et al., 2009). However a mechanism is still required to move this material in closer to the star. This could potentially be scattering by planets inside of the disc or the dynamical effects of mass loss on the disc. These effects are considered in more detail in Chapter 4.

3.6.2.4 Post-AGB or pre-WD stars

As discussed earlier in Sec 3.6.1.2, the stellar flux from AGB stars is so high that it is hard to detect emission from a debris disc. However as the stellar luminosity starts to drop just before the start of the white dwarf phase it is possible to detect discs around a small proportion of stars (see Table 3.1). The analysis is very similar to that for young white dwarf stars, discussed in the previous section. The only difference is that it is possible to observe discs around somewhat more distant stars, as the star and disc are brighter. However, since the post-AGB phase is shorter the density of such stars is lower. The chances of detecting such a system are therefore slim. Many post-AGB stars have infra-red excess associated with dust discs or shells, however, as discussed in §1.2.6 this dust is thought to be stellar in origin and associated with the binarity of the star.

3.7 Conclusions

This work provides a theoretical framework that considers all of the effects of stellar evolution on debris discs, firstly considering the evolution of an individual disc, before extending this to the known population of debris discs around main-sequence A stars. I found that debris discs are harder to detect around evolved

stars than on the main sequence. The fraction of discs with detectable excess decreases significantly on the giant branch, yet further for core-helium burning stars and discs around white dwarfs are very hard to detect, although the limitations during this phase are different to earlier in the star's evolution.

The population of discs on the main sequence is constrained by Spitzer observations of A stars (Rieke et al., 2005; Su et al., 2006) and the steady state collisional models of Wyatt et al. (2007b). In this chapter these models were updated to include realistic grains rather than the black body approximation used in Wyatt et al. (2007b). This was done relatively simplistically by considering that the difference in behaviour between realistic and black body grains can be explained entirely by an altered disc radius, characterised by the ratio X_{2470} between the radius calculated using realistic grains (r_{real}) and the radius calculated using a black body approximation (r_{2470}), shown in Fig. 3.2. This was used to adjust the fit from Wyatt et al. (2007b) and thus the population of discs around main-sequence A stars was determined.

In my models debris discs that are observed on the main sequence survive the star's evolution, however their properties are altered. They evolve collisionally in exactly the same manner as on the main sequence, however the longer timescales mean that, except for large radii discs, their masses are significantly reduced. Discs heat up as the stellar luminosity increases on the giant and asymptotic giant branches. The increase in disc flux, however, is relatively small since small grains are removed by radiation pressure and stellar wind drag (on the AGB only). It is shown that Poynting-Robertson drag is irrelevant for all discs, including discs around white dwarfs, the only exception being for low mass or close-in discs. Adiabatic stellar mass loss means that discs around white dwarfs have radii a factor of 2 or 3 greater than on the main sequence.

All of these changes in the properties of the disc can be put together to determine which discs can be detected. In terms of observations of discs around post-main-sequence stars, the important quantities are the disc flux (F_{disc}) and its ratio to the stellar flux (R_ν) which must, respectively, be above the sensitivity and calibration limits of the instrument considered. The variation in these are summarised in Fig. 3.10.

A smaller fraction of the population can be detected on the giant branch than

the main sequence. Observations are calibration limited. The large increase in stellar flux at the wavelengths considered, compared to the smaller increase in disc flux, means that R_ν decreases significantly and discs are hard to observe. R_ν decreases with time on the giant branch such that only large radii discs around stars early on the giant branch have a detectable excess. One limitation of my models is the uncertainty in the effect of sublimation on the disc, as discussed in §3.5.4.5. Future observations of giant stars with *Herschel* or ALMA, in comparison with my models, could potentially constrain the effects of sublimation on debris discs.

Discs around white dwarfs are very faint and thus hard to observe. Their luminosity decreases as the stellar luminosity falls off with age and the best chances of observing a disc are around very young white dwarfs close to the Sun, however there are very few such objects and thus the chances of observing such a system are small. If for some reason my models under predict the flux from such discs, then the optimum age and distance for detecting a white dwarf disc with Spitzer at 70μm would be at a distance of $\sim$200pc and an age of less than 5Myr. This fits nicely with the fact that the only white dwarfs with infra-red emission consistent with a cold dust disc are young white dwarfs. The first such detection being around WD2226-210, the young white dwarf at the centre of the helix nebula, at a distance of 219pc (Su et al., 2007).

There are however detections of hot dusty discs around $\sim$20 white dwarfs with radii less than 0.01AU. These are a different population from the discs in my models which have a minimum radius of 6AU. Within the context of my models a potential source of material to replenish such discs is material that has left the disc due to stellar wind drag, but not yet been accreted on to the star at the end of the AGB. However, a mechanism is still required to move this material in towards the star. This, and the dynamical effects of mass loss on debris discs will be discussed in the next chapter.

Chapter 4

Dynamical effects of stellar mass loss on a Kuiper-like belt.

4.1   Summary

A quarter of DA white dwarfs are metal polluted, yet elements heavier than helium sink down through the stellar atmosphere on timescales of days. Hence, these white dwarfs must be currently accreting material containing heavy elements. Here, I consider whether the scattering of comets or asteroids from an outer planetary system, following stellar mass loss on the asymptotic giant branch, can reproduce these observations. I use N-body simulations to investigate the effects of stellar mass loss on a simple system consisting of a planetesimal belt whose inner edge is truncated by a planet. My simulations find that, starting with a planetesimal belt population fitted to the observed main-sequence evolution, sufficient mass is scattered into the inner planetary system to explain the inferred heavy element accretion rates. This assumes that some fraction of the mass scattered into the inner planetary system ends up on star-grazing orbits, is tidally disrupted and accreted on to the white dwarf. The simulations also reproduce the observed decrease in accretion rate with cooling age and predict accretion rates in old (>1Gyr) white dwarfs, in line with observations. I assumed that the inner planetary system is similarly efficient as the Solar System at scattering particles on to star-grazing orbits. The simulations show that a single

planet is not sufficient. Although the correct level of accretion is reproduced, the simulations predict a higher fraction of accreting white dwarfs than observed. This could indicate that the average evolved planetary system is less efficient at scattering bodies on to star-grazing orbits or that dynamical instabilities post-stellar mass loss cause rapid planetesimal belt depletion for a significant fraction of systems.

4.2   Introduction

Keck observations of cool single DA white dwarfs find that $\sim 25\%$ contain elements heavier than helium in their spectra (Zuckerman et al., 2003). These elements sink rapidly in the white dwarf's atmosphere and their presence means that these white dwarfs must be currently accreting material containing heavy elements. Initially it was thought that these observations were a signature of accretion from the interstellar medium. This was ruled out by a lack of correlation between their accreted calcium abundances and spatial kinematical distributions relative to interstellar material (Farihi et al., 2010a). The best models to explain these systems (Debes and Sigurdsson, 2002; Jura, 2003; Gänsicke et al., 2006; Kilic et al., 2006; von Hippel et al., 2007b; Farihi et al., 2009, 2010b; Melis et al., 2010) suggest that asteroids or comets from the remnants of main-sequence planetary systems are scattered on to orbits that approach close to the star, due to altered dynamics following stellar mass loss on the asymptotic giant branch. Bodies that come within the tidal radius of the star are disrupted, potentially forming a dusty disc, before accreting on to the star. Spitzer observations of some of the most highly polluted systems find excess emission in the near-infra-red, consistent with a close-in dusty disc. Such a disc is observed around 1-3% of white dwarfs with cooling ages less than 0.5Gyr (Farihi et al., 2009).

Although the disruption of an asteroid or comet is widely quoted as the explanation for such systems, the feasibility of this process has not been thoroughly investigated. Evidence that the accreted material is asteroidal in nature is high. The composition of the accreted material in systems such as GD40 (Klein et al., 2010) highly resembles asteroids in our solar system. First, in order for this to be the case, planetesimals must survive the star's evolution. Considering only stellar

wind drag and sublimation, Jura (2008) shows that asteroids of 1-10km in size survive the giant branch evolution outside of 3-4AU. In Chapter 3 I modelled in more detail the evolution of the observed population of debris discs around main-sequence A stars, showing that white dwarfs should have outer planetesimal belts, but that these are hard to detect.

A mechanism is still required to transport material from an outer planetesimal belt to the star. Although other suggestions, such as stellar encounters (Farihi et al., 2011), have been made, scattering by planets is the most likely mechanism. It is not clear whether planets will survive the star's evolution. Many close-in planets will be swallowed by the expanding stellar envelope whilst the star is on the giant branch (e.g. Villaver and Livio (2007)). Multi-planet systems may also become dynamically unstable post-stellar mass loss (Debes and Sigurdsson, 2002), and planets may be ejected or collide with the star.

The dynamics of multi-planet systems post-stellar mass loss are complicated. Here, I focus on the effects of stellar mass loss on a single planet and a planetesimal belt. Observations suggest that many debris discs have their inner edges sculpted by planets, similar to the famous example of Fomalhaut (Chiang et al., 2009). Therefore, I consider a planetesimal belt with an interior planet, close enough to the belt such it truncates the inner edge, similar to Neptune and the Kuiper belt in our Solar System. The planet dominates the dynamics of bodies at the inner edge of the disc and material inside of the chaotic zone surrounding the planet's orbit (Wisdom, 1980) will be cleared, due to the overlap of mean motion resonances. As the star loses mass the size of the chaotic zone increases and extra material is scattered from the belt. Here I use N-body simulations to investigate the fate of this scattered material and whether the evolution of this simple system post-stellar mass loss can explain the white dwarf observations. In §4.3 I describe the set up for the simulations. In §4.4 I outline results from my initial simulations that mimic the main sequence evolution of the belt and set up the initial conditions, whilst §4.5 describes simulations that include stellar mass loss. In §4.6 I compare my simulations to the white dwarf observations and finally in §4.7 I conclude and summarise this chapter.

4.3   Setup

In order to investigate the dynamical effects of stellar mass loss on planetesimal belts I consider a simplistic planetary system architecture. My simulations include a planet and a planetesimal belt orbiting a central star that undergoes mass loss. The main aim is to investigate the fate of the planetesimals in the belt after the star has lost mass. In particular, I consider the feasibility of scattering enough bodies towards the central star in order to produce the close-in, dust discs observed around some white dwarfs.

The simulations are performed using *Mercury* (Chambers, 1999) with the RADAU integrator. They are set up with a star of mass $M_*(t)$, a planet of mass M_{pl} on a circular orbit and N mass-less test particles, in a belt initially outside of the planet's orbit. *Mercury* was altered such that the central star's mass changes as a function of time. The test particles are distributed in semi-major axis from the planet's semi-major axis a_{pl} to $a_{max} = (\frac{2}{1})^{2/3}a_{pl}$, the 2:1 mean motion resonance, the same outer edge as the Kuiper belt (Trujillo and Brown, 2001; Allen et al., 2001).

Typically, high mass loss rates on the AGB last for $\sim 10^5$yrs. In all my simulations I consider a $1\text{M}_\odot$ star that loses $\frac{2}{3}$ of its mass, at a constant rate, over 10^5yrs, however the rate of mass loss and timescale, so long as they are adiabatic, do not affect the simulations. Since many particles are removed on short timescales I model the belt expected at the onset of the AGB phase by first running the simulation for the main-sequence lifetime, t_{MS} and removing any objects classed as scattered disc (see later), in addition to those ejected or scattered in. Test particles are given randomly selected initial semi-major axis between a_{pl} and a_{max}, eccentricity between 0 and e_{max}, inclination between 0 and i_{max}, and mean anomaly, argument of pericentre and longitude of ascending node between 0 and 2π. Although test particles in these simulations are evenly distributed in semi-major axis, different radial surface density distributions can be considered by appropriate weighting of particles. Each particle is assigned a mass based on its initial semi-major axis and a disc of mass M_{tot}, distributed between a_{pl} and a_{max}, with a surface density given by

$$\Sigma(r)dr \propto r^{-\alpha}dr, \tag{4.1}$$

where Σ is the mass per unit area, r is the radial distance in the disc and α is a parameter of the models. Since eccentricities are low, a particle's semi-major axis corresponds approximately to its radial position.

During the simulations, objects on orbits approaching close to the planet, interact with it and are either scattered in towards the central star or out of the system. Some test particles receive a large enough kick that they are put directly on to hyperbolic orbits, become unbound and are ejected. Others undergo a series of scattering interactions increasing their semi-major axis and/or eccentricity. Studies of comets being scattered by a single planet find that when they reach a distance of $a_{galactic}$ from the star, they are more strongly influenced by the galactic tide than the central star (Tremaine, 1993), where

$$a_{galactic} = 10^4 AU \frac{(M_{pl}/M_\oplus)^{4/3}}{(M_*/M_\odot)^{2/3} (a_{pl}/AU)}. \tag{4.2}$$

At this point they either become unbound or enter the Oort cloud. In my simulations I assume that a similar process occurs and thus any bodies that go outside of $a_{galactic}$ are classified as 'ejected' and removed from the simulation, although in reality occasionally bodies that enter the Oort cloud may return on long period orbits and re-enter the inner planetary system.

The ultimate fate of bodies scattered into the inner system, depends on the planetary system architecture. As I am considering an arbitrary planetary system, this is unknown. Observations of exo-planet systems so far suggest a diversity of architectures. The stability of an arbitrary planetary system post-main sequence is a complicated dynamical question (e.g. Debes and Sigurdsson (2002)). In this chapter the focus is on the dynamics of the planetesimal belt and not the inner planetary system and therefore I merely track particles that are scattered into the inner system, defined as a test particles scattered on to an orbit with $a < a_{in}$, where a_{in} is a parameter of the models. My working assumption is that a fraction of the bodies that are scattered in will be scattered further times by inner planets and some fraction end up close enough to the white dwarf to be

tidally disrupted. Further verification of this scattering is discussed in Chapter 5. In terms of forming the hot white dwarf discs, it is these particles that are of interest.

Test particles that have interacted with the planet, but have not, as yet, been removed I classify as being in the 'scattered disc', similar to the Kuiper belt's scattered disc. The scattered disc is defined as test particles with eccentricity higher than e_{SD}. Bodies that are in the 'scattered disc' will eventually be removed, scattered in or ejected, if the simulation were to run for sufficient time. This means that it is not necessary to run the simulations for the entire main-sequence lifetime in order to find the conditions in the belt at the start of the AGB. Although this does mean that the impact of mass loss on bodies in the scattered disc at the end of the main sequence is neglected.

This leaves us with four potential fates for test particles: scattered in (SI), ejected (EJ), in the scattered disc (SD) or left in the belt (B). In this chapter I track the number of test particles with each of these fates, for a range of simulations in which the different parameters of my model are varied. Parameters that can be changed are the number of particles, N, planet semi-major axis, a_{pl}, planet mass, M_{pl}, surface mass density defined by α, maximum eccentricity e_{max}, maximum test particle inclination, i_{max}, the radius inside of which bodies are considered to be scattered in, a_{in}, the eccentricity above which bodies are in the scattered disc, e_{SD} and the simulation time before mass loss, t_{MS}. I also consider the time evolution on the post-main sequence.

4.4 Main-Sequence evolution

4.4.1 Baseline simulation

For this simulation I consider a set-up similar to the Solar System's. A Neptune mass planet ($M_{pl} = M_{Nep}$) is placed on a circular orbit at 30AU (a_{pl}), with 500 test particles in a belt extending in semi-major axis from 30 to 47.6AU (2:1 resonance). Test particles have initial maximal eccentricities $e_{max} = 0.1$ and inclinations $i_{max} = 10°$ similar to the cold Kuiper belt. Each test particle was assigned a nominal mass after the simulation was completed based on a disc
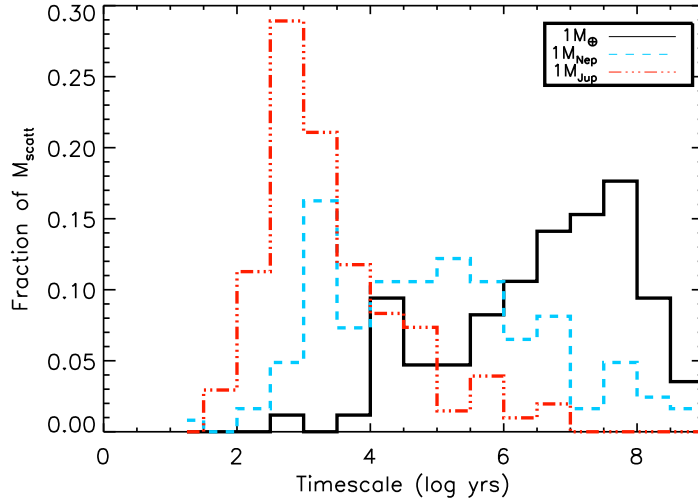
Figure 4.1 – The fraction of the total disc mass scattered in (SI) or ejected (EJ) as a function of main-sequence simulation time, for the parameters of my initial baseline simulation.

surface density profile Eq. 4.1 and $\alpha = 1.0$, taken from sub-mm observations of proto-planetary discs (e.g., Andrews and Williams (2007)). Test particles are defined as scattered into the inner system if their semi-major axis is less than a_{in}, taken to be $a_{in} = a_{pl} - 7r_H$, where $r_H = a_{pl}(M_{pl}/3M_*)^{1/3}$ is the Hill's radius, and $7r_H$ is half the separation of Neptune and Uranus in our Solar System, to the nearest number of Hill's radii.

In this section I consider this baseline simulation and the effect of changing some of the parameters from this set. Unless explicitly stated all simulations have this set of parameters. The mass that is ejected is defined as M_{EJ}, whilst M_{SI} is the mass that is 'scattered in' and M_{SD} is the mass that ends up in the scattered disc. The total mass that is scattered, $M_{scatt} = M_{EJ} + M_{SI} + M_{SD}$ and is often quoted as a fraction of the initial disc mass, M_{belt}.

4.4.2 Setting up the initial conditions in the belt

Before considering stellar mass loss, the initial conditions in the belt must be set up. This is done by running the simulation and removing all test particles that are ejected, scattered in or end the simulation in the scattered disc. The timescale on

which test particles are removed depends on planet mass; more massive planets scatter test particles on shorter timescales. I investigated the timescale on which test particles are removed, shown for several mass planets in Fig. 4.1. I found that the number of bodies removed falls off with time and therefore I chose to run my initial simulations for $t_{MS} = 10^7$ yrs, as most test particles are removed in this time period. However, it is clear from Fig. 4.1 that the $1M_\oplus$ planet continues to scatter test particles for the entire main sequence (on the order 10^9 yrs). The initial conditions in the belt will therefore depend on the main-sequence lifetime of a particular star. By only using 10^7yrs to set up the simulation, 45% of the mass that would end up being removed by a $1\mathrm{M}_\oplus$ in 10^9 yrs is missed, whilst for a $1\mathrm{M}_{Nep}$ this fraction is merely 10%. This should be taken into account when comparing the results (see later).

4.4.3 The effect of varying the definition of 'scattered in' or a_{in}

In terms of the formation of the hot white dwarf discs I am interested in the test particles that are 'scattered in', assuming that a fraction of these interact with planets in the inner system and are thus scattered on to star-grazing orbits. The fraction that are defined as 'scattered in', however, varies significantly with a_{in}.

In order to investigate the sensitivity of the results to a_{in} in Fig. 4.2 I changed the definition of a_{in} and calculated the fraction of the total mass that is defined as scattered in (SI). Only a few test particles spend time, at any point during the simulation, just inside of the planet, such that if $a_{in} > 0.98a_{pl}$ then $M_{SI} \sim 0.04M_{belt}$. These test particles will generally go on to be ejected. M_{SI} is approximately constant for definitions of a_{in} between 0.8 and 0.98. In this region test particles interact strongly with the planet and hence cover the whole range of semi-major axis space. If there are planets in the inner system, interior to $0.8a_{in}$, the dynamics of the test particles will be dominated by interior planets. This behaviour is relatively independent of planet mass or semi-major axis and I expect it to scale with the Hill's radius (r_H). The assumption of $a_{in} = a_{pl} - 7r_H$ in the baseline simulation falls in this region, hence the conclusion of these simulations will be relatively insensitive to a_{in} and if there is another planet at $\sim a_{pl} - 13r_H$
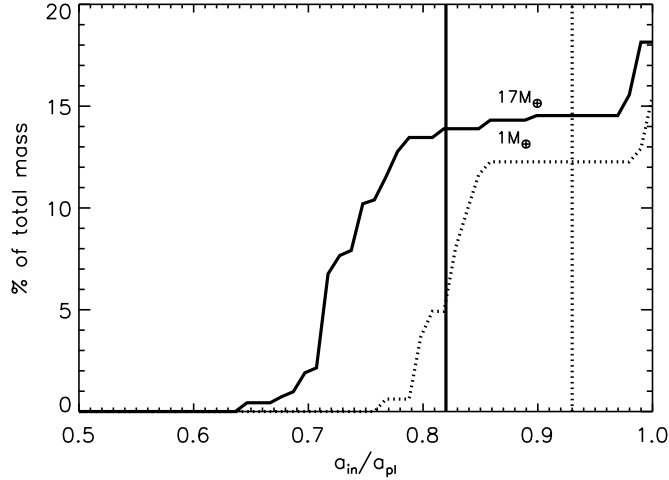
Figure 4.2 – The variation in the mass scattered in with changes to the parameter a_{in} for the initial baseline simulation (outlined in §4.4.1), with a $1M_{\oplus}$ (dotted), $1M_{Nep}$ (solid) and $e_{max} = 0.1$ and $i_{max} = 10°$. The dotted and solid vertical lines show $a_{in} = a_{pl} - 7r_H$ for $1M_{\oplus}$ and $1M_{Nep}$ respectively.

then interactions with this planet will pull some fraction of planetesimals defined as 'scattered in' into the inner region.

These simulations show a very interesting result in terms of the formation of the white dwarf discs. There is a lack of bodies scattered on to star-grazing orbits by a single planet on a circular orbit at 30AU. In fact in these simulations no test particle has a semi-major axis less than $0.5a_{pl}$. Even including the eccentricity, no test particles has a pericentre of less than $0.3a_{pl}$. In order for an asteroid to be tidally disrupted and form the observed discs, it must be scattered on to an orbit with pericentre less than the tidal radius (on the order of $R_{\odot}$). It may be that a small percentage of test particles are scattered further in towards the star, but these simulations do not find them because I have not included a sufficiently large number of test particles. Given this caveat, these simulations show that a single planet is incapable of producing the observed discs and that an inner planetary system is necessary.

4.4.4 Comparison to analytic prescription

An analytic (or semi-analytic) model is useful to understand the physical mechanisms causing instability and allows us to get scaling laws that describe the behaviour over a wide range of parameter space. Analytically it is expected that test particles orbits close to the planet will become chaotic due to the overlap of mean motion resonances. This condition defines the chaotic zone within which this occurs as (Wisdom, 1980):

$$\frac{\delta a_{chaos}}{a_{pl}} = C \left(\frac{M_{pl}}{M_*}\right)^{2/7},$$

(4.3)

where $C = 1.3$.

Test particles on chaotic orbits will either be ejected or scattered into the inner planetary system. Thus, the fraction of the disc mass that will be removed, $M_{analytic}/M_{belt}$ can be calculated, for a given surface density profile, assuming that all test particles with initial semi-major axes less than $a_{chaotic} = a_{pl} + \delta a_{chaos}$ are removed,

$$
\begin{aligned}
M_{analytic} &= \int_0^{2\pi} \int_{a_{pl}}^{a_{pl}+\delta a_{chaos}} \Sigma(r) r \, dr \, d\theta \\
&= KC\pi a_{pl} \left(\frac{M_{pl}}{M_*}\right)^{2/7}
\end{aligned}
$$

(4.4)

for the index in the surface density profile, $\alpha = 1$ and $K = M_{belt}/\pi a_{pl}(2^{2/3}-1)$, for a disc with outer edge, $a_{max} = (\frac{2}{1})^{2/3}a_{pl}$.

This can be compared to my N-body simulations, where I show that most test particles with semi-major axes less than $a_{chaotic}$ are removed, but that some test particles with $a > a_{chaotic}$ are also removed. Fig. 4.3 shows initial semi-major axis and eccentricities of all test particles in the baseline simulation, with those test particles that are scattered by a $1M_{Nep}$ planet highlighted. The higher the initial eccentricity of the test particles the higher the number of test particles outside of the chaotic zone that are removed. This also applies to inclination. No test particles were ejected in the 10^7 yrs of this simulation as this timescale is too long
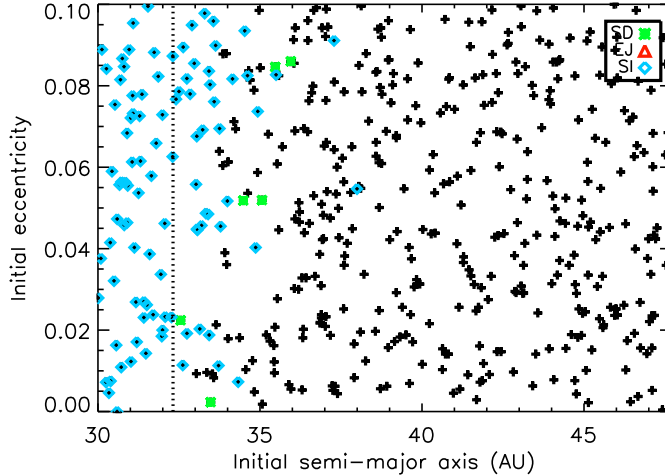
Figure 4.3 – The fates of test particles during the initial t_{MS} simulation, as a function of their initial semi-major axis and eccentricity. The parameters take the values for our baseline simulation (outlined in §4.4.1). Black particles remain in the belt, whilst red particles are ejected, blue scattered into the inner system and green end the $t_{MS} = 10^7$yrs in the scattered disc. The black dot-dashed line shows the size of the chaotic zone (Eq. 4.3), with $C = 1.3$.

for a Neptune mass planet to increase a test particles semi-major axis to greater than $a_{galactic} = 15,000$AU.

The formulation for the chaotic zone (Eq. 4.3) was developed for bodies on circular orbits. Although Quillen and Faber (2006) showed that the same formalism applies for eccentric planets, when all test particles have the forced (or the planet's) eccentricity, the behaviour for test particles with high free eccentricities (and inclinations) is different. There are a few sets of simulations that show that the chaotic zone is larger for eccentric or inclined bodies (e.g., Veras and Armitage (2004)), but there is no analytic prescription.

In order to reproduce the dependence of the chaotic zone width on particle eccentricity, this behaviour was investigated analytically using an encounter map in Mustill and Wyatt (2011a), using the formalism of Henon and Petit (1986); Duncan et al. (1989). The encounter map treats the particles as orbiting on unperturbed Keplerian orbits, except at conjunction with the planet where they receive impulsive perturbations. This is only strictly valid for $\frac{|a-a_{pl}|}{a_{pl}} \ll 1$, where a is the semi-major axis of the particle and a_{pl} is the semi-major axis of the

planet and for particle orbits that do not cross the planet's orbit $e \ll \frac{|a-a_{pl}|}{a_{pl}}$. For our simulations these approximations are valid, apart from a few particles at high eccentricities. The results of Mustill and Wyatt (2011a) are shown in Fig. 4.4. Orbits in the top left hand corner of this plot were not calculated as the approximations of the encounter map break down. Fig. 4.4 can be compared to Fig. 4.3 since it also shows the percentage of orbits that become chaotic for a range of initial eccentricities and semi-major axis. For each point on the grid in Fig. 4.4 100 orbits, with random initial longitudes of pericentre and mean longitudes, were followed. The black-white scale indicates the percentage of these that are classified as chaotic; black means that 0/100 are chaotic, whilst white means that 100% are chaotic. This plot reproduces the size of the chaotic zone for zero eccentricity particles, i.e. Eq. 4.3, although the factor C is different from the $C = 1.3$ given in Wisdom (1980). However, Fig. 4.4 shows that a greater fraction of orbits with initially higher eccentricity become chaotic for semi-major axis larger than the chaotic zone. This fits with the behaviour observed in my N-body integrations (see Fig. 4.3), the higher the initial eccentricities or inclinations, the more particles that are scattered (or end up on chaotic orbits).

4.4.5 Results

I investigated how the mass scattered by the planet on the main sequence, M_{scatt}, varies as a function of planet mass. My results are shown in Fig. 4.5 which shows the change in the total mass scattered, M_{scatt} (as a fraction of the total disc mass, M_{belt}) and a function of planet mass, for the main-sequence simulation (*i.e.* without stellar mass loss). As anticipated, there is an increase in M_{scatt}/M_{belt} with planet mass, for all simulations.

A numerical simulation with $e_{max} = 0.0$ and $i_{max} = 0.0$ is compared to an analytic prescription, assuming that all test particles inside of the chaotic zone are scattered (see Eq. 4.4). The numerical simulations scatter more mass than predicted analytically. I consider this to be partly a result of the chaotic zone being larger than predicted by Eq. 4.3, for example Chiang et al. (2009) find that $C \sim 2.0$, rather than $C \sim 1.3$, although their simulations are for a mildly eccentric planet. I also find a steeper dependence in M_{scatt} with planet mass than
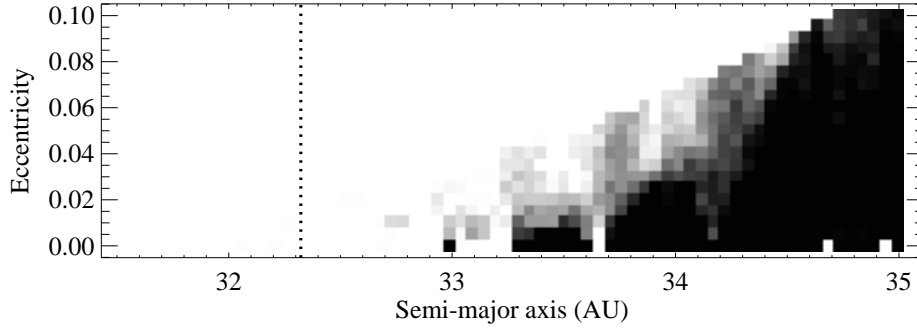
Figure 4.4 – The fraction of orbits that are chaotic are a function of initial semi-major axis and eccentricity for orbits around a $1M_{Nep}$ planet on a circular orbit at 30AU. 100 randomly selected orbits were calculated for each grid point, using an encounter map. The greyscale represents the number of orbits that become chaotic, black representing no chaotic orbits, white all 100 orbits were chaotic. The upper left hand corner of the plot has not been calculated as the encounter map is not valid in this regime. The black dot-dashed line shows the width of the chaotic zone (Eq. 4.3), with $C = 1.3$.

predicted in Eq. 4.4. I consider that this is because the simulations were run for the same time (t_{MS}), despite the fact that high mass planets scatter particles on shorter timescales. If the simulations were run for longer then the lower mass planets would scatter a higher fraction of the disc mass.

The baseline numerical simulation, with $e_{max} = 0.1$ and $i_{max} = 10.0$ is compared to a prescription calculated using the encounter map. This assumes that particles in the belt are randomly distributed in eccentricity and semi-major axis. 100 particles are placed at every grid point and using the calculation shown in Fig. 4.4, the fraction of the total disc mass in bodies not on chaotic orbits is calculated, for the given surface density profile. M_{scatt} calculated using the encounter map prescription is somewhat lower than the numerical simulations, presumably because the chaotic zone increases in size with inclination as well as eccentricity, but inclined particles were not included in the encounter map. I conclude that lower mass planets scatter a smaller fraction of the disc mass since they only scatter particles on longer timescales, as discussed above.

Analytically it is anticipated that these results are independent of a_{pl}, which

was verified by simulations, however, changing the surface density profile changes M_{scatt} by up to 15%, for $0.8 < \alpha < 2.0$.

These simulations show that there is a definite increase in M_{scatt} with initial eccentricity and inclination. Of the values of initial eccentricity and inclination tested here, the numerical simulation with $e_{max} = 0.2$ and $i_{max} = 20°$ scatters the most test particles. This implies that an analytic formulation for the chaotic zone for inclined or eccentric particles should be larger than that given in Eq. 4.3. Thus, the expected disc structure at the end of the main-sequence evolution will be the initial disc, minus material originally inside of the chaotic zone, that was scattered during the initial simulation.

4.5 Post-main sequence evolution

4.5.1 Analytic formulation

Once the orbital distribution at the end of the main sequence has been determined using the simulations of §4.4, I then studied evolution beyond the main sequence, including stellar mass loss. The star loses mass on timescales that are long compared to the orbital timescales and thus this should be an adiabatic process. Indeed this is seen to be the case for all test particles not scattered by the planet and the planet itself. As the star's mass decreases by a factor of 3, their orbital radii increase by the same factor, whilst their eccentricities and inclinations remain constant. This happens for all particles and the planet itself, although as the stellar mass decreases and the ratio of the planet's mass to the stellar mass increases, the zone of influence of the planet increases. For these simulations, where the stellar mass is decreased by a factor of 3, the size of the chaotic zone increases by a factor of $3^{2/7}$ (see Eq. 4.3). Analytically a prediction for the amount of mass scattered can be found by assuming that all test particles inside of the chaotic zone post-mass loss, but outside of its smaller pre-mass loss value, are scattered, given by:

$$M_{analytic} = \int_0^{2\pi} \int_{[a_{pl}(0)+\delta a_{chaos}(0)]}^{[a_{pl}(0)+3^{2/7}\delta a_{chaos}(0)]} \Sigma(r)rdrd\theta$$
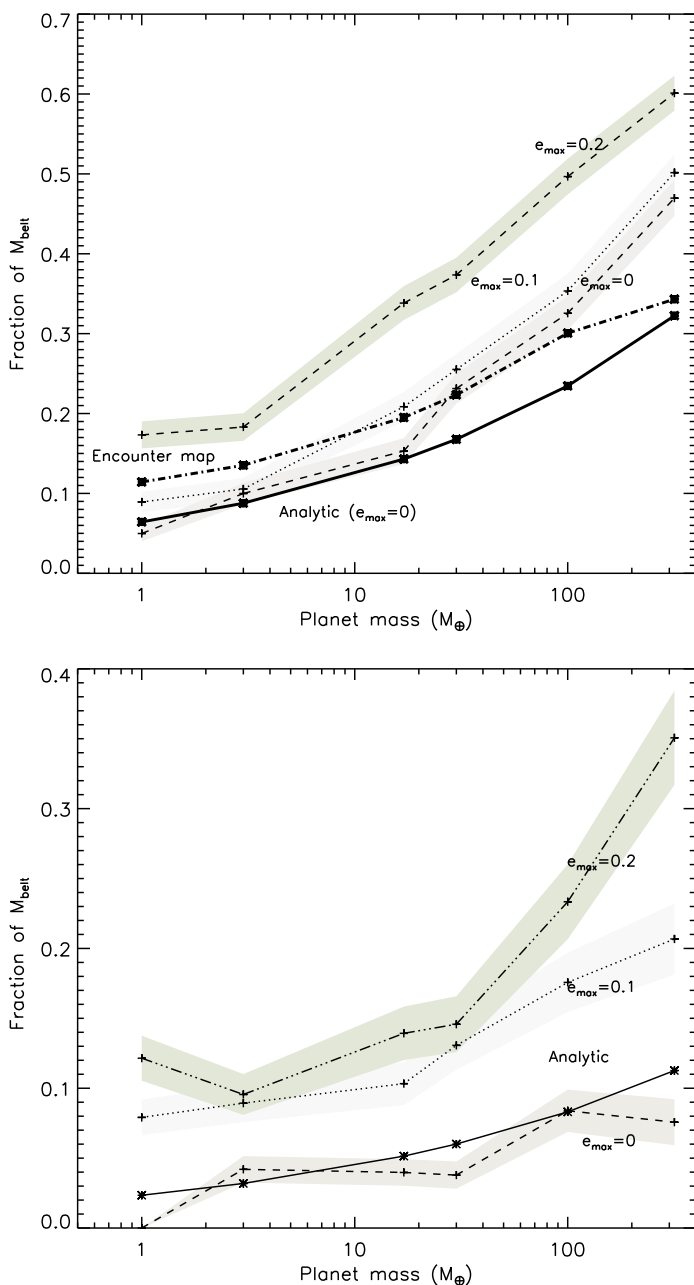
Figure 4.5 – The mass removed due to scattering by a planet as a function of planet mass. The numerical simulation with $e_{max} = 0.1$ and $i_{max} = 10.0°$ (dotted) should be compared to the encounter map calculation (dot dashed), whilst the numerical simulation with $e_{max} = 0$ and $i_{max} = 0°$ should be compared to the analytic prescription in which all material within the chaotic zone is scattered (solid). A further numerical simulation with $e_{max} = 0.2$ and $i_{max} = 20.0°$ is shown. The top plot is for the initial 10^7 yrs simulation without mass loss, whilst the bottom plot is post-stellar mass loss and 1Gyr of further evolution. The shaded areas are the 1σ error bars calculated assuming a multi-nomial distribution.

$$= K(3^{2/7} - 1)\delta a_{chaos}(0), \tag{4.5}$$

where $\delta a_{chaos}(0)$ is the initial size of the chaotic zone (Eq. 4.3), $a_{pl}(0)$ is the planet's initial semi-major axis, α is taken as 1.0 and $K = M_{belt}/\pi a_{pl}(0)(2^{2/3} - 1)$ is a constant determined from the initial belt mass.

The bottom panel of Fig. 4.5 compares the amount of mass scattered, following mass loss and 1Gyr of further evolution, found in the numerical simulations, to the analytic increase in the size of the chaotic zone. The numerical simulations show approximately the same dependence with planet mass as the analytic prescription. The simulation with $e_{max} = 0.0$ and $i_{max} = 0.0$ is closest to the analytic prescription, whilst as anticipated the simulations with higher initial eccentricities and inclinations scatter more test particles.

The main cause of scattering post stellar mass loss in these simulations is the increase in the extent of the chaotic region close to the planet. This extent can be estimated analytically from Eq. 4.3, giving Eq. 4.5, however this underestimates M_{scatt} by a factor of a few if the belt is initially dynamically hot.

4.5.2 Scattered in or ejected?

I investigated the fate of scattered bodies as a function of planet mass. This is shown in the top panel of Fig. 4.6. The analytic formulation does not give the ultimate fate of bodies, so it is necessary to use N-body simulations. The majority of the mass that is scattered by the planet ends up in the inner planetary system, according to my definition of 'scattered in'. The fraction of the mass that is ejected increases with planet mass. This is because higher mass planets give test particles a much larger kick per encounter and thus are more likely to scatter bodies out of the system after fewer encounters. Multiple encounters are, however, required to raise the test particle's eccentricity high enough that it is ejected. Assuming that the Tisserand parameter is conserved, for a test particle encountering the planet with a semi-major axis equal to the planet's and zero inclination, the condition $e > 0.405$ must be satisfied before an encounter, for that encounter to eject the particle. No test particles in my simulations start
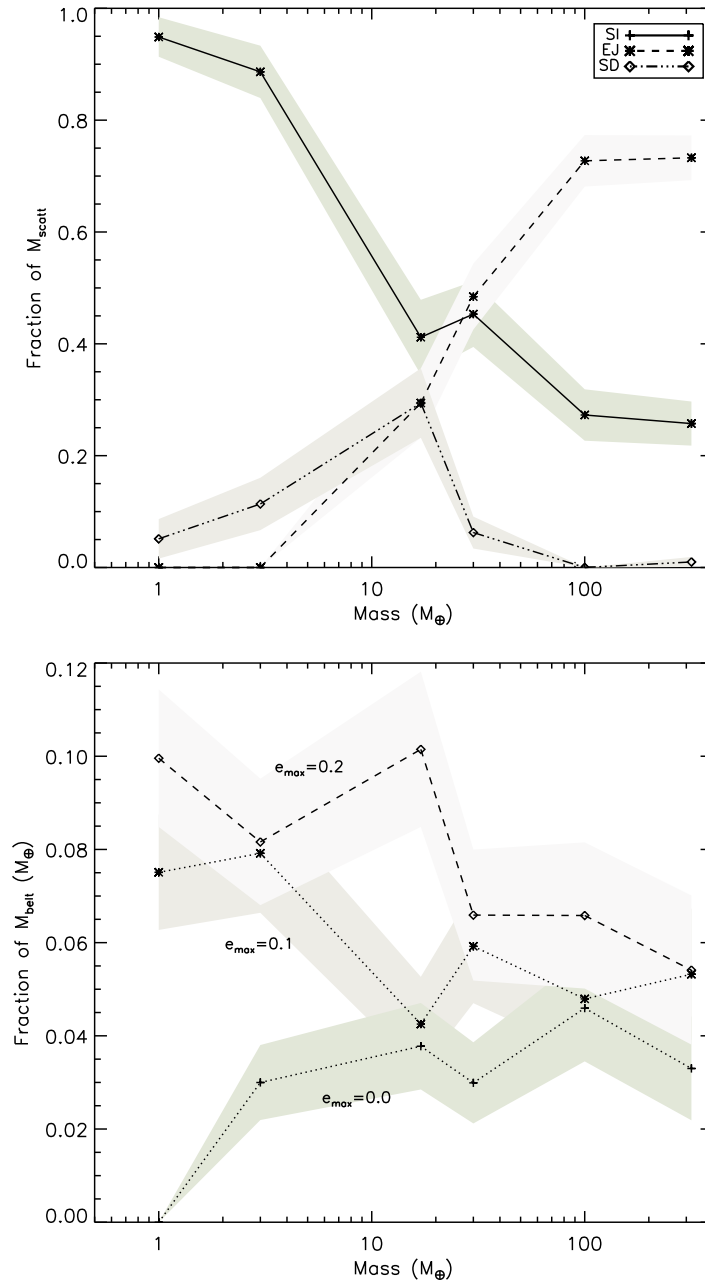
Figure 4.6 – The top panel shows M_{SI}, M_{EJ} and M_{SD} as a fraction of M_{scatt}, for various mass planets. The remainder of M_{scatt} ends the simulation in the scattered disc. The bottom shows M_{SI} as a function of planet mass for different initial eccentricities and inclinations. These figures were made after the initial main sequence evolution and 1Gyr of post-main sequence evolution. The shaded areas are the 1σ error bars calculated assuming a multi-nomial distribution.

with such a high eccentricity and hence several encounters, each of which increase the eccentricity are required before a particle is ejected.

Lower mass planets, on the other hand, tend to scatter test particles many many times before they get ejected. This leads to an increased chance of a test particle having $a < a_{in}$ at some point before it is ejected and hence in my definition being scattered in. There is a general trend that higher mass planets scatter test particles on shorter timescales and therefore clear any bodies from the scattered disc before the end of the simulation, whereas lower mass planets end the simulations with a higher mass in the scattered disc. However, the lowest mass planets scatter test particles more weakly and thus fewer test particles end up with $e > e_{SD} = 0.24$, my definition of the scattered disc and M_{SD} is low for the lowest mass planets.

Interestingly although M_{scatt} is very dependent on planet mass, the dependence with planet mass on M_{SI} is weak, at least for $e_{max} = 0.1$ and $i_{max} = 10°$; see the bottom panel of Fig. 4.6. This is because the decrease in M_{SI}/M_{scatt} with planet mass counteracts the increase in M_{scatt}. M_{SI} is highest for discs with initially high eccentricities and inclinations. This is because M_{scatt} is also higher since the size of the chaotic zone increases with eccentricity/inclination (see explanation above). Further simulations also show that M_{SI} is also independent of the planet's semi-major axis.

4.6 The relationship between these simulations and observations of metal rich white dwarfs.

In relation to the observations of metal polluted white dwarfs and/or white dwarfs with dusty discs, it is bodies that are scattered into the inner planetary system that are of interest. I assume that some fraction, f_{TD}, of the material scattered into the inner planetary system is further scattered by interior planets and ends up on an orbit that approaches close enough to the star for the body to be tidally disrupted. It is these bodies that potentially form the observed discs and accrete on to the star. This fraction is highly dependent on the inner planetary system architecture and will vary between individual planetary systems. Observations

of exo-planet systems so far suggest a diversity of architectures. The stability of an arbitrary planetary system post-main sequence is a complicated dynamical question (e.g. Debes and Sigurdsson (2002)) and it is therefore beyond the scope of the current work to investigate in detail scattering by the inner planetary system. This is discussed further in Chapter 5.

f_{TD} can be approximated for our Solar System from previous simulations. Levison and Duncan (1997) find that $\sim 1\%$ of visible comets end up on sun-grazing orbits. The particles in their simulations that leave the Kuiper belt to become visible comets correspond approximately to my definition of 'scattered in'. Levison and Duncan (1994), on the other hand, investigate the fate of known visible comets in our Solar System and find that $\sim 6\%$ end up on sun-grazing orbits. The discrepancy between the two is likely to be due to the inclusion of the terrestrial planets and comets of Oort cloud origin in Levison and Duncan (1994). Therefore, I adopt a fraction $f_{TD} = 0.06$ of M_{SI} that ends up on sun-grazing orbits and is therefore tidally disrupted. Of course, f_{TD} should be calculated for each individual planetary system and could vary between 0 and 1.

Not all of the material that is scattered in close enough to the star to be disrupted will end up in a disc, or be accreted on to the star. The formation of a such disc has not been modelled in detail at present, but here I assume that the disruption is relatively inefficient and only a small fraction, $f_{acc} \sim 0.1$, of the mass that reaches $\sim R_{\odot}$, ends up accreting on to the star. Hence, the mass that will be accreted on to the star is given by:

$$M_{acc} \sim f_{acc} \times f_{TD} \times f_{SI} \times M_{belt}, \qquad (4.6)$$

where $f_{SI} = M_{SI}/M_{belt}$ is the fraction of the initial belt mass defined as 'scattered in'. M_{SI} can either be the total mass that is scattered in, and then M_{acc} is the total mass that is accreted over the white dwarf lifetime, or alternatively the mass scattered in within a time interval dt, in which case M_{acc} is the mass accreted in the time interval dt.

Spitzer near-infrared observations of white dwarfs are used to determine dust masses for the observed discs. Since discs are opaque, this is a minimum disc mass and it is unclear how it relates to the total disc mass or the mass that

must be disrupted in order to produce such an observation. I, therefore, chose to compare the results of my simulations to the heavy element accretion rates calculated from observed abundances of metals in the white dwarf atmosphere. These are calculated from observed calcium abundances, an assumption that the accretion is in steady state and that the abundance of calcium in the accreting material is approximately solar.

Assuming that mass must be supplied to the disc at least at the rate at which it accretes on to star, the results of these simulations can be interpreted in terms of the observations. The rate at which mass is scattered inwards on to star-grazing orbits, or the predicted accretion rate, is given by:

$$\dot{M}_{acc} \sim \frac{M_{acc}}{\Delta t},\tag{4.7}$$

where Δt is the time interval over which a mass M_{acc} is scattered. This assumes that the accretion is a continuous process and that the accretion rate is determined by the scattering rate rather than viscous timescales in the close-in disc. These accretion rates could, however, be considered a minimum for the rate at which material must be supplied to the disc in order to reproduce the observed heavy element accretion rates on to the star. If the pollution is produced by the disruption of a large individual body, as suggested by, amongst others, Jura et al. (2009); Debes et al. (2011) then a lower scattering rate than predicted by these simulations is required.

Using this formulation and these assumptions, I calculated the accretion rate from each individual scattering event. The timescale for scattering, Δt in Eq. 4.7 is calculated as the mean of the time between the current scattering event and those immediately preceding and following it. For young white dwarfs ($t_{cool} <$ 1Myr) the average time between collisions is approximately 10,000 yrs. This increases to around 10Myr for old white dwarfs ($t_{cool} > $ 100Myr). Properties of the disc were selected randomly from the main-sequence population of debris discs around A stars, and the collisionally evolved mass at the end of the main sequence determined, according to the models of Wyatt et al. (2007b) and Bonsor and Wyatt (2010), presented in Chapter 3. The mass left in the disc after my initial simulations was equated with the collisionally evolved mass at the end of

the main sequence. Collisional evolution of the disc mass in the white dwarf phase is negligible (Bonsor and Wyatt, 2010). The top panel of Fig. 4.7 shows these accretion rates as a function of time, for a belt truncated by a $1M_{\oplus}$ (crosses), $1M_{Nep}$ (asterisks) and $1M_J$ (triangles) planet. Only the belt with the median mass at the end of the main sequence is displayed, whilst the arrows show the highest and lowest mass belt in the population, for the $1M_{Nep}$ case.

As anticipated, early in the white dwarf phase many particles are scattered, whilst at later times, the number of particles scattered as a function of time, and thus the accretion rate, decreases. This happens slightly more slowly for the lower mass planets, since scattering times decrease with increasing planet mass. The difference between the different planet masses, however, is small, compared to the range of accretion rates for different initial belt properties, or the other assumptions that went into this plot. In order to convert this stochastic process into a smooth decrease with time, a straight line was fitted to the data for each belt mass. These are shown for the belt with median mass by the solid ($1M_{\oplus}$), dotted ($1M_{Nep}$) and dashed ($1M_J$) lines. For a $1M_{Nep}$ planet the slope of this line is -1.1 ± 0.04. Observations from Farihi et al. (2009, 2010b) of metal polluted white dwarfs also show a decrease in accretion rate with cooling age of the white dwarf, although more recent results question the validly of this correlation (Koester et al., 2011). Using a sample of 62 white dwarfs from Farihi et al. (2009, 2010b) I found that the decrease in $\log(t_{cool})$ of $\log(\dot{M})$ can be fitted with a straight line of slope of -1.3 ± 0.23. This compares well with my simulations.

In order to compare to the observations in more detail, a model population was calculated. Each star in the population is assumed to have a $1M_{Nep}$ planet, a disc with an initial mass and radius randomly selected from the distributions of Wyatt et al. (2007b) and a randomly selected main-sequence lifetime from typical main-sequence lifetimes for A stars. Ages were selected evenly distributed in log space, as this is consistent with the spread in ages in the observed sample. The smoothed formula for the decrease in accretion rate with time shown in the top panel of Fig. 4.7 was used to calculate the accretion rates shown in the right-hand panel. Black crosses show my simulations, whilst heavy element accretion rates, calculated from observed calcium abundances (Farihi et al., 2009) are shown as red asterisks.
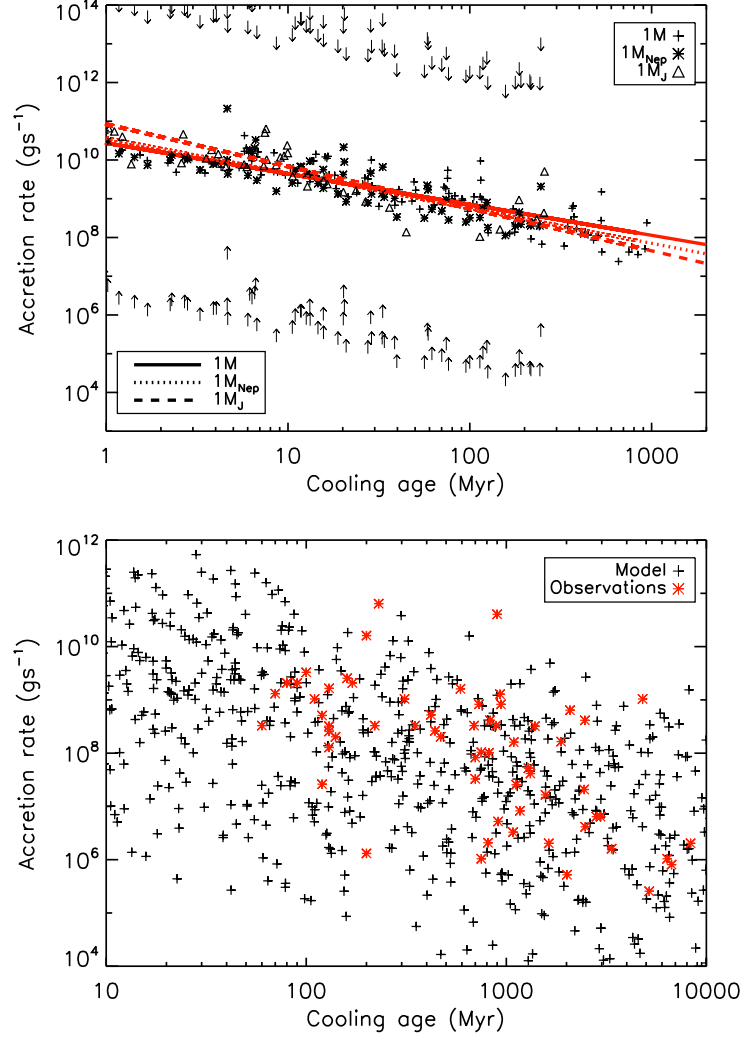
Figure 4.7 – Top panel: The accretion rate calculated using Eq. 4.6 and Eq. 4.7 for my simulations, with $M_{pl} = 1M_\oplus$ (crosses and solid line), $1M_{Nep}$ (asterisks and dotted line) and $1M_J$ (triangles and dashed line). A range of belt masses are calculated using the population models of (Bonsor and Wyatt, 2010), but only the median value is plotted here, with upper and lower limits for the $1M_{Nep}$ case shown by the arrows. Each test particle that is scattered in is plotted with a discrete value of $\dot{M}$. A straight line is then fitted to these data points.

Bottom panel: The accretion rates for a population of discs with randomly selected initial belt mass, radius, cooling age and stellar properties, using the smoothed fit to the stochastic accretion process, as determined in the top panel, but for each individual disc mass. These are compared to observed heavy element accretion rates from Farihi et al. (2009) (red asterisks).

My population agrees qualitatively with these observations, in particular, as also seen in the top panel of Fig. 4.7, there is good agreement with the decrease in accretion rate with white dwarf cooling age. There is a surprisingly good agreement with the order of magnitude and range of the observed accretion rates. My models show that accretion of material on to the star will be a continuous process and for the values of f_{TD} and f_{acc} used in these simulations it is not necessary to invoke discrete events to explain the observations.

However, my calculated accretion rates scale with the parameters f_{TD} and f_{acc}, which will vary between individual planetary systems or disruption events. The value I used for the fraction of the disrupted material accreted on to the star ($f_{acc} = 0.1$), although reasonable, may well be higher or lower and will vary with factors such as orbital parameters of the body being disrupted, its composition and strength. The largest uncertainty, however, is in the fraction of bodies 'scattered in' that end up on star-grazing orbits, f_{TD}. This will vary significantly between inner planetary system architectures. White dwarfs with high metal accretion rates that stand out from the population, such as GD362, GD40 and HS 2253+8023, most probably have a planetary system that is particularly efficient at scattering bodies on to star-grazing orbits. Other planetary systems may be less efficient at scattering bodies on to star-grazing orbits, or have this efficiency reduced post-stellar mass loss. In fact, the dynamics of many planetary systems will be altered post-stellar mass loss, potentially inner planets may be scattered such that they collide, are ejected or enter and clear the planetesimal belt. For systems where these processes are relevant, my simple model will no longer apply.

To determine the importance of further dynamical processes and whether my values for f_{TD} and f_{acc} describe an 'average' planetary system, I need to compare the percentage of white dwarfs that are metal polluted found by the observations with my simulations. Zuckerman et al. (2010) find that 19% of DB white dwarfs, with temperatures between 13,500K and 19,500K, are metal polluted with accretion rates $\dot{M} > 10^8 \mathrm{g\,s^{-1}}$. The metal pollution of DA white dwarfs in a similar temperature range is not well constrained, however for an older sample from Zuckerman et al. (2003) only 5% had accretion rates $> 10^8 \mathrm{g\,s^{-1}}$. Differences may well be attributed to a differences in the birth environments of DA and DB white dwarfs (Zuckerman et al., 2010). From my model population
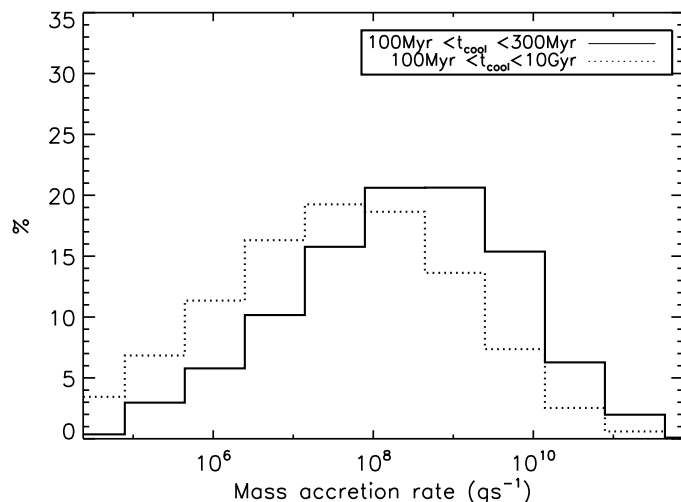
Figure 4.8 – A histogram of the predicted accretion rates from my baseline simulation, taken from the population of discs in Fig. 4.7. Discs around white dwarfs with cooling ages between 100Myr and 300Myr, and less than 10Gyr are shown.

in Fig. 4.7 I calculated a histogram of mass accretion rates, which are shown in Fig. 4.8 for two age samples, 100Myr$< t_{cool} < 300$Myr and $t_{cool} < 10$Gyr. The former sample corresponds approximately to temperatures betwen 13,500K and 19,500K and 66% of this sample have $\dot{M} > 10^8 \mathrm{g\,s^{-1}}$, compared to 45% of the stars with 100Myr$< t_{cool} < 10$Gyr.

These figures suggest that my simulations have overestimated the number of systems for which this simple model is applicable. The discrepancy could reflect the fraction of planetary systems that are destabilised post-stellar mass loss, since if a planet is scattered into the belt, the amount of material scattered may initially increase, but then decrease at later times as the belt is rapidly cleared. My simulations thus suggest that either instabilities are relevant for many planetary systems or that most planetary systems, post-stellar mass loss, are significantly less efficient than our Solar System at scattering bodies on to star-grazing orbits, i.e. $f_{TD} < 0.06$.

For many main-sequence planetary systems my model is too simplistic. It no longer applies if the planet is inclined or eccentric or if the dynamics of the system are dominated by another process, for example secular resonances or binary induced Kozai cycles. Although the evidence for planetesimal belts whose

114

inner edge is truncated by a planet is good, e.g. HR4796 (Wyatt et al., 1999; Moerchen et al., 2011), HD191089 (Churcher et al., 2010), Fomalhaut (Kalas et al., 2005; Chiang et al., 2009), other explanations have been put forward for inner holes, such as planet formation (Kenyon and Bromley, 2004b; Smith et al., 2009a) and interactions with gas (Besla and Wu, 2007). Hence, the results of these simulations may not apply to all main-sequence stars.

My simulations only consider a simplistic model for stellar mass loss. I have assumed spherical symmetry as the natural first assumption, however there have been suggestions that many systems have asymmetric mass loss e.g Soker (2001); Parriott and Alcock (1998). The stellar mass in the current simulations changed by a factor of 3, when in reality this will vary depending on the initial stellar mass, metallicity and so forth. This potentially changes the total amount of material scattered (M_{scatt}) by up to a factor of 2, thus increasing the spread in the calculated accretion rates in Fig. 4.7.

I have also ignored other effects of stellar evolution that may cause a decrease in the planetesimal belt mass, for example stellar wind drag, YORP effect or sublimation. Bonsor and Wyatt (2010) and Jura and Xu (2010) show that sublimation has a negligible effect on bodies of purely silicate or mixed composition. In Chapter 3 I found that stellar wind drag leaves between 10^{-6} and $10^{-1} M_{\oplus}$ of material inside of the planetesimal belt at the end of the AGB. These values will be reduced further by resonance trapping (Dong et al., 2010). Nonetheless, this is significantly less than the total mass scattered inwards during my simulations, between 10^{-4} and $10^{2} M_{\oplus}$, hence my simulations show that scattering by a planet will dominate over stellar wind drag.

To summarise, this simple model shows that if every star were to have a planetesimal belt truncated by a planet, and an inner planetary system capable of scattering bodies on to star-grazing orbits, this would produce the observed pollution in white dwarfs. If every system is as efficient as the Solar System at scattering bodies on to star-grazing orbits, then a higher fraction of white dwarfs would be metal polluted than is found in observations. Therefore, either many evolved planetary systems are less efficient at scattering bodies on to star-grazing orbits, or further dynamical processes are important.

4.7 Conclusions

In this chapter I addressed the origin of heavy elements in metal polluted white dwarfs and whether accretion of asteroids or comets can explain these observations. I have taken a simple model for a Kuiper-like planetesimal belt with inner edges sculpted by a planet. This is typical of many planetary systems on the main sequence. All main-sequence stars evolve to become giants, losing a significant proportion of their mass whilst on the asymptotic giant branch to end their lives as a white dwarf (or for higher mass stars than considered here, neutron star or black hole). I have used N-body simulations to investigate the effects of stellar evolution on this simple system, with the focus of explaining observations of metal polluted white dwarfs and white dwarfs with close-in dusty discs. The best models for these systems suggest that they are produced from asteroidal or cometary material that is scattered inwards due to dynamical instabilities post-stellar mass loss.

I found that for a dynamically cold system ($e_{max} = 0$ and $i_{max} = 0$), the amount of material scattered in the simulations can be calculated reasonably well using an analytic formulation, shown in Eq. 4.5. This assumes that pre-mass loss, the chaotic zone, given by Eq. 4.3, is cleared, whilst post-stellar mass loss, test particles that are inside of the increased chaotic zone are scattered. For systems with higher initial eccentricities and inclinations, for example $e_{max} = 0.1$ and $i_{max} = 10°$ for the "cold" Kuiper belt, the amount of material scattered is higher than given by this analytic formula. The fraction of the belt mass that is scattered increases with planet mass, but is independent of planet semi-major axis.

My simulations tracked test particles that are ejected, scattered in and end the simulation in the scattered disc or main belt. My definition of 'scattered in' included all test particles that are scattered on to orbits with semi-major axis less than $a_{in} = a_{pl} - 7r_H$. If there are interior planets, my assumption is that these bodies will interact with them and some fraction will be scattered on to star-grazing orbits, since my simulations show that a single planet is insufficient to scatter bodies on to star-grazing orbits. It is this fraction that is relevant to the white dwarf observations. I found that lower mass planets are more likely to

scatter test particles into the inner planetary system, whilst higher mass planets give each particle a larger 'kick' with a single close encounter and therefore are more likely to eject them. Hence, despite the increase in the amount of material scattered with planet mass, the mass that is scattered into the inner planetary system is relatively independent of planet mass, given the caveat that the belt mass is not comparable to the planet mass.

In order for my simple model to explain the white dwarf observations enough material must be scattered into the inner planetary system to reproduce the observations. I assume that a fraction $f_{acc}f_{TD}$ of the material 'scattered in' is accreted on to the star. Given the wealth of planetary system architectures found in exoplanet systems, for my calculations I take the efficiency of the Solar System at scattering Neptune encountering bodies on to sun-colliding orbits ($f_{TD} = 0.06$), and an efficiency of the disruption process of $f_{acc} = 0.1$. I assume that the initial planetesimal belt properties are the same as those found from observations of debris discs around main-sequence A stars, but take into account the collisional evolution of disc material. Accretion rates are calculated using Eq. 4.6 and Eq. 4.7 for a population of evolved planetary systems as a function of their cooling age as a white dwarf (see Fig. 4.7). These compare well with the observations, reproducing the correct order of magnitude, approximate range and most importantly the decrease in accretion rate with white dwarf age. Interestingly I find that that stellar mass loss can explain accretion rates even for old (> 1Gyr) white dwarfs.

In some ways this agreement is surprising given that the accretion rates scale with f_{TD} and hence will vary significantly between individual planetary systems. In fact my simulations overestimate the number of highly polluted white dwarfs; 82% of my simulations for white dwarfs with $t_{cool} < 300$Myr have $\dot{M} > 10^8 \, \mathrm{g\,s^{-1}}$, compared to only 19% of DB white dwarfs (Zuckerman et al., 2010) or 5% of DA white dwarfs (Zuckerman et al., 2003). There are three factors that could reduce the fraction of white dwarfs with high accretion rates calculated from my simulations. First the efficiency of scattering bodies on to star-grazing orbits may be reduced by the dynamical rearrangement of the planetary orbits. Alternatively, altered dynamics post-stellar mass loss could scatter planets in such a way that they clear the planetesimal belt swiftly of material and hence accretion will not be observed at later times. Finally, not all main-sequence stars will have a planetary

system resembling this simple model, i.e. containing a planetesimal belt and interior planet on a circular orbit.

This work shows that a simple model with a planetesimal belt and planet is able scatter enough material inwards in order to reproduce the observed metal abundances in polluted white dwarfs, even for old (>1Gyr) white dwarfs. In fact, given the observations of debris discs and planets on the main sequence, this model suggests that metals should be observed in a higher proportion of white dwarfs than is found by observations. Either the Solar System is particularly efficient at scattering bodies on to star-grazing orbits or dynamical instabilities and the rearrangement of the inner planetary system post-stellar mass loss is crucially important for many evolved planetary systems.

Chapter 5

The scattering of small bodies in planetary systems

5.1 Summary

The scattering of small bodies by planets is an important dynamical process in planetary systems. In this chapter I present an analytical model to describe this process using the simplifying assumption that each particle's dynamics is dominated by a single planet at a time. As such the scattering process can be considered as a series of three body problems during each of which the Tisserand parameter with respect to the given planet is conserved. This constrains the orbital parameter space into which the particle can be scattered. Such arguments have previously been applied to the process by which comets are scattered to the inner Solar System from the Kuiper belt. My analysis generalises this for an arbitrary planetary system. For particles scattered from an outer belt, based on the initial value of the Tisserand parameter, I find that it is possible to (i) determine which planets can eject the particles from the system, (ii) define a minimum stellar distance to which particles can be scattered, and (iii) constrain particle inclinations (and hence the disc height) at different distances. Applying this to the Solar System I determine that the planets are close to optimally separated for scattering particles between them. Concerning warm dust found around stars that also have Kuiper belt analogues, I show that, if there is to be

a dynamical link between the outer and inner regions, then certain architectures for the intervening planetary system are incapable of producing the observations. I speculate that the diversity in observed levels of warm dust may reflect the diversity of planetary system architectures. Furthermore I show that for certain planetary systems, comets can be scattered from an outer belt, or with fewer constraints, from an Oort cloud analogue, on to star-grazing orbits, in support of a planetary origin to the metal pollution and dustiness of some nearby white dwarfs. In order to make more concrete conclusions regarding scattering processes in such systems, the probability distribution for scattered particles needs to be considered.

5.2   Introduction

The scattering of small bodies is an important dynamical process in many planetary systems. One classic example is the population of small bodies close to the Sun, many of which originate further out in the Solar System, from where they were scattered inwards. Near-Earth asteroids (NEAs) originate in the asteroid belt. Many left the belt after being destabilised by resonances with Jupiter and then scattered by the terrestrial planets (Morbidelli et al., 2002). Visible comets are either objects scattered inwards from the Kuiper belt or the Oort cloud (Levison and Duncan, 1997). The scattering of small bodies has not been considered in detail for extra-solar planetary systems, mainly due to the lack of constraints on the structure of the planetary system. There is, however, evidence for small bodies in many extra-solar planetary systems, much of which has been discussed earlier in this thesis. Dust belts, known as debris discs are seen around hundreds of main-sequence stars (Wyatt, 2008). Observations, particularly resolved images, suggest that debris discs interact with planets (Greaves et al., 2005; Kalas et al., 2005; Moerchen et al., 2011), *etc* . Assuming a similar nature to our Solar System, it is reasonable to assume that scattering in these systems can also result in a comet-like population. The expected level and distribution of this comet population may differ substantially from the Solar System, depending on the individual planetary system architecture.

Evidence of such a comet-like population may exist from observations of *warm*

dust discs around a handful of main-sequence stars (Absil et al., 2006; di Folco et al., 2007; Wyatt et al., 2005; Gaidos, 1999; Beichman et al., 2005; Song et al., 2005). Comets or asteroids in the position of the observed dust belts have a short lifetime against collisions and drag forces. They cannot have existed for the entire main-sequence lifetime in their observed position (Wyatt et al., 2007a). One possible explanation is that the material originated in a cold, outer belt. It could be that we are observing a comet-like population, that is continuously replenished from scattering of material from the outer belt by intervening planets (Wyatt et al., 2007a). Alternatively, it could be a transient event, resulting from the stochastic collision of two larger bodies (Song et al., 2005), maybe in a similar manner to the impact that formed the Earth-Moon system. Or, material could be transported inwards from the outer belt during a LHB type event (Booth et al., 2009) or by drag forces (Reidemeister et al., 2011).

Another piece of evidence for the scattering of material in exo-planetary systems comes from observations of evolved stars. As discussed earlier in §1.3, observations of polluted and dusty white dwarfs are thought to originate from material scattered inwards by planets. In order to be tidally disrupted such material must not only be scattered in, as determined in Chapter 4, it must be scattered on to star-grazing orbits. The ability of evolved planetary systems to scatter comets or asteroids on to star-grazing orbits has not been investigated in detail, with previous work considering an Oort cloud origin of the scattered bodies (Debes and Sigurdsson, 2002).

In this work the scattering of small bodies in an arbitrary planetary system is investigated. N-body simulations are typically used to model such scattering (Horner and Jones, 2009; Levison and Duncan, 1997; Holman and Wisdom, 1993). A deeper understanding of the general properties of such scattering can, however, be achieved using analytical arguments, although this is generally restricted to planets on circular orbits. Simulations of scattered Kuiper belt objects have found that the scattering process can be approximated as a series of three-body problems, as the scattered bodies are passed from one planet to the next (Levison and Duncan, 1997). While such particles are under the influence of one of the planets, their dynamical evolution can be approximated by the circular restricted three-body problem in which the orbits of the particles must be such that

their Tisserand parameters, T_p, (Tisserand, 1896; Murray and Dermott, 1999) are conserved, where

$$T_p = \frac{a_p}{a} + 2\sqrt{\frac{(1 - e^2)a}{a_p}}\cos(I), \qquad (5.1)$$

where a, e, I are the comet's semi-major axis, eccentricity and inclination and a_p is the planet's semi-major axis or orbital radius.

This conservation is so fundamental to cometary dynamics that it is used to classify cometary orbits (Horner et al., 2003; Gladman et al., 2008). Simulations of scattered Kuiper belt objects have found that the Tisserand parameter is conserved *e.g.* Levison and Duncan (1997) and that the scattering process can be approximated as a series of three-body problems, as the scattered bodies are passed from one planet to the next.

In this work I use the conservation of the Tisserand parameter to constrain the orbits of scattered particles in a planetary system with an arbitrary configuration. In §5.3 I discuss how planetesimals are scattered from an outer belt, in an otherwise stable planetary system. I then outline my constraints on the orbits of particles scattered by a single planet in §5.4, which I extend to two planets in §5.5 and arbitrarily many planets in §5.6. In §5.7 I consider the application of this analysis to our Solar System, systems with *warm* dust discs and polluted white dwarfs.

5.3   Scattering of planetesimals

During the planet formation process, a planet that forms in a disc of planetesimals, will swiftly clear a zone around it, both by scattering processes and resonant interactions with the planet. Analytically the size of the planet's cleared zone can be determined using the resonance overlap criterion (Wisdom, 1980). Simulations have shown that Neptune clears such a zone in less than 10^5 yr (Levison and Duncan, 1993; Holman and Wisdom, 1993), but more generally one might expect 1,000 conjunctions for this clearing to take effect (Duncan et al., 1989). Material removed from this region may be ejected directly, whilst some fraction remains on bound, eccentric orbits, with pericentres close to the planet's orbit,

forming an analogue to Neptune's *scattered disc*. After many scatterings some of this material may reach far enough from the star to interact with the Galactic tide (Tremaine, 1993) and eventually populate an analogue of the Oort cloud.

Planetesimals outside of this chaotic zone could in principle be long term stable. However, N-body simulations of Neptune and the Kuiper belt find that Kuiper belt objects are still scattered by Neptune at late times (Holman and Wisdom, 1993; Duncan et al., 1995; Levison and Duncan, 1997; Emel'yanenko et al., 2004; Morbidelli, 1997). The Kuiper belt has a complicated structure of stable and unstable regions. The gravitational effects of Neptune and the inner planets result in the overlap of secular or mean-motion resonances producing thin chaotic regions, within the otherwise stable region (Kuchner et al., 2002; Lykawka and Mukai, 2005) and small unstable regions within otherwise stable mean motion resonances (Moons and Morbidelli, 1995; Morbidelli and Moons, 1995; Morbidelli, 1997). Objects may diffuse chaotically from stable to unstable regions (Morbidelli, 2005). This process has been shown to occur for Neptune's 3:2 and 2:1 resonances, amongst others (Morbidelli, 1997; Tiscareno and Malhotra, 2009; Nesvorný and Roig, 2000, 2001; de Elía et al., 2008). Objects leaving mean motion resonances in the Kuiper belt, in this way, may be the main source of Neptune encountering objects at the age of the solar system (Duncan et al., 1995). Many of these objects are scattered into the inner planetary system, and could be the source of Centaurs or Jupiter Family comets (Holman and Wisdom, 1993; Morbidelli, 1997; Levison and Duncan, 1997; di Sisto et al., 2010).

The dynamical processes occurring in the Kuiper belt may well be applicable to exoplanetary systems with a similar structure, *i.e.* an outer planetesimal belt and interior planets. The outer belt could be truncated by resonance overlap (Wisdom, 1980). Most particles would then inhabit a predominately stable region exterior to this, containing small regions that are unstable due to the overlap of secular or mean motion resonances of the inner planets. Objects could diffuse chaotically on long timescales from the stable to unstable regions and be scattered by the outer planet. Some of these scattered objects could enter the inner planetary system, whilst some could be ejected.

In my consideration of the dynamics of material scattered from the outer belt by interior planets, I find that this dynamics is strongly dependent on the

initial value of the Tisserand parameter, with respect to the outermost planet. Therefore, it is important to consider the value of this parameter. Object in the outer belt tend to have $T_p > 3$, whilst objects that are scattered by the planet the Tisserand parameter must be less than 3. For particles that are scattered at late times due to chaotic diffusion into an unstable region, at the time of first scattering the Tisserand parameter would be expected to be close to 3. Simulations of our solar system found this to be the case (Levison and Duncan, 1997). Here, I consider the initial value of the Tisserand parameter of such particles as an unknown, with the expectation that objects scattered in the way described will have initial Tisserand parameter values just below 3.

As a final note, I point out that not all objects scattered by Neptune originate from the cold Kuiper belt. The two other main sources are Neptune's *scattered disc* and the Oort cloud. It is possible that similar classes of objects exist in exoplanetary systems, however, there is at present no evidence for exo-Oort clouds or *scattered discs*. The distribution of the Tisserand parameter for such objects would differ significantly from those that leave the cold Kuiper belt, in particular for Oort cloud objects, where it is unconstrained and $T < 2$ is possible. Therefore, for clarity and simplicity, in this work I focus on the objects that originate in an outer belt and that are first scattered by the outermost planet, at the age of the system.

5.4 Scattering by a single planet

First I consider a system similar to that described in the previous section, with a single planet, labelled by subscript i on a circular orbit at a_i and an exterior planetesimal belt.

5.4.1 Orbital constraints

For a planetesimal with a given value of the Tisserand parameter with respect to this planet, T_i, the potential orbits on to which it can be scattered are limited, no matter how many times it interacts with the planet. The Tisserand parameter gives us no information about the probability for any given interaction to
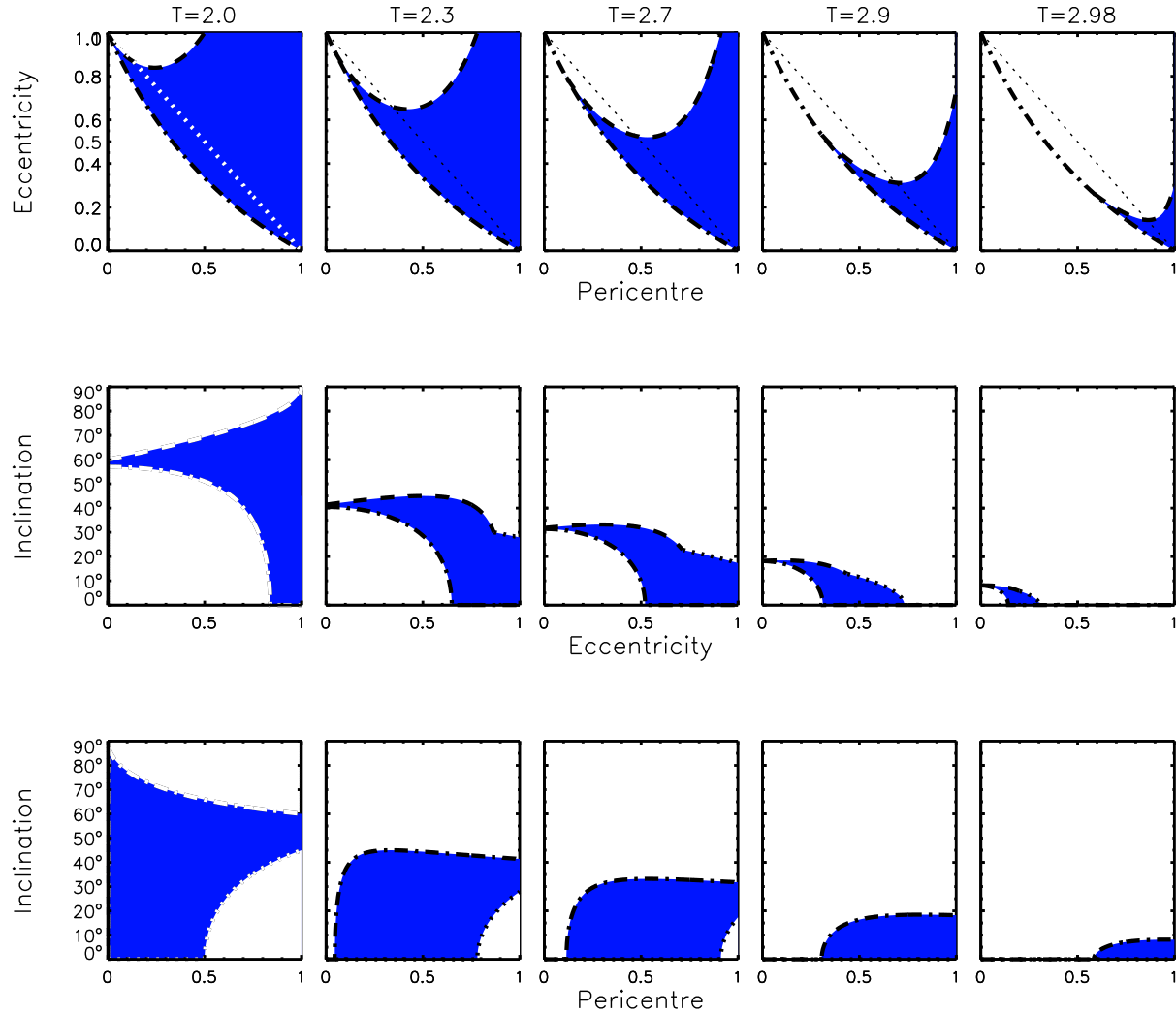
Figure 5.1 – The possible orbital parameters (coloured areas) of particles scattered by a single planet, with a given value of the Tisserand parameter with respect to that planet, T_i. This forms a 3-D parameter space, that is shown here projected on to the eccentricity-pericentre $(q - e)$ plane, the inclination-pericentre $(I - q)$ plane and the eccentricity-inclination $(e - I)$ plane. The limits of the parameter space are defined analytically in the Table 5.1, where the lines on these plots are also defined. It should be noted that the parameter space in the $q-e$ plot (top row) only extends until the lines $Q = 1$ (dot-dashed) and $\cos I = 1$ (dashed) cross and not to smaller pericentre. The units of the pericentre is the planet's semi-major axis and the dotted black line in the top row of plots shows the line where the particle's semi-major axis is equal to the planet's $(a = \frac{q}{(1-e)} = a_i)$.

Plane	Line	Constraint	Based on
q-e: upper	dashed	$e = 1 + 2q^3 - qT_i \pm 2q^{3/2}\sqrt{2 + q^3 - qT_i}$	$\cos(I) = \pm 1$
q-e: lower	dot-dashed	$e = \frac{(1-q)}{(1+q)}$	$Q = 1$
I-e: upper	dashed	$\cos(I) = \frac{T_i - 1 - e}{2\sqrt{1-e}}$	$Q = 1$
I-e: upper	dotted	$\cos(I) = \frac{T_i - 1 + e}{2\sqrt{1+e}}$	$q = 1$
I-e: lower	dot-dashed	$\cos(I) = \frac{T_i^{3/2}}{3\sqrt{3(1-e^2)}}$	$\frac{\partial I}{\partial q}\big|_{e,T_i} = 0$
I-q: upper	dot-dashed	$\cos(I) = \frac{T_i(1+q) - 2}{2\sqrt{2q(1+q)}}$	$Q = 1$
I-q: lower	dotted	$\cos(I) = \frac{T_i}{2\sqrt{2q}}$	$e = 1$

Table 5.1 – The analytical boundaries on the parameter space constraining the potential orbital parameters of a particle scattered by a planet, where the initial value of the Tisserand parameter is T_i. All units are in terms of the planet's semi-major axis; $a_i = 1$. For the cases where more than one limit is stated, the upper of the two applies and the lower limit on $I - e$ is derived from

scatter a planetesimal on to a given orbit, nor the timescales for interactions to occur. It does, however, limit the orbital parameters of the planetesimals after the interaction, in terms of its pericentre, q, eccentricity, e and the inclination, I, of its orbit with respect to the planet's. These constraints can be represented by a 3D volume in (q, e, I) space. A planetesimal, given an initial value of T_i, may not be scattered on to an orbit with parameters outside of this volume, in this simple example.

This parameter space can be fully mapped out analytically by re-writing Eq. 5.1 as

$$T_i = \frac{a_i(1 - e)}{q} + 2\sqrt{\frac{(1 + e)q}{a_i}} \cos(I), \tag{5.2}$$

and noting that if the planetesimal is to remain on a bound orbit, $0 < e < 1$, $-1 < \cos(I) < 1$ and $q > 0$ must apply. Applying these constraints to Eq. 5.2, places analytical bounds that define this 3D volume of permitted orbits. Given the difficulties in presenting a 3D volume, I instead present the 2D projection of this 3D volume on to the $q - e$ plane, $I - q$ plane and $e - I$ plane, shown in Fig. 5.1. The analytical bounds are presented in Table. 5.1.

5.4.2 Minimum pericentre

Further examination of the q-e plot in Fig. 5.1 makes clear that planetesimals cannot be scattered further towards the star than a limiting value, q_{min}, determined by T_i. This value can be calculated using constraints on the orbital parameters, apocentre $Q = a_i$ and $\cos(I) = 1$ (equivalent to the lower bound in the $q - e$ plane). For $2 < T_i < 3$:

$$\frac{q_{min}}{a_i} = \frac{-T_i^2 + 2T_i + 4 - 4\sqrt{3 - T_i}}{T_i^2 - 8}. \tag{5.3}$$

q_{min} as a function of T_i is shown in Fig. 5.2. The eccentricity at q_{min} will be given by:

$$e_{lim} = T_i - 3 + 2\sqrt{3 - T_i}. \tag{5.4}$$

For $T_i < 2$, the lines $Q = a_i$ and $\cos(I) = 1$ (positive root) no longer cross and the parameter space in the $q - e$ plane is no longer bounded by $Q = a_i$, rather by $\cos(I) = 1$ (both positive and negative root). Therefore $q_{min} \rightarrow 0$. This can be shown to be true by considering the derivatives of the lines:

$$\frac{dq}{de}\Big|_{cosI=1,q\rightarrow0} > \frac{dq}{de}\Big|_{Q=a_i,q\rightarrow0}. \tag{5.5}$$

Importantly this implies that the constraints on the pericentre that apply to the orbits of objects with $T_i > 2$ are not applicable to those with $T_i < 2$; such objects can be scattered on to orbits with any pericentre.

5.4.3 Ejection

A single planet can also eject planetesimals, given a suitable value of the Tisserand parameter. Unbound orbits (*i.e.* those with $e > 1$) are not included in the plots in Fig. 5.1. It is, however, possible to determine from the top panel of Fig. 5.1 those values of the Tisserand parameter for which the particles are constrained to bound orbits with $e < 1$. The most eccentric orbits are those with pericentre at the planet's orbit ($q = a_i$), therefore substituting into Eq. 5.1, ($q = a_i, e = 1, I = 0°$), I find that there is a limit on the Tisserand parameter such that only objects with
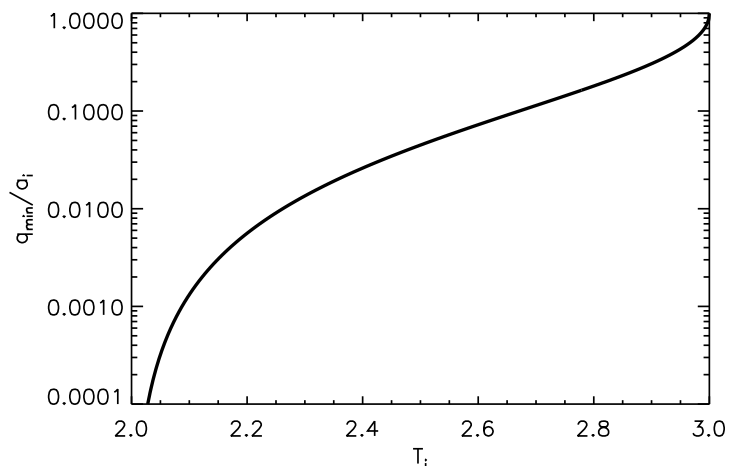
Figure 5.2 – The minimum pericentre for a test particle scattered by a single planet, as a function of the Tisserand parameter value, from Eq. 5.3. For $T_i < 2$, $q_{min} \to 0$.

$T_i < 2\sqrt{2}$ can be ejected. This has been previously calculated in, amongst others, Levison and Duncan (1997), using the formulation for the Tisserand parameter of a parabolic orbit.

5.5   Scattering by two planets

Now consider a planetary system with an outer belt and two interior planets, both on circular orbits. Particles from the outer belt are scattered by the outer planet, 1. The main possible fates of such particles are ejection, collision with a planet or the star, further scattering interactions with this planet, or scattering by the inner planet, 2. Many scattered particles are scattered multiple times by the outer planet. It dominates their dynamics for a certain period of time, during which the Tisserand parameter, with respect to this planet, T_1, is conserved. At some point, the particle may be scattered on to an orbit that overlaps with the inner planet and it may be scattered by that planet. In such an interaction the Tisserand parameter with respect to the inner planet, T_2 would be conserved, rather than T_1. Depending on the new orbit, it is then likely that the particle

is re-scattered by the inner planet and for a certain period its dynamics will be dominated by that planet.

I start by considering this simple situation where the particle is passed from planet 1 to planet 2. This is used to describe constraints on the orbits of scattered particles. I then consider the possibility that particles are scattered backwards and forwards between the two planets in §5.5.4.

5.5.1   Orbital constraints

For a particle scattered by the outer planet the Tisserand parameter, T_1, is conserved. The value of T_1 constrains the orbits, (q, e, I), of scattered particles to those shown in Fig. 5.1 that satisfy Eq. 5.1. Although only sets of the orbital parameters, q, e, I, that satisfy Eq. 5.1 are allowed, the full range of possible values is given by:

$$
\begin{aligned}
q_{min}(T_1) < \quad & q \quad < 1 \\
0 < \quad & e \quad < e_{max}(T_1) \\
0 < \quad & I \quad < I_{max}(T_1),
\end{aligned}
\tag{5.6}
$$

where q_{min} is given in Eq. 5.3,

$$
I_{max} = \cos^{-1}(\sqrt{T_1 - 2}),
\tag{5.7}
$$

and

$$
e_{max} = 3 - T_1 + 2\sqrt{3 - T_1}.
\tag{5.8}
$$

As mentioned earlier, if $T_1 > 2\sqrt{2}$, then $e_{max} > 1$ and some orbits are unbound.

The particle may interact many times with the outer planet, moving between orbits in this parameter set, until at some point it encounters the next planet, 2. Only a subset of the orbits specified by T_1 can interact with the next planet, 2. These are shown by the red filled area in Fig. 5.3 and are those orbits that cross

the planet's, with $q < a_2$ and:

$$
\begin{aligned}
q_{min}(T_1) < & \quad q \quad < a_2 \\
e_{int}(\frac{a_2}{a_1}) < & \quad e \quad < e_{lim}(T_1) \\
0 < & \quad I \quad < I_{int}(T_1, \frac{a_2}{a_1}),
\end{aligned}
\tag{5.9}
$$

where,

$$
e_{int} = \frac{a_1 + a_2}{a_1 - a_2}
\tag{5.10}
$$

and

$$
I_{int} = \cos^{-1}\left(\frac{T_1(1 + \frac{a_2}{a_1}) - 2\frac{a_2}{a_1}}{2\sqrt{2(1 + \frac{a_2}{a_1})}}\right).
\tag{5.11}
$$

I_{int} only applies if the second planet is placed inside of the maximum in q as a function of I, that occurs at $q = \frac{T_1 - 2}{4 - T_1}a_1$. Hence they apply if:

$$
\frac{a_2}{a_1} < \frac{T_1 - 2}{4 - T_1}.
\tag{5.12}
$$

Otherwise, $I < I_{max}$ (Eq. 5.7) applies.

Once the particle is scattered by planet 2, T_1 is no longer conserved, instead the value of T_2 when the particle is first scattered by planet 2 is conserved. The range of possible T_2 values is determined by the initial value of T_1 and the planets' orbits, specified by the ratio of the planet's semi-major axes, $\frac{a_2}{a_1}$.

The minimum possible value that T_2 can have occurs for particles on orbits with minimum pericentre ($q = q_{min}$), the corresponding eccentricity ($e = e_{lim}$) and in the orbital plane of the planets ($I = 0°$). It is given by:

$$
T_{2,min} = \frac{a_2(1 - e_{lim})}{q_{min}} + 2\sqrt{\frac{(1 + e_{lim})q_{min}}{a_2}},
\tag{5.13}
$$

where e_{lim} (Eq. 5.4) and q_{min} (Eq. 5.3) are functions of T_1.

Since the Tisserand parameter (T_2) is a monotonically increasing function of q, T_2 will be maximum for the orbit with the largest value of the pericentre, q,

that still crosses the planet's orbit, *i.e.* $q = a_2$. For the range of T_2 values for orbits with $q = a_2$, the minimum is at $\cos I = \pm 1$ and $e = e_X$, where from the top line of Table 5.1,

$$e_X = 1 + 2(\frac{a_2}{a_1})^3 - (\frac{a_2}{a_1})T_1 + 2(\frac{a_2}{a_1})^{3/2}\sqrt{2 + (\frac{a_2}{a_1})^3 - (\frac{a_2}{a_1})T_1}. \qquad (5.14)$$

Hence, the maximum of T_2 is given by:

$$T_{2,max} = (1 - e_X) + 2\sqrt{1 + e_X}. \qquad (5.15)$$

For the next time period the dynamics of the particle is controlled by the second planet. It may be scattered once or many times. Yet again, the particle's orbit is constrained to orbital parameters, (q, e, I), specified by the value of T_2 and Eq. 5.1. This time, however, I consider the situation where only T_1 and the planet's orbits are specified initially such that it is only known that T_2 lies between $T_{2,min}$ and $T_{2,max}$. The full range for the orbital parameters (q, e, I) is therefore specified by:

$$
\begin{aligned}
q_{min}(T_{2,min}) < \quad & q \quad < a_2 \\
0 < \quad & e \quad < e_{max}(T_{2,min}) \\
0 < \quad & I \quad < I_{max}(T_{2,min}),
\end{aligned} \qquad (5.16)
$$

where q_{min} is given by Eq. 5.3, e_{max} by Eq. 5.8 and I_{max} by Eq. 5.7, but as a function of $T_{2,min}$ rather than T_1.

5.5.2 Constraints on which particles interact with the innermost planet

For specific planetary orbits, specified by the ratio of the planets' semi-major axes, $\frac{a_2}{a_1}$, and strict constraints on the initial value of the Tisserand parameter in the outer belt (*i.e.* T_1 close to 3), the orbits of scattered particles may be constrained such that they never interact with the inner planet. This occurs
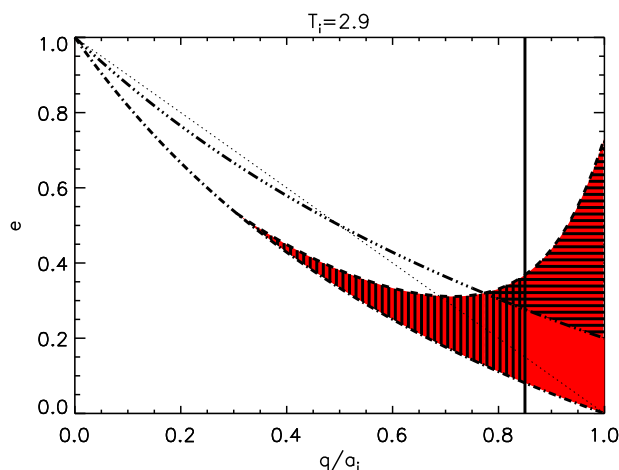
Figure 5.3 – The orbital parameter space as determined by the Tisserand param-
eter, in the eccentricity-pericentre plane, for $T_i = 2.9$ (equivalent to the fourth plot
on the top row of Fig. 5.1). The bounds on this space are between the dashed
($\cos I = 1$) and dot-dashed lines ($q = a_i$) and shown in red. The subset of this
orbital parameter space that can interact with an inner planet placed at $a_{in} = 0.8a_i$
is shown by the vertically hashed region, whilst the subset that could interact with
an outer planet placed at $a_{out} = 1.5a_i$ is shown by the horizontally hashed region.
The dotted line shows $a = a_i$, the solid line $q = a_{in}$ and the triple dotted dashed
line, $Q = a_{out}$.

when the minimum pericentre to which particles may be scattered by the outer
planet is further from the star than the inner planet's orbit:

$q_{min}(T_1) > a_2$ (Eq. 5.3) or :

$$\frac{-T_1^2 + 2T_1 + 4 - 4\sqrt{3 - T_1}}{T_1^2 - 8} > \frac{a_2}{a_1} \tag{5.17}$$

5.5.3   Minimum pericentre

In §5.4.2, Eq. 5.3, I determined the minimum pericentre to which a single planet
may scatter a particle. A similar calculation may be made for two planets, assum-
ing that particles are only passed once along the chain of planets. The minimum
pericentre will depend on the Tisserand parameter with respect to the outer
planet, T_1 and the ratio of the planets' semi-major axes, $\frac{a_2}{a_1}$.

For a particle that is scattered by the outer planet, with a value of the Tisserand parameter with respect to that planet of T_1, if it is then scattered by the inner planet, the particle could have a range of possible values of the Tisserand parameter with respect to the inner planet, between $T_{2,min}$ (Eq. 5.13) and $T_{2,max}$ (Eq. 5.15). Since q_{min} (Eq. 5.3) is a monotonically increasing function of the Tisserand parameter, the minimum pericentre for scattering by both planets will be given by $q_{min}(T_{2,min})$, where $T_{2,min}$ is the minimum value of the Tisserand parameter (Eq. 5.13). A particle scattered as far in as possible by the outer and inner planet, must be scattered on to an orbit with eccentricity $e = e_{lim}(T_{2,min})$ (Eq. 5.4) and inclination, $I = 0°$.

The minimum pericentre for a two planet system is shown in Fig. 5.4 as a function of the ratio of the planets' semi-major axes, $\frac{a_1}{a_2}$. This has a clear minimum, which occurs at:

$$a_{2,min} = \frac{(1 + e_{lim}(T_1))^{1/3} q_{min}(T_1)}{(1 - e_{lim}(T_1))^{2/3}}, \tag{5.18}$$

where e_{lim} and q_{min} are the minimum pericentre and limiting eccentricity for scattering by the outer planet, given by Eq. 5.3 and Eq. 5.8.

This means that the optimum configuration of two planets in terms of their ability to scatter particles as close to the star as possible, involves planets positioned in semi-major axis at $a_{2,min}$ and a_1. It is interesting to note that the optimum position for the inner planet is not as close to the star as the outer planet could possibly scatter particles *i.e.* $q_{min}(T_1)$, but closer to the outer planet. This is because there is a balance between moving the inner planet closer to the star, decreasing a_2, such that q_{min} is decreased directly or moving the planet further from the star, increasing a_2, but decreasing T_2 and thus q_{min}.

5.5.4 Further scattering

Scattering is not confined to the forward direction. Particles may originate in the outer belt, be scattered inwards by the outer planet, passed on to the inner planet, and then scattered back outwards again to the outer planet. Constraints on which particles might re-interact with the outer planet can be determined
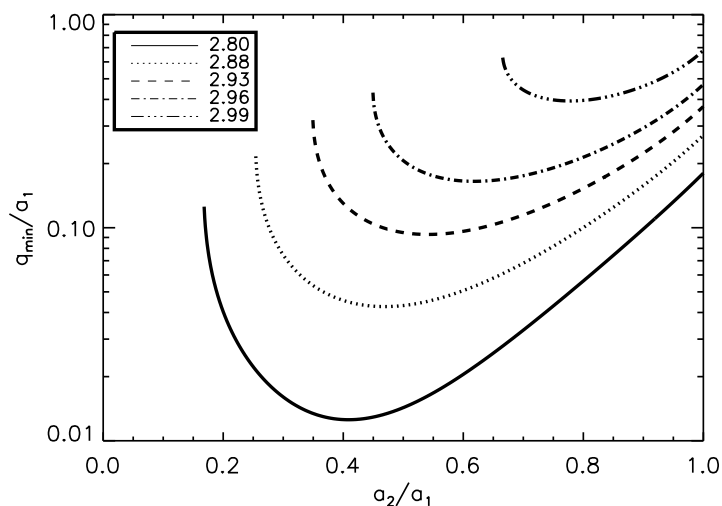
Figure 5.4 – The minimum pericentre for a test particle scattered by two planets, as a function of the ratio of the inner planet's semi-major axis to the outer planet's semi-major axis.

using a similar procedure to that discussed in the previous section (§5.5.1) for particles passed from the outer planet to the inner planet.

The possible values for the orbital parameters of particles scattered by the inner planet are determined by the value of the Tisserand parameter, T_2. A subset of these orbits cross the outer planet's orbit, those with apocentres outside of its orbit ($Q > a_1$). For the example of an outer planet at $a_1 = 1.5a_2$ and with $T_2 = 2.9$, this subset is shown by the hashed region in Fig. 5.3. Each set of orbital parameters in this region (q, e, I) will specify a possible value for the Tisserand parameter with respect to the outer planet, T_1. The minimum possible new value of T_1 occurs at the maximum pericentre ($q = a_2$), the maximum eccentricity $(e_{max}(T_2)$ Eq. 5.8) and $\cos I = 1$, such that:

$$T_{1,new,min} = \frac{a_1(T_2 - 2 - 2\sqrt{3 - T_2})}{a_2} + 2\sqrt{\frac{(4 - T_2 + 2\sqrt{3 - T_2})a_2}{a_1}}. \qquad (5.19)$$

If there are a range of values for T_2, the smallest (*e.g.* $T_{2,min}$ for Eq. 5.13) will give the lowest value of $T_{1,new,min}$. The maximum value of T_1 such that particles can still interact with the outer planet is 3, as for any scattering event.

If the particle is scattered backwards and forwards multiple times this procedure may be repeated to determine the full range of Tisserand parameter values and potential orbits. $T_{1,new,min}$ can be significantly lower than the initial value of T_1 in the outer belt, particularly after multiple scatterings backwards and forwards. Thus, this increases the range of potential orbits of scattered particles.

This can be illustrated using an example system. Consider a particle scattered by the outer planet, with $T_1 = 2.99$. The inner planet is placed arbitrarily at $a_2 = 0.7a_1$. The minimum pericentre for the particle after the particle is scattered by both planets, shown in Fig. 5.4, is $q_{min} = 0.43$. If the particle is then scattered back outwards, the minimum value of T_1 is 2.93 (Eq. 5.19). If the particle is then scattered back in, again from Fig. 5.4, this gives a new minimum pericentre for scattering by the two planets of $q_{min} = 0.12$. After a further scattering backwards and forwards, $q_{min} \rightarrow 0$; all constraints on the eccentricity and pericentre of the orbit are removed. Given sufficient repetitions this occurs for all pairs of planetary orbits, where the constraints on the Tisserand parameter allow particles to be passed between them. Thus, the orbital parameter space available to scattered particles can be greatly increased by repeatedly scattering them backwards and forwards.

So far I have merely outlined the orbital parameter space available to particles and not discussed the probability for scattering particles into this space. This is in general beyond the scope of this paper, however, these have important implications for the passing of particles backwards and forwards between the two planets. First, it is clear that the timescales for particles to be repeatedly scattered backwards and forwards between two planets will be long and therefore at any given time the probability will be higher that particles have merely been scattered by the outer planet, or passed from the outer to the inner planet once. Secondly, although repeated passing of particles between planets greatly increases the range of orbital parameters available to such scattered particles, this does not mean that it is most probable for such particles to be scattered on to more extreme (higher eccentricity or inclination) orbits. In fact, if we were to assume that a particle has an equal probability of being scattered on to any of the orbital parameters available to it, it is most likely that the particle is scattered on to an orbit that retains a value of the Tisserand parameter close to its original value.

It is only the few particles that are scattered on to *extreme* orbits, *i.e.* with low pericentre or high eccentricity/inclination, that have significantly reduced values of the Tisserand parameter when they are scattered by the next planet. Therefore, although it is possible that particles may be scattered on to extreme orbits, with low values of the Tisserand parameter, by being repeatedly passed backwards and forwards between the planets, I anticipate that the probability for this to occur is low and I therefore feel justified in focusing on particles scattered directly along a planetary system for the rest of the paper.

5.6   Multi-planet systems

All of the calculations discussed so far can be easily applied to planetary systems with many planets. The procedure discussed in §5.5.1 can be repeated many times, to determine the full range of orbital constraints and values for the Tisserand parameter after scattering by each planet. This analysis places useful constraints on the planets with which particles can interact, the planets that can eject particles and the minimum pericentre to which the whole system can scatter particles.

All of the dynamics is determined by the initial value of the Tisserand parameter with respect to the outer planet, T_1, the outer planet's semi-major axis, a_1 and the ratio of the planets' semi-major axes to one another, $\frac{a_{i+1}}{a_i}$. Scaling the system, *i.e.* changing the semi-major axes, a_i, whilst keeping their ratios, $\frac{a_{i+1}}{a_i}$, constant, will not affect the dynamics (values of T_i) and merely scales the minimum pericentre, q_{min}, with a_1. In the next section, I discuss these constraints in terms of an example planetary system.

5.6.1   A hypothetical 5-planet system with constant ratio of planets' semi-major axes

I apply these calculations to a system of 5 planets, separated by a constant ratio of adjacent planets' semi-major axis ($\frac{a_{i+1}}{a_i} = \alpha$). This corresponds to a constant number of Hill's radii for equal mass planets. My results are independent of the
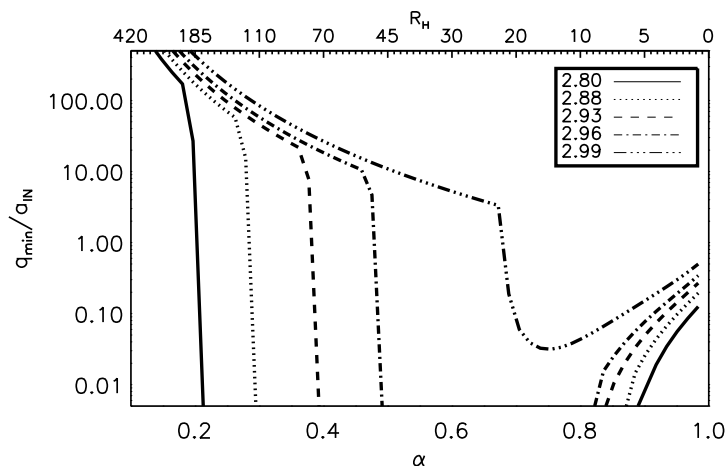
Figure 5.5 – The variation in the minimum pericentre to which test particles can be scattered to by a system of five planets. The ratio of the planets' semi-major axes (α) is constant and is given as a ratio on the bottom axis and in terms of separation in Hill's radii, for five $10\mathrm{M}_\oplus$ planets, on the top axis. The initial value of the Tisserand parameter with respect to the outer planet is varied between 2.8 and 3.0.

planet masses. I fix the inner planet at $a_5 = a_{IN}$ and calculate the semi-major axes of the other planets accordingly for a range of values for α.

The minimum pericentre to which this system can scatter particles, shown in Fig. 5.5 as a function of α, is calculated by repeatedly determining the minimum value of the Tisserand parameter for each planet. For the ith planet this occurs at $q = q_{min}(T_{i+1,min})$ (Eq. 5.3), $e = e_{lim}(T_{i+1,min})$ (Eq. 5.4) and $\cos I = 1$.

In this plot scattered particles exhibit three types of behaviour. For simplicity I label the three types of behaviour as "non-interacting", "constrained" and "unconstrained". This refers to the constraints on the orbits of scattered particles. In the "non-interacting" regime, the planets are so widely separated (small α) that particles cannot be scattered all the way along the chain of planets. The minimum pericentre to which one of the planets can scatter particles is outside of the next innermost planet's orbit. Hence the particles are restricted to the region surrounding the outer planet(s).

In the "constrained" regime, the planets are so close together (large α) that

particles can be scattered between all planets in the system. However, if they are only scattered once along the chain of planets, the Tisserand parameter cannot vary significantly from its original value and there will be a non-zero minimum pericentre to which particles can be scattered. As the separation of the planets is increased, the minimum possible value of the Tisserand parameter for each planet decreases and hence the minimum pericentre for the whole system decreases. Eventually the separation is large enough that the Tisserand parameter falls below 2 and all constraints on the minimum pericentre are removed. This forms the third, "unconstrained" regime, where there are few constraints on the orbital parameters of scattered particles.

In Fig. 5.6 the constraints on the eccentricities and inclinations of particles in the 3 regimes are shown. As particles are scattered by each planet, from the outermost (1) to the innermost (5), there will be a range of possible Tisserand parameter values, between $T_{i,min}$ (Eq. 5.13) and $T_{i,max}$ (Eq. 5.15) and hence a range of possible orbital parameters, given by Eqs. 5.16. It is the maximum inclination and eccentricity that are important on this figure, although of course the orbits of scattered particles will be distributed between the minimum and maximum values, in a manner not determined by this analysis. The plot shows that, for this example with $T_1 = 2.96$, almost all planets can eject particles ($e > 1$) and that the scale height of the disc (inclinations of scattered particles) increases with decreasing distance to the star, as the constraints on the orbits of scattered particles decrease with each successive scattering event. It is clearly seen, as anticipated, that the constraints of orbits in the "constrained" regime are much tighter than those in the "unconstrained" regime.

Although very few real planetary systems have planets separated by a constant ratio of their semi-major axes, it may be possible to similarly classify the behaviour of scattered particles into systems that fall within the three regimes and thus usefully better understand the future fate of scattered particles.

5.6.2 Hypothetical multi-planet system separated by $10R_H$

For real planetary systems the planets cannot be arbitrarily close together as dynamical instabilities are important. Chambers et al. (1996) find that planets
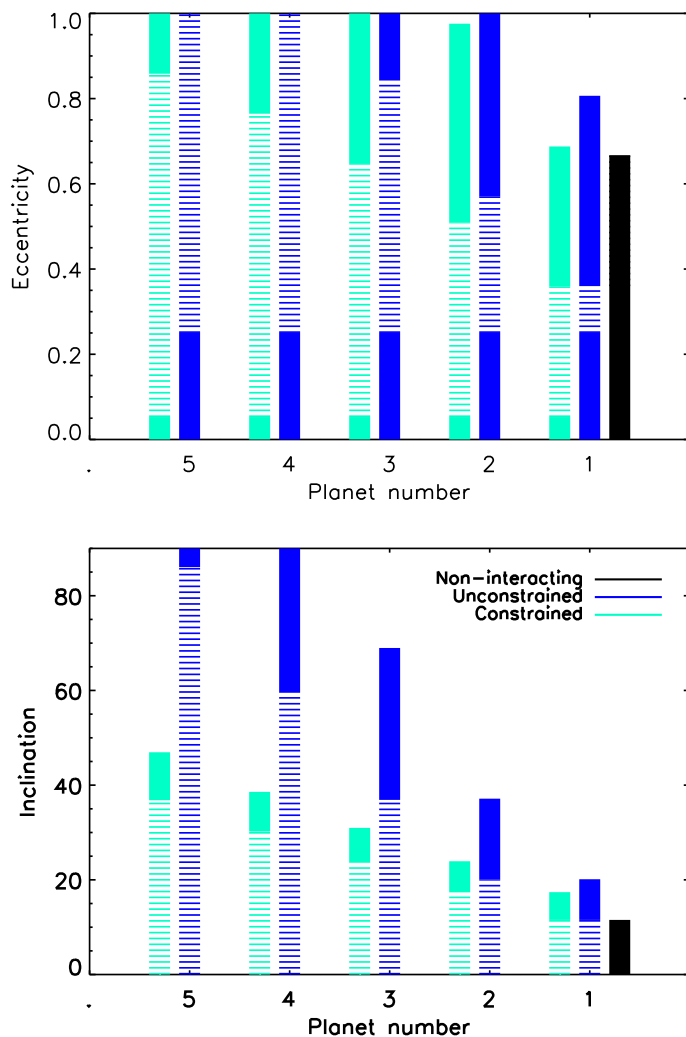
Figure 5.6 – Constraints on the eccentricities and inclinations (Eq. 5.16) of particles scattered by a system of five planets with constant ratio of the planets' semi-major axes, α, and an initial value of the Tisserand parameter in the outer belt of $T_1 = 2.96$. Particles are scattered from the belt, outside of planet 1, to the innermost planet, 5. Three planet separations are considered, corresponding to the three regimes (see discussion in the text); "non-interacting", $\alpha = 0.2$, "unconstrained", $\alpha = 0.6$ and "constrained", $\alpha = 0.9$. The dashed regions correspond to the parameters of particles that can interact with the next interior planet (Eq. 5.9).

must be separated by at least $10R_H$ to be stable. On Fig. 5.5, the separation of the planets is shown in terms of Hill's radii on the top axis, for a system of equal mass $10M_\oplus$ planets. This shows that for the $10M_\oplus$ planets considered, if they are separated by $10R_H$, then the behaviour of particles is unconstrained ($q_{min} \to 0$). Only very low mass ($< 10M_\oplus$) systems may be dynamically stable (separated by more than $10R_H$) and have limits on the scattering of particles, such that the particle's behaviour is in the "constrained" regime.

Such low mass systems are, however, unlikely to only contain 5 planets. One possible outcome of planet formation, is a chain of low mass planet embryos and an outer disc of planetesimals. Consider the example of such a disc in the position of the Solar System's Kuiper belt and a chain of interior, equal mass planets, between 1 and 30AU. If planets generally form on orbits as tightly packed as possible (Barnes and Raymond, 2004; Raymond et al., 2009), then their separation will be $\sim 10R_H$. I investigate the dynamics in such a system by varying the planet mass and thus the number of planets that fit between 1 and 30AU. This is equivalent to varying α. The results are shown in Fig. 5.7. The behaviour is identical to the five planet system in the "non-interacting" and "unconstrained" regimes, however the "constrained" regime no longer exists.

5.7 Applications to real systems

5.7.1 Solar System

This analysis can be applied to the planetary system that we understand best, our Solar System. There are three possible sources of scattered bodies; the asteroid belt, the Kuiper belt and the Oort cloud. Constraints can be placed on the potential orbital parameters of scattered bodies based on the initial value of the Tisserand parameter. The lack of tight constraints on the initial value of the Tisserand parameter limits the ability of this analysis to tightly constrain the dynamics of scattered bodies. This analysis does have the ability to explain general trends, for example behaviour seen in N-body simulations, in particular where such simulations make an implicit assumption about the Tisserand parameters of particles scattered from the Kuiper belt.
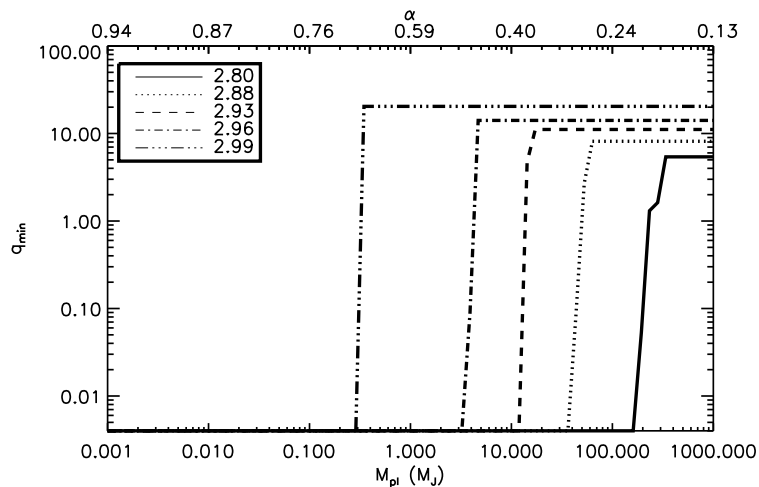
Figure 5.7 – The same as Fig. 5.5, but for tightly packed planetary systems, with equal mass planets separated by $10R_H$. The mass of the planets is shown on the bottom axis, whilst the top axis shows α. As many planets as fit between 1 and 30AU are included, hence the minimum pericentre is no longer finite for large α, a possibly more realistic scenario for low mass planets than that shown in Fig. 5.5.

As discussed in §5.3, I anticipate that the Tisserand parameter for objects scattered out of the Kuiper belt is close to 3, whereas the Tisserand parameter of scattered asteroids may take a wider range of values and that of scattered Oort cloud comets is unconstrained and many comets have $T_p < 2$. In the context of the Solar System these differences in initial conditions cannot be used to differentiate scattered particles inside of Jupiter. Even a Kuiper belt object that leaves the Kuiper belt with a high value of the Tisserand parameter (*i.e.* $T_{Nep} < 2.962$) can be scattered directly along the chain of outer planets into an unconstrained orbital parameter space inside of Jupiter ($T_J < 2$). Thus, the dynamics of such bodies are indistinguishable from scattered asteroids or Oort cloud comets, within the context of this analysis. There are, however, constraints on the orbital parameters whilst the scattered Kuiper belt object is in the Centaur region (between Neptune and Jupiter).

Given the poorly constrained and low values of the Tisserand parameter for particles leaving the asteroid belt and Oort cloud, this analysis is most usefully applied to scattered Kuiper belt objects, in the outer planet region. Particle

141

Planet	Semi-major axis (AU)	
	Observed	Optimum
Neptune	30.1	
Uranus	19.2	21.1
Saturn	9.58	10.5
Jupiter	5.20	3.3

Table 5.2 – The semi-major axes of solar system planets, compared the optimum semi-major axes in terms of scattering particles inwards, calculated using (Eq. 5.18) and $T_{Nep} = 2.98$.

inclinations are constrained to be below a maximum value, for example 80°, for scattered Kuiper belt objects with $T_{Nep} > 2.96$, consistent with observations of Centaurs (Gulbis et al., 2010). The Solar System's outer planets are well placed for scattering particles between them. If $T_{Nep} \leq 2.982$ then particles can be scattered, directly, all the way along the chain of planets to Jupiter and Table 5.2 shows that using Eq. 5.18 the planets are placed close to optimally for scattering particles as far inwards as possible. The three regimes presented in §5.6.1 can be applied to the Solar System to show that the majority of scattered Kuiper belt objects exhibit behaviour consistent with the "unconstrained" regime, if $T_{Nep} < 2.962$. Using this analysis it should be possible to identify the range of possible orbits of a scattered body, based on the manner in which it left the Kuiper belt.

5.7.2   Warm dust discs

As discussed in §5.2, there are many observations of stars with *warm* dust belts, *e.g.* (Gaidos, 1999; Beichman et al., 2005; Song et al., 2005). Many of the systems with warm dust also have cold dust belts, amongst others, η Corvi (Smith et al., 2009b; Wyatt et al., 2005), HD72905 (Beichman et al., 2006). The analysis presented here can be used to consider the scattering of particles from an outer belt inwards, as a potential explanation for the observed *warm* belts. My main conclusion is that the architecture of a planetary system determines whether or not material can be scattered to the position of the observed belt. I, therefore,

speculate that the diversity of planetary system architectures could result in the diversity of observed systems, both in terms of disc radii and the ratio of the flux from the outer to the inner belt. Although this analysis does not determine what fraction of the scattered particles end up in the position of the observed disc, it does show that some planetary systems cannot scatter particles on to the required orbits and illustrates that when the distribution of scattered particles is determined, tight constraints will be placed on the architecture of the planetary system required.

Consider the example system of η Corvi, with cold and warm dust. The inner belt is resolved and lies between 0.16-2.98 AU (Smith et al., 2009b), whilst the outer dust is at 150 ± 20 AU (Wyatt et al., 2005). Although there are no planets detected in this system, it seems probable that there is a planet close to the inner edge of the cold outer belt, that truncates it (Wyatt et al., 2005). I, therefore, consider a planet at 100AU. If the Tisserand parameter with respect to this planet is $T_1 = 2.96$, then this planet alone could potentially scatter particles in as far as 47AU (Eq. 5.3). In order for particles to be scattered inwards to the location of the warm belt, $q_{min} < 3$AU, at least three planets are required. The optimum position for these planets is 58 and 23 AU, with the outer planet at 100AU (Eq. 5.18). The orbits cannot vary significantly from these values if the minimum pericentre is to remain less than 3 AU. For example, if the planets were positioned at 100, 80 and 60 AU, particles could only be scattered in as far as 6AU and thus the warm dust belt, if it formed, would be at larger radii. Alternatively, there could be more than 3 planets, the initial value of the Tisserand parameter could be less than 2.96 or particles could be scattered multiple times backwards and forwards between the planets, as discussed in §5.5.4.

This procedure can be used for a planetary system of any architecture, observed or hypothetical, to determine whether material can be scattered from an outer belt inwards to a specific position, for example the position of an observed warm dust belt. In many cases it can usefully places limits on the minimum number of planets required if there is to be a dynamical link between the outer and inner belts.

Another use of this analysis, already calculated for the Solar System (see §5.7.1 and Table 5.2), is to consider the separation of planets in terms of their ability to

Semi-major axis (AU)		
Observed	Optimum	
	$T_p = 2.98$	$T_p = 2.7$
0.63	0.63	0.63
0.19	0.49	0.25
0.079	0.31	

Table 5.3 – The observed semi-major axes for the planets in HD 69830 (Lovis et al., 2006), compared the optimum semi-major axes in terms of scattering particles inwards, calculated using (Eq. 5.18) and a value for the Tisserand parameter with respect to the outer planet of $T_p = 2.98$ or $T_p = 2.7$.

scatter particles between them. An interesting example is HD 69830, with three planets at 0.0785, 0.186 and 0.630 AU (Lovis et al., 2006), and a warm dust disc at 0.931.16 AU (Lisse et al., 2007), outside of the exterior planet. These planets are far from optimally separated for scattering particles between them, as shown in Table 5.3. In fact unless particles have values of the Tisserand parameter with respect to the outer planet is less than 2.9, they cannot be scattered sufficiently far in that they are passed on to the next planet. It could be the warm dust belt observed results from asteroids or comets scattered inwards from an outer reservoir with $T_p > 2.9$. However, in order for this to be the case an outer belt and planet(s) would be required. Scattering by the outer planets could reduce the value of the Tisserand parameter with respect to the planet at 0.63AU of many particles, in which case further scattering by the inner planets would be possible.

5.7.3 Metal polluted white dwarfs and white dwarfs with close-in circumstellar discs

Evidence of evolved planetary systems and scattering of planetary material is found in the observations of metal polluted white dwarfs (Zuckerman et al., 2003; Koester et al., 2005) and white dwarfs with close-in circumstellar discs (Farihi et al., 2009). In order to explain these observations with planetary material, comets or asteroids must be scattered on to star-grazing orbits and tidally dis-

rupted. The analysis presented in this work can be used to determine the feasibility of this explanation.

Planets are required to scatter comets or asteroids close enough to the star. There are three potential reservoirs in an evolved planetary system, a Kuiper belt analogue, an Oort cloud analogue and if it survives an asteroid belt analogue. This analysis shows that it is possible for particles from all three reservoirs to be scattered on to star-grazing orbits, but that this ability depends strongly on the planets' orbits and the initial value of the Tisserand parameter. The lower the initial value of the Tisserand parameter, the more likely that particles can be scattered sufficiently close to the star (the lower q_{min} Fig. 5.2). Hence, the majority of comets from an Oort cloud analogue, where T_p is often less than 2, can be scattered on to star-grazing orbits, whilst for a Kuiper or asteroid belt analogue this ability is strongly dependent on the initial value of the Tisserand parameter and the planets' orbits. Asteroid belt analogues have the advantage of lower initial values for the Tisserand parameter, but the disadvantage that there may be fewer surviving interior planets and the asteroid belt itself may not survive until the white dwarf phase.

There are a large number of observations of Kuiper belt analogues around main-sequence stars (Wyatt, 2008) and models find that such systems survive the star's evolution (Bonsor and Wyatt, 2010). Such belts have been suggested as the source of the metal pollution, although there is little evidence that they are capable of scattering particles sufficiently close to the star. Here, I show that it is possible for some planetary systems to scatter particles from an outer belt on to star-grazing orbits, but that there are tight constraints on the planets' orbits and the initial value of the Tisserand parameter in the outer belt.

One potential hindrance in the ability of an evolved planetary system to scatter particles on to star-grazing orbits is the absence of inner planets due to the star's evolution. Villaver and Livio (2007) find that white dwarfs should not possess planets within 15AU due to a combination of the increased stellar radius, tidal forces and stellar mass loss. In order for a planet at $a_i = 15$AU to scatter particles on to star-grazing orbits ($q_{min} < R_\odot$), particles must have values of the Tisserand parameter less than 2.05 when they interact with the planet (Eq. 5.3). Only particles from an evolved Oort cloud might have sufficiently low values of

Tisserand parameter without interacting with further planets. Therefore, using repetition of the technique described in §5.5.1, if particles originate in an outer belt with $T_1 > 2.97$, then at least 4 planets are required to scatter particles on to star-grazing orbits, whilst for $2.89 < T_1 < 2.97$ only 3 are required. Another potential hindrance is the instability of many planetary systems after stellar mass loss on the giant branches (Debes and Sigurdsson, 2002), if, for example, planets are ejected. Examples of real planetary systems that could scatter particles on to star-grazing orbits from a Kuiper-like belt include our Solar System (if $T_{Nep} < 2.96$) and HR 8799 with planets at 14.5, 24, 38 and 68 AU (Marois et al., 2008, 2010), if $T_1 < 2.95$ in the outer belt.

This analysis crucially shows that it is possible to scatter comets or asteroids on to star-grazing orbits and places limits on the architecture of a planetary system that can do this, although it does not inform us about the probability of a given planetary system to scatter planetesimals on to star-grazing orbits. Oort cloud analogues only require a single planet to scatter material on to star-grazing orbits, whilst constraints are placed on the orbits of planets and the initial value of the Tisserand parameter required to scatter material inwards from a Kuiper or asteroid belt analogues. Thus, this analysis shows that material from an evolved Kuiper belt is a potential origin of the metal pollution in white dwarfs, although fewer constraints exist on the ability of an evolved Oort cloud to scatter comets on to star-grazing orbits. This provides important evidence in support of the planetary origin for the white dwarf observations.

5.8 Discussion of limitations

The purpose of this work is to present a simple analytical tool that can be applied to many planetary systems. It determines the potential orbital parameters of scattered particles, based on the initial value of the Tisserand parameter and the planets' orbits. It does not claim to determine the probability for any particle to be scattered on to a given orbit, nor the expected distribution of scattered particles. In order to retain this simplicity it was necessary to make several assumptions that strictly limit the applicability of this analysis. The following discussion justifies these assumptions and shows that this analysis can still be

broadly applied. I anticipate that much of the behaviour described in this work will be seen in N-body simulations of individual systems.

One of the biggest limitations in the analysis presented here, is the dependence on the initial value of the Tisserand parameter in the outer belt. This is in general an unknown quantity, although good approximations can be made to its value, as discussed in §5.3. The initial value of the Tisserand parameter can be determined in N-body simulations and hence the subsequent behaviour of scattered particles better understood.

Here, the scattering of particles by a chain of planets is considered as a series of three-body problems. This should be broadly true, although some particles may be affected by secular or resonant perturbations, or interact with a planet other than the one dominating their dynamics during that period. This could alter the value of the Tisserand parameter. Particles may also be passed backwards and forwards along the chain of planets, as discussed in §5.5.4.

Another limiting assumption is that particles only interact with the planet when their orbits exactly cross the planet's orbit. In reality there will be a zone of influence around the planet within which particle orbits may be perturbed. The size of such a zone would depend on the planet's mass. Inclusion of such a zone should not, broadly speaking, alter the outcomes of the analysis presented here.

Strictly the conservation of the Tisserand parameter, and therefore this analysis, should only be applied to systems with planets on circular orbits, *i.e.* within the context of the circular restricted three body problem. It is, however, found that even when these assumptions are relaxed, the analysis still applies approximately, for example Murray and Dermott (1999) found only a small change in the Tisserand parameter when they consider Jupiter's eccentricity. In the manner in which the analysis has been formulated here it only applies to co-planar planets. It would not be difficult to alter, for example, the calculations of §5.5 for two planets to take into account their mutual inclinations. Caution should, therefore, be exerted when applying this analysis to some of the detected exoplanets with large eccentricities and/or high relative inclinations.

All of these limitations, although important to consider, should not stop this

analysis being broadly applied and the results used to better understand the scattering of small bodies by planets.

5.9   Conclusions

I have presented an analytical tool that constrains the outcomes of scattering events, based on the conservation of the Tisserand parameter (Eq. 5.1). This tool is very useful for analysing the structure of many planetary systems where the scattering of small bodies by planets is important. It provides a simple and analytical description of the anticipated behaviour. This could be used to better understand the outcomes of N-body simulations.

I consider here the application to planetary systems where small bodies are scattered from an outer belt by interior planets. The analysis could, however, easily be reformulated to consider scattering by planets exterior to the belt. All of the outcomes depend only on the value of the Tisserand parameter, with respect to the outer planet and the orbits of the planets, with the assumption that particles are passed directly along the chain of planets. There is no dependence on the planetary mass and it is only the ratio of the planets' semi-major axes that are important. An important limit is placed on how far in particles can be scattered (q_{min} from Eq. 5.3) and I also determine which planets the particles can interact with, which can eject them and the potential height of the disc, based on the maximum particle inclinations (Eq. 5.16).

I consider the application of this analysis to our Solar System, main-sequence stars with both cold and warm dust belts and metal polluted white dwarfs. In the Solar System, this analysis describes the scattering of Kuiper belt objects by Neptune to become Centaurs and Jupiter Family comets, as well as asteroids by Mars and the terrestrial planets. I show that the Solar System planets are close to optimally separated for scattering particles between them and suggest that this analysis could be used to explain behaviour seen in N-body simulations. For main-sequence stars with *warm* dust belts that cannot have survived for the age of the system in their current positions, I show that it is possible for material to be scattered inwards from a cold, outer belt, in order to replenish such discs. Given the strong dependence on planetary system architecture, I speculate that

the diversity of such systems is a reflection of the variety of planetary system architectures.

Observations of metal polluted white dwarfs and white dwarfs with circumstellar discs have been associated with material scattered from evolved planetary systems. The best explanation for these observations is that asteroids or comets are scattered on to star-grazing orbits, tidally disrupted and accreted on to the star. I show that it is always possible for comets from an evolved Oort cloud analogue to be scattered on to star-grazing orbits. Objects can also be scattered on to star-grazing orbits from an evolved Kuiper-like outer belt, but this ability depends strongly on the planetary system architecture and the initial value of the Tisserand parameter in the outer belt. In general, multiple planets or low initial values of the Tisserand parameter are required. This strengthens the case for a planetary origin to these observations, although this analysis does not comment on the probability for particles to be scattered on to such orbits.

The intention of the analysis presented here is to describe simply and analytically the scattering of particles in a planetary system. It outlines the possible orbital parameters of scattered particles, rather than predicting their orbital distribution. This analysis is limited by a knowledge of the initial value of the Tisserand parameter and the assumption that particles are only passed directly along a chain of planets. However, as discussed in §5.8, the conclusions of this analysis should still apply to the majority of scattered particles and this analysis can, therefore, still be usefully applied to a wide range of planetary systems, in order to explain behaviour seen both in observations and N-body simulations. In summary I have presented a piece of analysis that describes the scattering of small bodies by planets. It makes use of the circular restricted three body problem and the conservation of the Tisserand parameter in order to describe several key properties of the scattering process in a manner that is applicable to a wide range of planetary systems.

Chapter 6

Conclusions

This thesis investigates the effects of stellar evolution on planetary systems. In particular, it considers debris discs observed on the main sequence, their evolution and the link between main-sequence planetary systems and observations of metal polluted white dwarfs and white dwarfs with circumstellar discs. The work presented here provides further evidence that these observations originate from evolved planetary systems.

In Chapter 3 I outlined a theoretical framework that describes the effects of stellar evolution on debris discs. I showed that debris discs should survive the star's evolution, but become increasingly difficult to detect as the star evolves. The prospects for detecting debris discs around giant stars are good and future observations of giant stars with *Herschel* or ALMA should detect such discs, thereby improving our understanding of the effects of sublimation on a debris disc. Although debris discs should survive to the white dwarf phase, they will be cold, faint and hard to detect. Young, hot white dwarfs provide the best chances of detecting a disc. This fits nicely with the observations of Su et al. (2007) and Chu et al. (2011), although my models do not directly predict these detections. Such cold, evolved debris discs could provide the reservoir of material that is scattered inwards to produce the metal pollution and close-in, circumstellar discs. For many systems, I also suggest an alternative, lower mass, reservoir: the material deposited by stellar wind drag between the inner edge of the disc and the star.

In Chapter 4 I showed that evolved debris discs provide a sufficiently large

reservoir to feed the accretion on the polluted white dwarfs, if material is scattered inwards after stellar mass loss on the giant branches. I used N-body simulations to investigate the dynamical effects of stellar mass loss on a planetary system with a cold outer belt and interior planet, similar to the Solar System's Kuiper belt and Neptune. I naturally reproduced the observed decline in accretion rates with time, as the system dynamically settles. This assumes that the accretion process is 10% efficient and that the average inner planetary system is similarly efficient at scattering material on to the star as the Solar System. I used these simulations to show that a single planet is not sufficient to scatter material on to star-grazing orbits and multiple interior planets are required.

The architecture of the inner planetary system is critical to the scattering of small bodies and whether or not they can be scattered on to star-grazing orbits. In Chapter 5, I investigated the scattering of small bodies in an arbitrary planetary system using the circular restricted three-body problem and the conservation of the Tisserand parameter. Based on the planets' orbits and the initial value of the Tisserand parameter, the full range of possible orbits for particles scattered by a chain of planets is constrained. Furthermore, I determine how far in the particles can be scattered, whether or not they can interact with all the planets and which planets can eject them. This analysis is widely applicable to any system where the scattering of small bodies is important and I also considered its application to our Solar System and main-sequence stars with warm and cold dust discs. I showed that many, but not all, planetary systems can scatter particles on to star-grazing orbits. Either low initial values of the Tisserand parameter, for example in an evolved Oort cloud analogue, or multiple planets are required.

During this thesis I have taken significant steps to show that it is plausible that the observations of metal polluted white dwarfs and white dwarfs with close-in dust discs are a result of the evolution of main-sequence planetary systems. I have not ruled out alternative explanations and there remain gaps in our knowledge and understanding.

It still remains to be shown that sufficient material will be scattered on to star-grazing orbits in a high enough proportion of planetary systems to be consistent with the observed metal pollution. This presents challenges because even on the main sequence the diversity of planetary system architectures is not well

characterised. Within the context of the analysis presented in Chapter 5, the probability distribution for scattering outcomes can be determined and from this the probability for particles to be scattered on to star-grazing orbits calculated. This probability distribution can either be calculated using N-body simulations for the scattering of many test particles, or analytically by considering collisional probabilities and the outcome of collisions, calculated analytically as a change in orbital parameters, based on the relative velocity and direction of the collision. From the probability distribution for the orbits of particles scattered by a planet, this could be extended to multiple planets and thus the radial distribution of particles scattered by a chain of planets also be calculated. This would be very useful for explaining observations of the scattering process in many planetary systems, in particular main-sequence stars with both warm and cold dust belts.

There are other pathways for transporting material from an outer planetary system on to the star to be investigated. These include resonant perturbations that produce high eccentricities in an asteroid-like belt, as suggested in the Falling Evaporating Body (FEB) scenario for β Pic (Beust and Morbidelli, 1996) and for asteroids falling on to the Sun (Farinella et al., 1994), Kozai-type oscillations, stellar wind drag or the effects of a binary companion. Alternative explanations for the observations involve features of stellar evolution and include the merger of two white dwarfs (García-Berro et al., 2007).

In order to produce the observations, material must not only be transported inwards, but it must be tidally disrupted and accreted on to the star. Further detailed modelling of this process is required to better understand the observations and link with outer planetary systems. It is not clear how their disruption leads to the formation of a circular disc that accretes on to the star. The disruption could be modelled using SPH simulations. It is important to determine what fraction of material is accreted on to the star and the structure of the accretion flow. It may be that differences in the disruption process lead to geometrically different discs, which may help to explain the lack of observed excess emission around some highly polluted white dwarfs, whilst other weakly polluted dwarfs have strong emission. This may also provide an explanation for the presence of gaseous discs in some systems. Further observations of a large sample of white dwarfs that characterise the level of metal pollution and the incidence of circum-

stellar discs is necessary to aid our understanding of the link between the two. This should be achieved with WISE and further HST, *Herschel*, Gemini, *etc*, observations.

The ultimate goal is to provide a definitive link between evolved planetary systems and these observations by the detection of an outer planetary system around a polluted white dwarf. This may be possible in the near future. There are many searches for planets around white dwarfs, such as DODO (Burleigh et al., 2008), Gaia (Silvotti et al., 2011a) *etc* , although these are generally biased towards close-in planets and do not focus on polluted white dwarfs. If there is an outer planetesimal belt that is sufficiently massive it may be possible to detect it with ALMA or *Herschel*. Such a detection would provide good evidence in support of the hypothesis that the pollution of the white dwarfs is planetary in origin. In any case *Herschel* will be used to follow up observations of cold dust discs around very young white dwarfs made by Chu et al. (2011). These should provide important confirmation of the nature of these observations, planetary or otherwise.

At present investigations of planetary systems beyond the main sequence naturally focus on the current observations. These include the growing number of detections of planets around giant stars and extreme horizontal branch stars, as well as the white dwarf observations. As the number and diversity of these observations grows, as does the need for more detailed theoretical models that evolve main-sequence planetary systems and link them with the observations around evolved stars. Overall, there are very good future prospects for improving our theoretical and observational knowledge of evolved planetary systems. In this thesis I have advanced our understanding of the link between main-sequence planetary systems and observations of evolved stars, in particular metal polluted white dwarfs and white dwarfs with circumstellar discs, paving the way for future work on the post-main sequence evolution of planetary systems.

Bibliography

Aannestad, P. A., Kenyon, S. J., Hammond, G. L., and Sion, E. M.: 1993, Cool metallic-line white dwarfs, radial velocities, and interstellar accretion, *AJ* **105**, 1033 16

Absil, O., di Folco, E., Mérand, A., Augereau, J.-C., Coudé du Foresto, V., Aufdenberg, J. P., Kervella, P., Ridgway, S. T., Berger, D. H., ten Brummelaar, T. A., Sturmann, J., Sturmann, L., Turner, N. H., and McAlister, H. A.: 2006, Circumstellar material in the ¡astrobj¿vega¡/astrobj¿ inner system revealed by chara/fluor, *A&A* **452**, 237 121

Alcock, C., Fristrom, C. C., and Siegelman, R.: 1986, On the number of comets around other single stars, *ApJ* **302**, 462 18

Allen, R. L., Bernstein, G. M., and Malhotra, R.: 2001, The edge of the solar system, *ApJ* **549**, L241 94

Andrews, S. M. and Williams, J. P.: 2005, Circumstellar dust disks in taurus-auriga: The submillimeter perspective, *ApJ* **631**, 1134 54

Andrews, S. M. and Williams, J. P.: 2007, High-resolution submillimeter constraints on circumstellar disk structure, *ApJ* **659**, 705 97

Assef, R. J., Gaudi, B. S., and Stanek, K. Z.: 2009, Detecting transits of planetary companions to giant stars, *ApJ* **701**, 1616 8

Augereau, J.-C. and Beust, H.: 2006, On the au microscopii debris disk. density profiles, grain properties, and dust dynamics, *A&A* **455**, 987 41

Augereau, J. C., Nelson, R. P., Lagrange, A. M., Papaloizou, J. C. B., and Mouillet, D.: 2001, Dynamical modeling of large scale asymmetries in the beta pictoris dust disk, *A&A* **370**, 447 5, 42

Aumann, H. H., Beichman, C. A., Gillett, F. C., de Jong, T., Houck, J. R., Low, F. J., Neugebauer, G., Walker, R. G., and Wesselius, P. R.: 1984, Discovery of a shell around alpha lyrae, *ApJ* **278**, L23 5

Backer, D. C., Foster, R. S., and Sallmen, S.: 1993, A second companion of the millisecond pulsar 1620 - 26, *Nature* **365**, 817 12

Barnes, R. and Raymond, S. N.: 2004, Predicting planets in known extrasolar planetary systems. i. test particle simulations, *ApJ* **617**, 569 140

Becklin, E. E., Farihi, J., Jura, M., Song, I., Weinberger, A. J., and Zuckerman, B.: 2005, A dusty disk around gd 362, a white dwarf with a uniquely high photospheric metal abundance, *ApJ* **632**, L119 19, 20

Beichman, C. A., Bryden, G., Gautier, T. N., Stapelfeldt, K. R., Werner, M. W., Misselt, K., Rieke, G., Stansberry, J., and Trilling, D.: 2005, An excess due to small grains around the nearby k0 v star hd 69830: Asteroid or cometary debris?, *ApJ* **626**, 1061 5, 121, 142

Beichman, C. A., Tanner, A., Bryden, G., Stapelfeldt, K. R., Werner, M. W., Rieke, G. H., Trilling, D. E., Lawler, S., and Gautier, T. N.: 2006, Irs spectra of solar-type stars: A search for asteroid belt analogs, *ApJ* **639**, 1166 142

Benz, W. and Asphaug, E.: 1999, Catastrophic disruptions revisited, *Icarus* **142**, 5 35, 36

Besla, G. and Wu, Y.: 2007, Formation of narrow dust rings in circumstellar debris disks, *ApJ* **655**, 528 115

Beuermann, K., Buhlmann, J., Diese, J., Dreizler, S., Hessman, F. V., Husser, T., Miller, G. F., Nickol, N., Pons, R., Ruhr, D., Schmülling, H., Schwope, A. D., Sorge, T., Ulrichs, L., Winget, D. E., and Winget, K. I.: 2011, The giant planet orbiting the cataclysmic binary dp leonis, *A&A* **526**, A53+ 13

Beuermann, K., Hessman, F. V., Dreizler, S., Marsh, T. R., Parsons, S. G., Winget, D. E., Miller, G. F., Schreiber, M. R., Kley, W., Dhillon, V. S., Littlefair, S. P., Copperwheat, C. M., and Hermes, J. J.: 2010, Two planets orbiting the recently formed post-common envelope binary nn serpentis, *A&A* **521**, L60+ 13

Beust, H. and Morbidelli, A.: 1996, Mean-motion resonances as a source for infalling comets toward beta pictoris, *Icarus* **120**, 358 153

Blum, J.: 2010, Dust growth in protoplanetary disks - a comprehensive experimental/theoretical approach, *Research in Astronomy and Astrophysics* **10**, 1199 34

Bonsor, A., Mustill, A. J., and Wyatt, M. C.: 2011, Dynamical effects of stellar mass-loss on a kuiper-like belt, *MNRAS* **414**, 930 iii

Bonsor, A. and Wyatt, M.: 2010, Post-main-sequence evolution of a star debris discs, *MNRAS* **409**, 1631 110, 111, 112, 115, 145

Booth, M., Wyatt, M. C., Morbidelli, A., Moro-Martín, A., and Levison, H. F.: 2009, The history of the solar system's debris disc: observable properties of the kuiper belt, *MNRAS* **399**, 385 121

Boyle, C. B.: 1984, Mass transfer and accretion in close binaries - a review, *Vistas in Astronomy* **27**, 149 13

Brinkworth, C. S., Gänsicke, B. T., Marsh, T. R., Hoard, D. W., and Tappert, C.: 2009, A dusty component to the gaseous debris disk around the white dwarf sdss j1228+1040, *ApJ* **696**, 1402 20

Bujarrabal, V., Castro-Carrizo, A., Alcolea, J., and Neri, R.: 2005, The orbiting gas disk in the red rectangle, *A&A* **441**, 1031 14

Bujarrabal, V., van Winckel, H., Neri, R., Alcolea, J., Castro-Carrizo, A., and Deroo, P.: 2007, The nebula around the post-agb star 89 herculis, *A&A* **468**, L45 14

Burleigh, M. R., Clarke, F. J., Hogan, E., Brinkworth, C. S., Bergeron, P., Dufour, P., Dobbie, P. D., Levan, A. J., Hodgkin, S. T., Hoard, D. W., and Wachter, S.: 2008, The 'dodo' survey - i. limits on ultra-cool substellar and planetary-mass companions to van maanen's star (vma2), *MNRAS* **386**, L5 12, 154

Burns, J. A., Lamy, P. L., and Soter, S.: 1979, Radiation forces on small particles in the solar system, *Icarus* **40**, 1 39, 40, 67

Campo Bagatin, A., Cellino, A., Davis, D. R., Farinella, P., and Paolicchi, P.: 1994, Wavy size distributions for collisional systems with a small-size cutoff, *Planet. Space Sci.* **42**, 1079 39

Chambers, J. E.: 1999, A hybrid symplectic integrator that permits close encounters between massive bodies, *MNRAS* **304**, 793 25, 94

Chambers, J. E.: 2009, Planetary migration: What does it mean for planet formation?, *Annual Review of Earth and Planetary Sciences* **37**, 321 28

Chambers, J. E., Wetherill, G. W., and Boss, A. P.: 1996, The stability of multi-planet systems, *Icarus* **119**, 261 31, 138

Chayer, P. and Dupuis, J.: 2010, Effect of radiative levitation on calculations of accretion rates in white dwarfs, *American Institute of Physics Conference Series* **1273**, 394 16

Chayer, P., Fontaine, G., and Wesemael, F.: 1995, Radiative levitation in hot white dwarfs: Equilibrium theory, *ApJS* **99**, 189 16

Chiang, E., Kite, E., Kalas, P., Graham, J. R., and Clampin, M.: 2009, Fomalhaut's debris disk and planet: Constraining the mass of fomalhaut b from disk morphology, *ApJ* **693**, 734 5, 42, 93, 102, 115

Chu, Y., Su, K. Y. L., Bilikova, J., Gruendl, R. A., De Marco, O., Guerrero, M. A., Updike, A. C., Volk, K., and Rauch, T.: 2011, Spitzer 24 um survey for dust disks around hot white dwarfs, *AJaccepted* 15, 16, 86, 151, 154

Churcher, L., Wyatt, M., and Smith, R.: 2010, Resolved imaging of the hd191089 debris disc, *MNRAS* pp 1405—+ 42, 115

de Elía, G. C., Brunini, A., and di Sisto, R. P.: 2008, Collisional and dynamical evolution of plutinos, *A&A* **490**, 835 123

de Ruyter, S., van Winckel, H., Maas, T., Lloyd Evans, T., Waters, L. B. F. M., and Dejonghe, H.: 2006, Keplerian discs around post-agb stars: a common phenomenon?, *A&A* **448**, 641 14

Debes, J., Stark, K., and Walsh, M.: 2011, *in prep* 110

Debes, J. H. and Sigurdsson, S.: 2002, Are there unstable planetary systems around white dwarfs?, *ApJ* **572**, 556 10, 17, 18, 31, 92, 93, 95, 109, 121, 146

Dermott, S. F., Jayaraman, S., Xu, Y. L., Gustafson, B. Å. S., and Liou, J. C.: 1994, A circumsolar ring of asteroidal dust in resonant lock with the earth, *Nature* **369**, 719 28

Desidera, S. and Barbieri, M.: 2007, Properties of planets in binary systems. the role of binary separation, *A&A* **462**, 345 11

di Folco, E., Absil, O., Augereau, J.-C., Mérand, A., Coudé du Foresto, V., Thévenin, F., Defrère, D., Kervella, P., ten Brummelaar, T. A., McAlister, H. A., Ridgway, S. T., Sturmann, J., Sturmann, L., and Turner, N. H.: 2007, A near-infrared interferometric survey of debris disk stars. i. probing the hot dust content around ϵ eridani and τ ceti with chara/fluor, *A&A* **475**, 243 121

di Sisto, R. P., Brunini, A., and de Elía, G. C.: 2010, Dynamical evolution of escaped plutinos, another source of centaurs, *A&A* **519**, A112+ 123

Dohnanyi, J. S.: 1969, Collisional model of asteroids and their debris, *J. Geophys. Res.* **74**, 2531 34

Döllinger, M. P., Hatzes, A. P., Pasquini, L., Guenther, E. W., Hartmann, M., Girardi, L., and Esposito, M.: 2007, Discovery of a planet around the k giant star 4 ursae majoris, *A&A* **472**, 649 8

Dong, R., Wang, Y., Lin, D. N. C., and Liu, X.: 2010, Dusty disks around white dwarfs. i. origin of debris disks, *ApJ* **715**, 1036 16, 28, 47, 69, 86, 115

Duncan, M., Quinn, T., and Tremaine, S.: 1989, The long-term evolution of orbits in the solar system - a mapping approach, *Icarus* **82**, 402 101, 122

Duncan, M. J., Levison, H. F., and Budd, S. M.: 1995, The dynamical structure of the kuiper belt, *AJ* **110**, 3073 123

Dupuis, J., Fontaine, G., Pelletier, C., and Wesemael, F.: 1992, A study of metal abundance patterns in cool white dwarfs. i - time-dependent calculations of gravitational settling, *ApJS* **82**, 505 16

Dupuis, J., Fontaine, G., Pelletier, C., and Wesemael, F.: 1993, A study of metal abundance patterns in cool white dwarfs. ii - simulations of accretion episodes, *ApJS* **84**, 73 16

Duquennoy, A. and Mayor, M.: 1991, Multiplicity among solar-type stars in the solar neighbourhood. ii - distribution of the orbital elements in an unbiased sample, *A&A* **248**, 485 12

Emel'yanenko, V. V., Asher, D. J., and Bailey, M. E.: 2004, High-eccentricity trans-neptunian objects as a source of jupiter-family comets, *MNRAS* **350**, 161 123

Everhart, E.: 1985, An efficient integrator that uses gauss-radau spacings, *Dynamics of Comets: Their Origin and Evolution, Proceedings of IAU Colloq. 83, held in Rome, Italy, June 11-15, 1984.* pp 185–+ 25

Faedi, F., West, R. G., Burleigh, M. R., Goad, M. R., and Hebb, L.: 2011, Detection limits for close eclipsing and transiting substellar and planetary companions to white dwarfs in the wasp survey, *MNRAS* **410**, 899 12

Farihi, J., Barstow, M. A., Redfield, S., Dufour, P., and Hambly, N. C.: 2010a, Rocky planetesimals as the origin of metals in dz stars, *MNRAS* **404**, 2123 16, 92

Farihi, J., Dufour, P., Napiwotzki, R., and Koester, D.: 2011, The magnetic and metallic degenerate g77-50, *MNRAS* **413**, 2559 93

Farihi, J., Jura, M., Lee, J., and Zuckerman, B.: 2010b, Strengthening the case for asteroidal accretion: Evidence for subtle and diverse disks at white dwarfs, *ApJ* **714**, 1386 18, 20, 92, 111

Farihi, J., Jura, M., and Zuckerman, B.: 2009, Infrared signatures of disrupted minor planets at white dwarfs, *ApJ* **694**, 805 17, 18, 19, 47, 69, 86, 92, 111, 112, 144

Farihi, J., Zuckerman, B., and Becklin, E. E.: 2008, Spitzer irac observations of white dwarfs. i. warm dust at metal-rich degenerates, *ApJ* **674**, 431 87

Farinella, P., Froeschlé, C., Froeschlé, C., Gonczi, R., Hahn, G., Morbidelli, A., and Valsecchi, G. B.: 1994, Asteroids falling into the sun, *Nature* **371**, 314 153

Gaidos, E. J.: 1999, Observational constraints on late heavy bombardment episodes around young solar analogs, *ApJ* **510**, L131 121, 142

Galland, F., Lagrange, A., Udry, S., Chelli, A., Pepe, F., Queloz, D., Beuzit, J., and Mayor, M.: 2005, Extrasolar planets and brown dwarfs around a-f type stars. i. performances of radial velocity measurements, first analyses of variations, *A&A* **443**, 337 8

Gänsicke, B. T.: 2011, Gaseous debris disks around white dwarfs, **1331**, 211 21

Gänsicke, B. T., Koester, D., Marsh, T. R., Rebassa-Mansergas, A., and Southworth, J.: 2008, Sdssj084539.17+225728.0: the first dbz white dwarf with a metal-rich gaseous debris disc, *MNRAS* **391**, L103 21

Gänsicke, B. T., Marsh, T. R., and Southworth, J.: 2007, Sdssj104341.53+085558.2: a second white dwarf with a gaseous debris disc, *MNRAS* **380**, L35 21

Gänsicke, B. T., Marsh, T. R., Southworth, J., and Rebassa-Mansergas, A.: 2006, A gaseous metal disk around a white dwarf, *Science* **314**, 1908 18, 20, 92

García-Berro, E., Lorén-Aguilar, P., Pedemonte, A. G., Isern, J., Bergeron, P., Dufour, P., and Brassard, P.: 2007, Evidence of a merger of binary white dwarfs: The case of gd 362, *ApJ* **661**, L179 153

Geier, S., Edelmann, H., Heber, U., and Morales-Rueda, L.: 2009, Discovery of a close substellar companion to the hot subdwarf star hd 149382. the decisive influence of substellar objects on late stellar evolution, *ApJ* **702**, L96 8, 10

Geier, S., Heber, U., Tillich, A., Hirsch, H., Kupfer, T., Schaffenroth, V., Classen, L., Maxted, P. F. L., Østensen, R. H., Barlow, B. N., Marsh, T. R., Gänsicke, B. T., Napiwotzki, R., O'Toole, S. J., and Günther, E. W.: 2011, Substellar companions and the formation of hot subdwarf stars, *American Institute of Physics Conference Series* **1331**, 163 10

Gielen, C., van Winckel, H., Min, M., Waters, L. B. F. M., and Lloyd Evans, T.: 2008, Spitzer survey of dust grain processing in stable discs around binary post-agb stars, *A&A* **490**, 725 14

Gladman, B., Marsden, B. G., and Vanlaerhoven, C.: 2008, Nomenclature in the outer solar system, *The Solar System Beyond Neptune* pp 43–57 122

Greaves, J. S., Holland, W. S., Wyatt, M. C., Dent, W. R. F., Robson, E. I., Coulson, I. M., Jenness, T., Moriarty-Schieven, G. H., Davis, G. R., Butner, H. M., Gear, W. K., Dominik, C., and Walker, H. J.: 2005, Structure in the ϵ eridani debris disk, *ApJ* **619**, L187 120

Gulbis, A. A. S., Elliot, J. L., Adams, E. R., Benecchi, S. D., Buie, M. W., Trilling, D. E., and Wasserman, L. H.: 2010, Unbiased inclination distributions for objects in the kuiper belt, *AJ* **140**, 350 142

Hadjidemetriou, J. D.: 1963, Two-body problem with variable mass: A new approach, *Icarus* **2**, 440 30

Haghighipour, N.: 2009, Formation, dynamical evolution, and habitability of planets in binary star systems, *Exoplanets: Detection, Formation, Properties, Habitability. Editor: John Mason (Springer, 2008)* 13, 23

Heber, U.: 2008, Extreme horizontal branch stars, *Mem. Soc. Astron. Italiana* **79**, 375 10

Heber, U.: 2009, Hot subdwarf stars, *ARA&A* **47**, 211 9

Henon, M. and Petit, J.: 1986, Series expansion for encounter-type solutions of hill's problem, *Celestial Mechanics* **38**, 67 101

Holman, M. J. and Wisdom, J.: 1993, Dynamical stability in the outer solar system and the delivery of short period comets, *AJ* **105**, 1987 121, 122, 123

Horner, J., Evans, N. W., Bailey, M. E., and Asher, D. J.: 2003, The populations of comet-like bodies in the solar system, *MNRAS* **343**, 1057 122

Horner, J. and Jones, B. W.: 2009, Jupiter - friend or foe? ii: the centaurs, *International Journal of Astrobiology* **8**, 75 121

Hurley, J. R., Pols, O. R., and Tout, C. A.: 2000, Comprehensive analytic formulae for stellar evolution as a function of mass and metallicity, *MNRAS* **315**, 543 6, 7, 48, 50, 51

Jacobs, V. A., Østensen, R. H., van Winckel, H., Bloemen, S., Pápics, P. I., Raskin, G., Debosscher, J., Uttenthaler, S., van Aarle, E., Waelkens, C., Bauwens, E., Verhoelst, T., Gielen, C., Lehmann, H., and Oreiro, R.: 2011, in . U. H. S. Schuh, H. Drechsel (ed.), *American Institute of Physics Conference Series*, Vol. 1331 of *American Institute of Physics Conference Series*, pp 304–309 10

Johnson, J. A., Fischer, D. A., Marcy, G. W., Wright, J. T., Driscoll, P., Butler, R. P., Hekker, S., Reffert, S., and Vogt, S. S.: 2007, Retired a stars and their companions: Exoplanets orbiting three intermediate-mass subgiants, *ApJ* **665**, 785 8

Johnson, J. A., Marcy, G. W., Fischer, D. A., Wright, J. T., Reffert, S., Kregenow, J. M., Williams, P. K. G., and Peek, K. M. G.: 2008, Retired a stars and their companions. ii. jovian planets orbiting κ crb and hd 167042, *ApJ* **675**, 784 8

Jones, M. I., Jenkins, J. S., and Rojo, P.: 2011, Study of planetary systems around giant stars, *American Institute of Physics Conference Series* **1331**, 310 8

Jura, M.: 1990, The absence of circumstellar dust debris around g giants, *ApJ* **365**, 317 81, 82

Jura, M.: 1999, Dust around first-ascent red giants, *ApJ* **515**, 706 46

Jura, M.: 2003, A tidally disrupted asteroid around the white dwarf g29-38, *ApJ* **584**, L91 18, 19, 92

Jura, M.: 2004, Other kuiper belts, *ApJ* **603**, 729 47, 71

Jura, M.: 2008, Pollution of single white dwarfs by accretion of many small asteroids, *AJ* **135**, 1785 47, 69, 93

Jura, M., Farihi, J., Zuckerman, B., and Becklin, E. E.: 2007, Infrared emission from the dusty disk orbiting gd 362, an externally polluted white dwarf, *AJ* **133**, 1927 19

Jura, M., Muno, M. P., Farihi, J., and Zuckerman, B.: 2009, X-ray and infrared observations of two externally polluted white dwarfs, *ApJ* **699**, 1473 87, 110

Jura, M. and Xu, S.: 2010, The survival of water within extrasolar minor planets, *AJ* **140**, 1129 71, 115

Kains, N., Wyatt, M. C., and Greaves, J. S.: 2011, Steady-state evolution of debris discs around solar-type stars, *MNRAS* **414**, 2486 34

Kalas, P., Graham, J. R., Chiang, E., Fitzgerald, M. P., Clampin, M., Kite, E. S., Stapelfeldt, K., Marois, C., and Krist, J.: 2008, Optical images of an exosolar planet 25 light-years from earth, *Science* **322**, 1345 5

Kalas, P., Graham, J. R., and Clampin, M.: 2005, A planetary system as the origin of structure in fomalhaut's dust belt, *Nature* **435**, 1067 5, 115, 120

Kennedy, G. M. and Wyatt, M. C.: 2010, Are debris discs self-stirred?, *MNRAS* **405**, 1253 46

Kenyon, S. J. and Bromley, B. C.: 2004a, Collisional cascades in planetesimal disks. ii. embedded planets, *AJ* **127**, 513 34

Kenyon, S. J. and Bromley, B. C.: 2004b, Detecting the dusty debris of terrestrial planet formation, *ApJ* **602**, L133 46, 115

Kenyon, S. J. and Bromley, B. C.: 2004c, The size distribution of kuiper belt objects, *AJ* **128**, 1916 35

Kilic, M., von Hippel, T., Leggett, S. K., and Winget, D. E.: 2006, Debris disks around white dwarfs: The daz connection, *ApJ* **646**, 474 18, 92

Kim, S. S., Zuckerman, B., and Silverstone, M.: 2001a, Extent of excess far-infrared emission around luminosity class iii stars, *ApJ* **550**, 1000 15

Kim, S. S., Zuckerman, B., and Silverstone, M.: 2001b, Extent of excess far-infrared emission around luminosity class iii stars, *ApJ* **550**, 1000 46, 82

Klein, B., Jura, M., Koester, D., Zuckerman, B., and Melis, C.: 2010, Chemical abundances in the externally polluted white dwarf gd 40: Evidence of a rocky extrasolar minor planet, *ApJ* **709**, 950 17, 92

Koester, D., Girven, J., Gänsicke, B. T., and Dufour, P.: 2011, Cool dz white dwarfs in the sdss, *A&A* **530**, A114+ 18, 111

Koester, D., Rollenhagen, K., Napiwotzki, R., Voss, B., Christlieb, N., Homeier, D., and Reimers, D.: 2005, Daz white dwarfs in the spy sample, *14th European Workshop on White Dwarfs, Astronomical Society of the Pacific Conference Series* **334**, 215 144

Koester, D. and Wilken, D.: 2006, The accretion-diffusion scenario for metals in cool white dwarfs, *A&A* **453**, 1051 16

Krivov, A. V.: 2010, Debris disks: seeing dust, thinking of planetesimals and planets, *Research in Astronomy and Astrophysics* **10**, 383 42

Krivov, A. V., Löhne, T., and Sremčević, M.: 2006, Dust distributions in debris disks: effects of gravity, radiation pressure and collisions, *A&A* **455**, 509 39

Krivov, A. V., Mann, I., and Krivova, N. A.: 2000, Size distributions of dust in circumstellar debris discs, *A&A* **362**, 1127 43

Krivov, A. V., Müller, S., Löhne, T., and Mutschke, H.: 2008, Collisional and thermal emission models of debris disks: Toward planetesimal population properties, *ApJ* **687**, 608 46

Krivov, A. V., Reidemeister, M., Fiedler, S., Löhne, T., and Neuhäuser, R.: 2011, Debris disc candidates in systems with transiting planets, *MNRAS* pp L322+ 3

Krivov, A. V., Sremčević, M., and Spahn, F.: 2005, Evolution of a keplerian disk of colliding and fragmenting particles: a kinetic model with application to the edgeworth kuiper belt, *Icarus* **174**, 105 43

Kuchner, M. J., Brown, M. E., and Holman, M.: 2002, Long-term dynamics and the orbital inclinations of the classical kuiper belt objects, *AJ* **124**, 1221 123

Kudritzki, R. P. and Reimers, D.: 1978, On the absolute scale of mass-loss in red giants. ii. circumstellar absorption lines in the spectrum of alpha sco b and mass-loss of alpha sco a., *A&A* **70**, 227 xv, 11, 51

Kunitomo, M., Ikoma, M., Sato, B., Katsuta, Y., and Ida, S.: 2011, Planet engulfment by $\tilde{1}$.5-3 solar-mass red giants, *ApJ* submitted 9

Kurucz, R. L.: 1979, Model atmospheres for g, f, a, b, and o stars, *ApJS* **40**, 1 48

Lagrange, A., Beust, H., Udry, S., Chauvin, G., and Mayor, M.: 2006, New constrains on gliese 86 b. vlt near infrared coronographic imaging survey of planetary hosts, *A&A* **459**, 955 13

Lagrange, A., Desort, M., Galland, F., Udry, S., and Mayor, M.: 2009, Extrasolar planets and brown dwarfs around a-f type stars. vi. high precision rv survey of early type dwarfs with harps, *A&A* **495**, 335 8

Lee, J. W., Kim, S.-L., Kim, C.-H., Koch, R. H., Lee, C.-U., Kim, H.-I., and Park, J.-H.: 2009, The sdb+m eclipsing system hw virginis and its circumbinary planets, *AJ* **137**, 3181 10

Levison, H. F. and Duncan, M. J.: 1993, The gravitational sculpting of the kuiper belt, *ApJ* **406**, L35 122

Levison, H. F. and Duncan, M. J.: 1994, The long-term dynamical behavior of short-period comets, *Icarus* **108**, 18 109

Levison, H. F. and Duncan, M. J.: 1997, From the kuiper belt to jupiter-family comets: The spatial distribution of ecliptic comets, *Icarus* **127**, 13 109, 120, 121, 122, 123, 124, 128

Li, A. and Greenberg, J. M.: 1997, A unified model of interstellar dust., *A&A* **323**, 566 33, 53

Lisse, C. M., Beichman, C. A., Bryden, G., and Wyatt, M. C.: 2007, On the nature of the dust in the debris disk around hd 69830, *ApJ* **658**, 584 144

Livio, M. and Soker, N.: 1984, Star-planet systems as possible progenitors of cataclysmic binaries, *MNRAS* **208**, 763 8

Löhne, T., Krivov, A. V., and Rodmann, J.: 2008, Long-term collisional evolution of debris disks, *ApJ* **673**, 1123 52

Lovis, C. and Mayor, M.: 2007, Planets around evolved intermediate-mass stars. i. two substellar companions in the open clusters ngc 2423 and ngc 4349, *A&A* **472**, 657 8

Lovis, C., Mayor, M., Pepe, F., Alibert, Y., Benz, W., Bouchy, F., Correia, A. C. M., Laskar, J., Mordasini, C., Queloz, D., Santos, N. C., Udry, S., Bertaux, J., and Sivan, J.: 2006, An extrasolar planetary system with three neptune-mass planets, *Nature* **441**, 305 5, 144

Lykawka, P. S. and Mukai, T.: 2005, Long term dynamical evolution and classification of classical tnos, *Earth Moon and Planets* **97**, 107 123

Mann, I., Nakamura, A. M., Mukai, T., and I. Mann, A. M. Nakamura, . T. M.: 2009, Small bodies in planetary systems, *Lecture Notes in Physics, Berlin Springer Verlag* 758 38, 40

Marois, C., Macintosh, B., Barman, T., Zuckerman, B., Song, I., Patience, J., Lafrenière, D., and Doyon, R.: 2008, Direct imaging of multiple planets orbiting the star hr 8799, *Science* **322**, 1348 5, 146

Marois, C., Zuckerman, B., Konopacky, Q. M., Macintosh, B., and Barman, T.: 2010, Images of a fourth planet orbiting hr 8799, *Nature* **468**, 1080 146

Maxted, P. f. L., Heber, U., Marsh, T. R., and North, R. C.: 2001, The binary fraction of extreme horizontal branch stars, *MNRAS* **326**, 1391 9

Melis, C., Jura, M., Albert, L., Klein, B., and Zuckerman, B.: 2010, Echoes of a decaying planetary system: The gaseous and dusty disks surrounding three white dwarfs, *ApJ* **722**, 1078 18, 21, 92

Mestel, L.: 1952, On the theory of white dwarf stars. i. the energy sources of white dwarfs, *MNRAS* **112**, 583 50

Metcalfe, T. S., Montgomery, M. H., and Kanaan, A.: 2004, Testing white dwarf crystallization theory with asteroseismology of the massive pulsating da star bpm 37093, *ApJ* **605**, L133 50

Moerchen, M. M., Churcher, L. J., Telesco, C. M., Wyatt, M., Fisher, R. S., and Packham, C.: 2011, Asymmetric heating of the hr 4796a dust ring due to pericenter glow, *A&A* **526**, A34+ 42, 115, 120

Moons, M. and Morbidelli, A.: 1995, Secular resonances inside mean-motion commensurabilities: the 4/1, 3/1, 5/2 and 7/3 cases., *Icarus* **114**, 33 123

Morbidelli, A.: 1997, Chaotic diffusion and the origin of comets from the 2/3 resonance in the kuiper belt, *Icarus* **127**, 1 28, 123

Morbidelli, A.: 2002, Modern integrations of solar system dynamics, *Annual Review of Earth and Planetary Sciences* **30**, 89 25

Morbidelli, A.: 2005, Origin and dynamical evolution of comets and their reservoirs, *arXiv:astro-ph/0512256* 123

Morbidelli, A., Bottke, Jr., W. F., Froeschlé, C., and Michel, P.: 2002, Origin and evolution of near-earth objects, *Asteroids III* pp 409–422 120

Morbidelli, A. and Moons, M.: 1995, Numerical evidence on the chaotic nature of the 3/1 mean motion commensurability, *Icarus* **115**, 60 123

Mullally, F., Reach, W. T., De Gennaro, S., and Burrows, A.: 2009, Spitzer planet limits around the pulsating white dwarf gd66, *ApJ* **694**, 327 11

Mullally, F., Winget, D. E., De Gennaro, S., Jeffery, E., Thompson, S. E., Chandler, D., and Kepler, S. O.: 2008, Limits on planets around pulsating white dwarf stars, *ApJ* **676**, 573 11

Müller, S., Löhne, T., and Krivov, A. V.: 2010, The debris disk of vega: A steady-state collisional cascade, naturally, *ApJ* **708**, 1728 39

Murray, C. D. and Dermott, S. F.: 1999, *Solar system dynamics* 25, 26, 122, 147

Mustill, A. J. and Wyatt, M. C.: 2009, Debris disc stirring by secular perturbations from giant planets, *MNRAS* **399**, 1403 34, 46

Mustill, A. J. and Wyatt, M. C.: 2011a, Dependence of a planet's chaotic zone on particle eccentricity: the shape of debris disc inner edges, *ArXiv e-prints* 101, 102

Mustill, A. J. and Wyatt, M. C.: 2011b, A general model of resonance capture in planetary systems: first- and second-order resonances, *MNRAS* **413**, 554 28

Nesvorný, D., Ferraz-Mello, S., Holman, M., and Morbidelli, A.: 2002, Regular and chaotic dynamics in the mean-motion resonances: Implications for the structure and evolution of the asteroid belt, *Asteroids III* pp 379–394 28

Nesvorný, D. and Roig, F.: 2000, Mean motion resonances in the trans-neptunian region i. the 2:3 resonance with neptune, *Icarus* **148**, 282 123

Nesvorný, D. and Roig, F.: 2001, Mean motion resonances in the transneptunian region part ii: The 1 : 2, 3 : 4, and weaker resonances, *Icarus* **150**, 104 123

Olofsson, H., Maercker, M., Eriksson, K., Gustafsson, B., and Schöier, F.: 2010, High-resolution hst/acs images of detached shells around carbon stars, *A&A* **515**, A27+ 46

O'Toole, S., Heber, U., Geier, S., Classen, L., and De Marco, O.: 2011, Radial velocity search for substellar companions to sdb stars, *American Institute of Physics Conference Series* **1331**, 170 10

Parriott, J. and Alcock, C.: 1998, On the number of comets around white dwarf stars: Orbit survival during the late stages of stellar evolution, *ApJ* **501**, 357 115

Perets, H. B.: 2010, Second generation planets, *ApJ* submitted 13, 14

Phillips, N. M., Greaves, J. S., Dent, W. R. F., Matthews, B. C., Holland, W. S., Wyatt, M. C., and Sibthorpe, B.: 2010, Target selection for the suns and debris surveys for debris discs in the solar neighbourhood, *MNRAS* **403**, 1089 78, 81, 84, 85, 86

Plavchan, P., Jura, M., and Lipscy, S. J.: 2005, Where are the m dwarf disks older than 10 million years?, *ApJ* **631**, 1161 41

Plavchan, P., Werner, M. W., Chen, C. H., Stapelfeldt, K. R., Su, K. Y. L., Stauffer, J. R., and Song, I.: 2009, New debris disks around young, low-mass stars discovered with the spitzer space telescope, *ApJ* **698**, 1068 64

Plets, H. and Vynckier, C.: 1999, An analysis of the incidence of the vega phenomenon among main-sequence and post main-sequence stars, *A&A* **343**, 496 14

Podsiadlowski, P.: 1993, in . S. R. K. J. A. Phillips, S. E. Thorsett (ed.), *Planets Around Pulsars*, Vol. 36 of *Astronomical Society of the Pacific Conference Series*, pp 149–165 12

Poglitsch, A. and Waelkens, C.: 2010, The photodetector array camera and spectrometer (pacs) on the herschel space observatory, *A&A* **518**, L2+ 72

Qian, S.-B., Liu, L., Liao, W.-P., Li, L.-J., Zhu, L.-Y., Dai, Z.-B., He, J.-J., Zhao, E.-G., Zhang, J., and Li, K.: 2011, Detection of a planetary system orbiting the eclipsing polar hu aqr, *MNRAS* **414**, L16 13

Queloz, D., Mayor, M., Weber, L., Blécha, A., Burnet, M., Confino, B., Naef, D., Pepe, F., Santos, N., and Udry, S.: 2000, The coralie survey for southern extra-solar planets. i. a planet orbiting the star gliese 86, *A&A* **354**, 99 13

Quillen, A. C.: 2007, Diffusive low optical depth particle discs truncated by planets, *MNRAS* **377**, 1287 5

Quillen, A. C. and Faber, P.: 2006, Chaotic zone boundary for low free eccentricity particles near an eccentric planet, *MNRAS* **373**, 1245 101

Quillen, A. C. and Thorndike, S.: 2002, Structure in the ϵ eridani dusty disk caused by mean motion resonances with a 0.3 eccentricity planet at periastron, *ApJ* **578**, L149 42

Rafikov, R. R.: 2011, Runaway accretion of metals from compact discs of debris on to white dwarfs, *MNRAS* pp L287+ 21

Raymond, S. N., Barnes, R., Veras, D., Armitage, P. J., Gorelick, N., and Greenberg, R.: 2009, Planet-planet scattering leads to tightly packed planetary systems, *ApJ* **696**, L98 140

Reach, W. T., Kuchner, M. J., von Hippel, T., Burrows, A., Mullally, F., Kilic, M., and Winget, D. E.: 2005, The dust cloud around the white dwarf g29-38, *ApJ* **635**, L161 18, 86

Reidemeister, M., Krivov, A. V., Stark, C. C., Augereau, J., Löhne, T., and Müller, S.: 2011, The cold origin of the warm dust around ϵ eridani, *A&A* **527**, A57+ 121

Rieke, G. H., Su, K. Y. L., Stansberry, J. A., Trilling, D., Bryden, G., Muzerolle, J., White, B., Gorlova, N., Young, E. T., Beichman, C. A., Stapelfeldt, K. R.,

and Hines, D. C.: 2005, Decay of planetary debris disks, *ApJ* **620**, 1010 47, 54, 88

Sato, B.: 2005, Okayama planet search program, *Journal of Korean Astronomical Society* **38**, 315 8

Sato, B., Omiya, M., Liu, Y., Harakawa, H., Izumiura, H., Kambe, E., Toyota, E., Murata, D., Lee, B.-C., Masuda, S., Takeda, Y., Yoshida, M., Itoh, Y., Ando, H., Kokubo, E., Ida, S., Zhao, G., and Han, I.: 2010, Substellar companions to evolved intermediate-mass stars: Hd 145457 and hd 180314, *PASJ* **62**, 1063 8

Setiawan, J., Klement, R. J., Henning, T., Rix, H., Rochau, B., Rodmann, J., and Schulze-Hartung, T.: 2010, A giant planet around a metal-poor star of extragalactic origin, *Science* **330**, 1642 9

Sheret, I., Dent, W. R. F., and Wyatt, M. C.: 2004, Submillimetre observations and modelling of vega-type stars, *MNRAS* **348**, 1282 34

Siess, L. and Livio, M.: 1999, The accretion of brown dwarfs and planets by giant stars - ii. solar-mass stars on the red giant branch, *MNRAS* **308**, 1133 8

Silvotti, R., Schuh, S., Janulis, R., Solheim, J.-E., Bernabei, S., Østensen, R., Oswalt, T. D., Bruni, I., Gualandi, R., Bonanno, A., Vauclair, G., Reed, M., Chen, C.-W., Leibowitz, E., Paparo, M., Baran, A., Charpinet, S., Dolez, N., Kawaler, S., Kurtz, D., Moskalik, P., Riddle, R., and Zola, S.: 2007, A giant planet orbiting the 'extreme horizontal branch' star v391 pegasi, *Nature* **449**, 189 10

Silvotti, R., Sozzetti, A., and Lattanzi, M.: 2011a, in . U. H. S. Schuh, H. Drechsel (ed.), *American Institute of Physics Conference Series*, Vol. 1331 of *American Institute of Physics Conference Series*, pp 336–339 12, 154

Silvotti, R., Szabó, R., Degroote, P., Østensen, R. H., and Schuh, S.: 2011b, The potential of the timing method to detect evolved planetary systems, *American Institute of Physics Conference Series* **1331**, 133 10

Sion, E. M., Holberg, J. B., Oswalt, T. D., McCook, G. P., and Wasatonic, R.: 2009, The white dwarfs within 20 parsecs of the sun: Kinematics and statistics, *AJ* **138**, 1681 79, 86

Smith, B. A. and Terrile, R. J.: 1984, A circumstellar disk around beta pictoris, *Science* **226**, 1421 5

Smith, R., Churcher, L. J., Wyatt, M. C., Moerchen, M. M., and Telesco, C. M.: 2009a, Resolved debris disc emission around η telescopii: a young solar system or ongoing planet formation?, *A&A* **493**, 299 115

Smith, R., Wyatt, M. C., and Haniff, C. A.: 2009b, Resolving the hot dust around hd69830 and η corvi with midi and visir, *A&A* **503**, 265 142, 143

Soker, N.: 1998, Can planets influence the horizontal branch morphology?, *AJ* **116**, 1308 10

Soker, N.: 2001, Extrasolar planets and the rotation and axisymmetric mass-loss of evolved stars, *MNRAS* **324**, 699 115

Soker, N., Livio, M., and Harpaz, A.: 1984, The evolution of a star-'planet' system in the double core phase, *MNRAS* **210**, 189 8

Song, I., Zuckerman, B., Weinberger, A. J., and Becklin, E. E.: 2005, Extreme collisions between planetesimals as the origin of warm dust around a sun-like star, *Nature* **436**, 363 121, 142

Stark, C. C. and Kuchner, M. J.: 2008, The detectability of exo-earths and super-earths via resonant signatures in exozodiacal clouds, *ApJ* **686**, 637 42

Stark, C. C. and Kuchner, M. J.: 2009, A new algorithm for self-consistent three-dimensional modeling of collisions in dusty debris disks, *ApJ* **707**, 543 43

Stewart, S. T. and Leinhardt, Z. M.: 2009, Velocity-dependent catastrophic disruption criteria for planetesimals, *ApJ* **691**, L133 35

Su, K. Y. L., Chu, Y.-H., Rieke, G. H., Huggins, P. J., Gruendl, R., Napiwotzki, R., Rauch, T., Latter, W. B., and Volk, K.: 2007, A debris disk around the central star of the helix nebula?, *ApJ* **657**, L41 15, 46, 86, 89, 151

Su, K. Y. L., Rieke, G. H., Stansberry, J. A., Bryden, G., Stapelfeldt, K. R., Trilling, D. E., Muzerolle, J., Beichman, C. A., Moro-Martin, A., Hines, D. C., and Werner, M. W.: 2006, Debris disk evolution around a stars, *ApJ* **653**, 675 xi, 46, 47, 50, 54, 57, 88

Su, K. Y. L., Rieke, G. H., Stapelfeldt, K. R., Malhotra, R., Bryden, G., Smith, P. S., Misselt, K. A., Moro-Martin, A., and Williams, J. P.: 2009, The debris disk around hr 8799, *ApJ* **705**, 314 5, 55

Swinyard, B. and Nakagawa: 2009, The space infrared telescope for cosmology and astrophysics: Spica a joint mission between jaxa and esa, *Experimental Astronomy* **23**, 193 81

Tanaka, H., Inaba, S., and Nakazawa, K.: 1996, Steady-state size distribution for the self-similar collision cascade, *Icarus* **123**, 450 34

Thébault, P. and Augereau, J.: 2007, Collisional processes and size distribution in spatially extended debris discs, *A&A* **472**, 169 43

Thébault, P., Augereau, J. C., and Beust, H.: 2003, Dust production from collisions in extrasolar planetary systems. the inner beta pictoris disc, *A&A* **408**, 775 39, 43

Thorsett, S. E., Arzoumanian, Z., Camilo, F., and Lyne, A. G.: 1999, The triple pulsar system psr b1620-26 in m4, *ApJ* **523**, 763 11

Tiscareno, M. S. and Malhotra, R.: 2009, Chaotic diffusion of resonant kuiper belt objects, *AJ* **138**, 827 123

Tisserand, F.-F.: 1896, *Trait de Mcanique Cleste IV*, Gauthier-Villars, Paris 122

Tremaine, S.: 1993, in . S. R. K. J. A. Phillips, S. E. Thorsett (ed.), *Planets Around Pulsars*, Vol. 36 of *Astronomical Society of the Pacific Conference Series*, pp 335–344 95, 123

Trujillo, C. A. and Brown, M. E.: 2001, The radial distribution of the kuiper belt, *ApJ* **554**, L95 94

van Winckel, H.: 2003, Post-agb stars, *ARA&A* **41**, 391 13

van Winckel, H., Lloyd Evans, T., Briquet, M., De Cat, P., Degroote, P., De Meester, W., De Ridder, J., Deroo, P., Desmet, M., Drummond, R., Eyer, L., Groenewegen, M. A. T., Kolenberg, K., Kilkenny, D., Ladjal, D., Lefever, K., Maas, T., Marang, F., Martinez, P., Østensen, R. H., Raskin, G., Reyniers, M., Royer, P., Saesen, S., Uytterhoeven, K., Vanautgaerden, J., Vandenbussche, B., van Wyk, F., Vučković, M., Waelkens, C., and Zima, W.: 2009, Post-agb stars with hot circumstellar dust: binarity of the low-amplitude pulsators, *A&A* **505**, 1221 46

Vassiliadis, E. and Wood, P. R.: 1993, Evolution of low- and intermediate-mass stars to the end of the asymptotic giant branch with mass loss, *ApJ* **413**, 641 xv, 11, 51

Veras, D. and Armitage, P. J.: 2004, The dynamics of two massive planets on inclined orbits, *Icarus* **172**, 349 101

Veras, D., Wyatt, M. C., Mustill, A. J., Bonsor, A., and Eldridge, J. J.: 2011, The great escape: How exoplanets and smaller bodies desert dying stars, *MNRAS* submitted 11, 29, 30

Villaver, E. and Livio, M.: 2007, Can planets survive stellar evolution?, *ApJ* **661**, 1192 93, 145

Villaver, E. and Livio, M.: 2009, The orbital evolution of gas giant planets around giant stars, *ApJ* **705**, L81 8, 9

von Hippel, T., Kuchner, M. J., Kilic, M., Mullally, F., and Reach, W. T.: 2007a, in R. Napiwotzki and M. R. Burleigh (eds.), *15th European Workshop on White Dwarfs*, Vol. 372 of *Astronomical Society of the Pacific Conference Series*, pp 327–+ 47

von Hippel, T., Kuchner, M. J., Kilic, M., Mullally, F., and Reach, W. T.: 2007b, The new class of dusty daz white dwarfs, *ApJ* **662**, 544 18, 92

Wickramasinghe, D. T., Farihi, J., Tout, C. A., Ferrario, L., and Stancliffe, R. J.: 2010, Does gd356 have a terrestrial planetary companion?, *MNRAS* **404**, 1984 11

Willson, L. A.: 2000, Mass loss from cool stars: Impact on the evolution of stars and stellar populations, *ARA&A* **38**, 573 11, 51

Wisdom, J.: 1980, The resonance overlap criterion and the onset of stochastic behavior in the restricted three-body problem, *AJ* **85**, 1122 28, 93, 100, 102, 122, 123

Wolszczan, A.: 1994, Confirmation of earth-mass planets orbiting the millisecond pulsar psr b1257+12, *Science* **264**, 538 12

Wolszczan, A. and Frail, D. A.: 1992, A planetary system around the millisecond pulsar psr1257 + 12, *Nature* **355**, 145 12

Wright, J. T., Fakhouri, O., Marcy, G. W., Han, E., Feng, Y., Johnson, J. A., Howard, A. W., Fischer, D. A., Valenti, J. A., Anderson, J., and Piskunov, N.: 2011, The exoplanet orbit database, *PASP* **123**, 412 2, 13

Wyatt, M. C.: 2003, Resonant trapping of planetesimals by planet migration: Debris disk clumps and vega's similarity to the solar system, *ApJ* **598**, 1321 5, 42, 43

Wyatt, M. C.: 2005, The insignificance of p-r drag in detectable extrasolar planetesimal belts, *A&A* **433**, 1007 40, 66

Wyatt, M. C.: 2008, Evolution of debris disks, *ARA&A* **46**, 339 32, 81, 120, 145

Wyatt, M. C., Clarke, C. J., and Booth, M.: 2011, Debris disk size distributions: steady state collisional evolution with p-r drag and other loss processes, *ArXiv e-prints* 39, 43

Wyatt, M. C. and Dent, W. R. F.: 2002, Collisional processes in extrasolar planetesimal discs - dust clumps in fomalhaut's debris disc, *MNRAS* **334**, 589 34, 53

Wyatt, M. C., Dermott, S. F., Telesco, C. M., Fisher, R. S., Grogan, K., Holmes, E. K., and Piña, R. K.: 1999, How observations of circumstellar disk asymmetries can reveal hidden planets: Pericenter glow and its application to the hr 4796 disk, *ApJ* **527**, 918 5, 36, 42, 43, 115

Wyatt, M. C., Greaves, J. S., Dent, W. R. F., and Coulson, I. M.: 2005, Submillimeter images of a dusty kuiper belt around η corvi, *ApJ* **620**, 492 121, 142, 143

Wyatt, M. C., Smith, R., Greaves, J. S., Beichman, C. A., Bryden, G., and Lisse, C. M.: 2007a, Transience of hot dust around sun-like stars, *ApJ* **658**, 569 36, 37, 121

Wyatt, M. C., Smith, R., Su, K. Y. L., Rieke, G. H., Greaves, J. S., Beichman, C. A., and Bryden, G.: 2007b, Steady state evolution of debris disks around a stars, *ApJ* **663**, 365 xiii, xv, 34, 36, 46, 48, 52, 53, 54, 55, 56, 57, 62, 73, 78, 88, 110, 111

Zuckerman, B., Kim, S. S., and Liu, T.: 1995, Luminosity class iii stars with excess far-infrared emission, *ApJ* **446**, L79+ 15, 82

Zuckerman, B., Koester, D., Reid, I. N., and Hünsch, M.: 2003, Metal lines in da white dwarfs, *ApJ* **596**, 477 13, 16, 92, 113, 117, 144

Zuckerman, B., Melis, C., Klein, B., Koester, D., and Jura, M.: 2010, Ancient planetary systems are orbiting a large fraction of white dwarf stars, *ApJ* **722**, 725 16, 113, 117

Zuckerman, B. and Reid, I. N.: 1998, Metals in cool da white dwarfs, *ApJ* **505**, L143 13